

Copyright is owned by the Author of the thesis. Permission is given for a copy to be downloaded by an individual for the purpose of research and private study only. The thesis may not be reproduced elsewhere without the permission of the Author.

DESIGN AND VALIDATION OF CELLULAR AERIAL BASE STATION PLATFORM FOR MOBILE PHONE LOCALISATION IN SEARCH AND RESCUE

A thesis presented in partial fulfillment of the requirements for the degree of

Master of Engineering

in

Electronic and Computer Engineering

At Massey University, Palmerston North, New Zealand



TODD MURRAY
FEBRUARY 2023

Abstract

Natural and man-made disasters can trap victims under rubble and debris, and it is generally up to nearby civilians and Search and Rescue (SAR) teams to locate and extricate these victims. The aftermath of disasters such as earthquakes, tsunamis, floods, and terrorist attacks can be quite dangerous. Paired with the frantic nature of search and rescue, this environment can be chaotic (Charfuelan and Kruijff 2013). Additionally, there is no international 'protocol' which defines how these SAR operations should be carried out (Statheropoulos, Agapiou et al. 2015). Consequently, search efforts are often unorganised until dedicated SAR teams can take over from those helping in the immediate vicinity (Bäckström and Christoffersson 2006, Spence, So et al. 2011).

Current methods for locating trapped victims after earthquakes and similar events is largely restricted to equipment that is expensive, bulky, and difficult to mobilise. This is especially apparent in poorer, disaster-prone areas. There is a clear opportunity to develop a system that capitalises on the disadvantages of the existing equipment, whilst also exploiting the prevalence of mobile phones. Although there is existing research that has proposed cellular-based localisation solutions, these systems are quite complex. Some of these complex systems utilise complex principles and algorithms to locate mobile phones. There appears to be a distinct lack of proposed solutions that utilise signal-strength-based metrics for localisation. Measuring signal-strength-based metrics of cellular channels has potential to locate victims in search and rescue scenarios. However, there are many different factors which affect the technical feasibility of such a system. The extent to which signal-strength-based metrics can be used as localisation metrics in search and rescue scenarios is explored in this research.

A novel UAV-based test rig was fabricated to capture signal-strength-based metrics of Long Term Evolution (LTE) cellular signals with respect to position for different testing environments. This research aims to assess whether a cellular aerial base station provides a viable platform for locating mobile phones in search and rescue scenarios. For a proof-of-concept, the results obtained show great promise that the system is technically feasible.

Acknowledgement

This project originated as an Honours research project stemming from the final part of my undergraduate Engineering degree at Massey University. This project combines my interest in telecommunications and UAVs. Holistically, it has been fulfilling to explore the synergy of these two technologies with the intention of designing a platform to help save human lives. This Masters project was funded in conjunction with a sponsor company, Salcom Ltd, who specialise in development, manufacturing, and supply of wireless solutions for a wide variety of applications including emergency services. Hence, there is a heavy emphasis on implementation and tangible hardware in this Thesis.

I'd like to acknowledge Callaghan Innovation for enabling this project to happen. Furthermore, I'd like to acknowledge Salcom Ltd, particularly Mohammad Ayat and Alan Jacks, for being the industry partners of this project.

I'd like to extend my gratitude to my supervisors, Dr Morio Fukuoka, who is somewhat responsible for encouraging my interest in UAVs, and Dr Faraz Hasan, who is somewhat responsible for encouraging my interest in telecommunications. Acknowledgement needs to be given to Ryan Warner, who was always willing to lend a technical hand. I extend my deep gratitude to close friends and family, who were here to help through this time.

Table of Contents

1. INTRODUCTION.....	12
1.1 BACKGROUND AND MOTIVATION.....	12
1.2 PROBLEM FORMULATION AND RESEARCH QUESTION.....	13
1.3 THESIS CHAPTER OUTLINE.....	14
2. LITERATURE REVIEW	15
2.1 PREFACE	15
2.2 CURRENT STATE OF THE ART.....	15
2.3 UAV-BASED SEARCH AND RESCUE SYSTEMS.....	16
2.3.1 UAV SAR Systems Using Cellular Radio Technologies.....	17
2.3.2 UAV SAR Systems Using Non-cellular Radio Technologies.....	19
2.4 NON-UAV-BASED SEARCH AND RESCUE SYSTEMS.....	21
2.4.1 SAR Systems Using Cellular Radio Technologies.....	21
2.5 RADIO CONSIDERATIONS FOR SEARCH AND RESCUE.....	22
2.5.1 Architecture of Cellular 4G/LTE Deployments.....	22
2.5.2 Applicability of Time Versus Signal Strength Metrics.....	23
2.5.3 Processing of Radio Metrics for Localisation Purposes.....	24
2.5.4 Other Radio Considerations.....	25
2.6 OTHER REVIEW.....	26
2.6.1 UAV Path Planning Algorithms for SAR.....	26
2.6.2 Special Considerations for UAV Implementations.....	29
2.7 DEFINING THE OPPORTUNITY.....	30
3. INFORMING DESIGN FROM RESEARCH.....	32
3.1 DEVELOPING REQUIREMENTS.....	32
3.2 FUNCTIONAL HIERARCHY.....	33
3.3 PRODUCT ARCHITECTURE.....	34
3.4 PROPOSED MODUS OPERANDI.....	35
4. UAV IMPLEMENTATION.....	36
4.1 BASELINE VEHICLE.....	36
4.1.1 Vehicle Overview.....	36
4.1.2 Vehicle Software.....	37
4.1.3 Vehicle Control.....	38
4.2 PAYLOAD HARDWARE.....	39
4.2.1 Cellular Radio.....	39
4.2.2 Onboard Computer.....	40
4.2.3 Directional Antenna.....	41
4.2.4 Nadir Mechanism.....	43
4.3 PAYLOAD CONTROL.....	44
4.3.1 Nadir Antenna Control.....	44
4.4 UAV OPERATION.....	46
4.4.1 Flight Planning Considerations.....	46
4.4.2 Antenna Beam-width Considerations.....	48
5. GROUND STATION IMPLEMENTATION.....	50
5.1 OVERVIEW.....	50
5.2 COMPUTER AND NETWORK SETUP.....	50
5.3 ANTENNA STEERING MECHANISM.....	51
5.3.1 Specifications.....	51
5.3.2 Antenna Steering Calculations.....	52
5.3.3 Antenna Steering Limitations.....	55
OTHER EQUIPMENT AND CONSIDERATIONS.....	56
5.3.4 Wi-Fi Link Range.....	56

5.3.5	<i>Charging and Power Considerations</i>	57
6.	CELLULAR AND RADIO IMPLEMENTATION	58
6.1	CELLULAR STACK	58
6.1.1	<i>Segregated Architecture</i>	58
6.1.2	<i>Cellular Radio Frontend</i>	59
6.2	CELLULAR NETWORK SETUP	60
6.2.1	<i>SIM cards and COTS UE</i>	60
6.2.2	<i>Cellular Channel Setup</i>	60
6.2.3	<i>Parameter Configuration</i>	61
6.3	FLIGHT CONSIDERATIONS	62
6.3.1	<i>RF Propagation Characteristics in Environment</i>	62
6.3.2	<i>Location Inference Parameters</i>	63
6.3.3	<i>Cellular Link Range</i>	65
7.	SOFTWARE IMPLEMENTATION	67
7.1	SYSTEM ARCHITECTURE	67
7.2	ROS SETUP.....	68
7.2.1	<i>ROS Topics</i>	68
7.2.2	<i>Bagging ROS Data</i>	70
7.3	PROTOTYPE SOFTWARE WORKFLOW	71
7.3.1	<i>Shell Scripts</i>	71
7.4	PROCESSING SOFTWARE WORKFLOW	72
7.4.1	<i>Raw Data Processing</i>	72
7.4.2	<i>Raw Image Processing</i>	73
7.4.3	<i>Geographical Alignment and Post-Processing</i>	74
8.	VALIDATION	75
8.1	SUBSYSTEM TESTING	75
8.1.1	<i>Speed Testing</i>	75
8.1.2	<i>BladeRF Channel Power</i>	79
8.2	PRELIMINARY TESTING.....	81
8.2.1	<i>Testing Objective</i>	81
8.2.2	<i>Test Methodology</i>	81
8.2.3	<i>Preliminary Test 1</i>	82
8.2.4	<i>Preliminary Test 2</i>	84
8.2.5	<i>Preliminary Test 3</i>	86
8.2.6	<i>Observations</i>	89
8.3	PRIMARY TESTING	90
8.3.1	<i>Post-testing Improvements</i>	90
8.3.2	<i>Testing Methodology</i>	90
8.3.3	<i>Testing Environment</i>	91
8.3.4	<i>Primary Test 1</i>	92
8.3.5	<i>Primary Test 2</i>	94
8.3.6	<i>Primary Test 3</i>	96
8.3.7	<i>Primary Test 4</i>	98
8.3.8	<i>Observations</i>	99
9.	CONCLUSIONS AND RECOMMENDATIONS	100
9.1	SUMMARY	100
9.2	RECOMMENDATIONS FOR FUTURE WORK	101
APPENDIX A - ANTENNA RETURN LOSS		102
I.)	ENTIRE BAND: 500MHZ - 4000MHZ.....	102
II.)	LOWER BAND: 696MHZ - 960MHZ.....	102
III.)	MIDDLE BAND: 1700MHZ - 2700MHZ	103

IV.)	UPPER BAND: 3300MHZ - 3800MHZ	103
APPENDIX B - CONFIGURED SRSRAN PARAMETERS.....		104
APPENDIX C - SOFTWARE SCRIPT FLOW DIAGRAMS		105
I.)	SYSTEM SETUP WORKFLOW	105
II.)	LAUNCHING ROS WORKFLOW.....	106
III.)	LAUNCHING CELLULAR WORKFLOW	107
APPENDIX D WI-FI LINK RANGE USING OMNIDIRECTIONAL ANTENNA		108
BIBLIOGRAPHY		110

List of Figures

FIGURE 1:	NLSS BASED ALGORITHM, ADAPTED FROM ALGORITHM DEPICTED BY TOMIYAMA, TAKEDA ET AL. (2020)	28
FIGURE 2:	PROPOSED FLYING ALGORITHM FROM TIEMANN, FELDMEIER ET AL. (2018)	28
FIGURE 3:	PROPOSED HIGH-LEVEL FUNCTIONAL HIERARCHY.....	34
FIGURE 4:	PROPOSED HIGH-LEVEL PRODUCT ARCHITECTURE	34
FIGURE 5:	BASILINE MATRICE 100 UAV WITH DUAL BATTERIES. IMAGE SOURCED FROM DJI (2019).....	37
FIGURE 6:	ANNOTATED VIEW OF DJI Go APP	39
FIGURE 7:	ANNOTATED VIEW OF PIX4DCAPTURE APP	39
FIGURE 8:	THE APPROXIMATE VERTICAL AND HORIZONTAL BEAMWIDTHS OF THE DIRECTIONAL ANTENNA.....	42
FIGURE 9:	THREE RENDERS SHOWING THE OPERATION OF THE ANTENNA UPON THE M100.....	43
FIGURE 10:	THE ANTENNA COMPENSATION MECHANISM WHICH MOUNTS TO THE M100.....	44
FIGURE 11:	PWM CONTROL OF THE ANTENNA COMPENSATION SERVO.....	46
FIGURE 12:	A DEPICTION OF THE HORIZONTAL AND VERTICAL GSDs OF RADIO SAMPLES	48
FIGURE 13:	THE APPROXIMATE TRANSMIT COVERAGE AREAS CORRESPONDING TO DIFFERENT FLIGHT HEIGHTS	49
FIGURE 14:	RADIATION PATTERN OF DIRECTIONAL CELLULAR ANTENNA FROM SIDE AND TOP VIEWS RESPECTIVELY .	49
FIGURE 15:	THE NETWORK AND DATA ARCHITECTURE OF THE GROUND CONTROL STATION.....	51
FIGURE 16:	THE POWER AND CONTROL ARCHITECTURE OF THE GROUND CONTROL STATION	52
FIGURE 17:	DIAGRAMS REPRESENTING ELEVATION AND AZIMUTH ANGLES RESPECTIVELY	53
FIGURE 18:	TRIANGLE REPRESENTING MATHEMATICAL RELATIONSHIP BETWEEN GCS AND UAV.....	54
FIGURE 19:	MINIMUM DISTANCE BETWEEN THE GCS AND FULL-SPEED UAV TO MAINTAIN TRACKING	55
FIGURE 20:	STANDARD SRSRAN ARCHITECTURE.....	58
FIGURE 21:	CUSTOMISED SRSRAN ARCHITECTURE	58
FIGURE 22:	THE HARDWARE ARCHITECTURE OF THE BLADERF XA4	59
FIGURE 23:	THE SOFTWARE ARCHITECTURE OF THE SYSTEM.....	67
FIGURE 24:	TERMINAL OUTPUT SHOWING SUCCESSFUL HAND-SHAKING PROCEDURE	68
FIGURE 25:	TERMINAL OUTPUT OF ROS TOPICS AVAILABLE.....	69
FIGURE 26:	ANNOTATED TMUX INTERFACE	71
FIGURE 27:	RAW DATA PROCESSING WORKFLOW	73
FIGURE 28:	RAW IMAGE PROCESSING WORKFLOW	73
FIGURE 29:	POST-PROCESSING WORKFLOW	74
FIGURE 30:	UAV FLIGHT PATH FLOWN FOR SPEED TESTING.....	76
FIGURE 31:	SPEED TEST OF OMNIDIRECTIONAL ANTENNA ON GCS AND EXTERNAL DONGLE ON UAV	76
FIGURE 32:	SPEED TEST OF OMNIDIRECTIONAL ANTENNA ON GCS AND ONBOARD RPI4 WI-FI ON UAV.....	77
FIGURE 33:	SPEED TEST OF DIRECTIONAL ANTENNA ON GCS AND EXTERNAL DONGLE ON UAV	77
FIGURE 34:	SPEED TEST OF DIRECTIONAL ANTENNA ON GCS AND ONBOARD RPI4 WI-FI ON UAV	78
FIGURE 35:	TEST SETUP FOR OUTPUT POWER ANALYSIS	79
FIGURE 36:	SRSRAN OUTPUT POWER TESTING RESULTS	80
FIGURE 37:	ORTHOMOSAIC LAYER OVERLAID ON SATELLITE BASE MAP SHOWING UE LOCATION	82
FIGURE 38:	EPRE HEAT-MAP OVERLAID ON TOP OF BASE MAPS	83
FIGURE 39:	HEAT-MAP THRESHOLDED FOR EPRE VALUES > 10DBFS.....	83
FIGURE 40:	ORTHOMOSAIC LAYER OVERLAID ON SATELLITE BASE MAP SHOWING PHONE LOCATION	84

FIGURE 41: EPRE HEAT-MAP OVERLAID ON TOP OF BASE MAPS	85
FIGURE 42: HEAT-MAP THRESHOLDED FOR EPRE VALUES > 10DBFS	85
FIGURE 43: ORTHOMOSAIC LAYER OVERLAID ON SATELLITE BASE MAP SHOWING PHONE LOCATION	86
FIGURE 44: EPRE HEAT-MAP OVERLAID ON TOP OF BASE MAPS	87
FIGURE 45: HEAT-MAP THRESHOLDED FOR EPRE VALUES > 15DBFS	87
FIGURE 46: THE FLIGHT PATH RELATIVE TO THE HEAT-MAP	88
FIGURE 47: THE ERROR BETWEEN CONSECUTIVE STATIC POSITIONS OF UE	89
FIGURE 48: SATELLITE BASE MAP OF PRIMARY TESTING SITE SHOWING 60M FLIGHT PATH	91
FIGURE 49: UNPROCESSED HEAT-MAP FROM PRIMARY TEST 1	92
FIGURE 50: FULLY PROCESSED HEAT-MAP FROM PRIMARY TEST 1	93
FIGURE 51: ENHANCED SALIENCY PROVIDED BY ORTHOPHOTO BASE MAP	93
FIGURE 52: UNPROCESSED HEAT-MAP FROM PRIMARY TEST 2	94
FIGURE 53: FULLY PROCESSED HEAT-MAP FROM PRIMARY TEST 2	95
FIGURE 54: ROLL ERROR (θ_R) AND TILT ERROR (θ_T) DURING FLIGHT	96
FIGURE 55: UNPROCESSED HEAT-MAP FROM PRIMARY TEST 3	97
FIGURE 56: FULLY PROCESSED HEAT-MAP FROM PRIMARY TEST 3	97
FIGURE 57: UNPROCESSED HEAT-MAP FROM PRIMARY TEST 4	98
FIGURE 58: FULLY PROCESSED HEAT-MAP FROM PRIMARY TEST 4	99

List of Tables

TABLE 1: FEATURES, FUNCTIONS AND ARCHITECTURE INSIGHTS GAINED FROM LITERATURE REVIEW	32
TABLE 2: KEY SPECIFICATIONS OF DJI MATRICE 100, SOURCED FROM DJI (2019)	36
TABLE 3: SOFTWARE VERSIONS OF CONSTITUENT COMPONENTS	38
TABLE 4: KEY PARAMETERS OF NUAND BLADERF xA4 SDR	40
TABLE 5: FEATURES OF RASPBERRY PI 4 SBC	41
TABLE 6: THE CONNECTIONS BETWEEN THE ONBOARD PI AND OTHER COMPONENTS	41
TABLE 7: SPECIFICATIONS OF CELLULAR ANTENNA FOR DIFFERENT FREQUENCY RANGES	42
TABLE 8: SPECIFICATIONS OF HI-TEC HS755HB SERVO	43
TABLE 9: SPECIFICATIONS OF THE PAN/TILT MECHANISM FITTED WITH HI-TEC HS785HB SERVOS	51
TABLE 10: THE CONFIGURATION SCRIPTS USED IN SRSRAN	61
TABLE 11: THE CONFIGURABLE PARAMETERS IN SRSRAN	61
TABLE 12: SUBSCRIBED ROS TOPICS AND CORRESPONDING DETAILS	69
TABLE 13: THE VARIOUS DATA PARAMETERS AND CORRESPONDING TRANSMISSION RATES	70
TABLE 14: THE DATA TYPE SETTINGS OF SPECIFIC VEHICLE PARAMETERS	70
TABLE 15: THE FIXED AND VARIABLE PARAMETERS DEFINED FOR PRELIMINARY TESTING	81

List of Abbreviations

3G	Third Generation (cellular)
3GPP	Third Generation Partnership Project
4G	Fourth Generation (cellular)
5G	Fifth Generation (cellular)
AoA	Angle of Arrival
AP	Access Point
API	Application Programming Interface
ARM	Advanced RISC Machine
CDMA	Code-Division Multiple Access
CNN	Convolutional Neural Network
COTS	Commercial Off The Shelf
CPU	Central Processing Unit
CQI	Channel Quality Indicator
CSV	Comma-Separated Values
CW	Continuous Wave
D2D	Device to Device
DAC	Digital to Analog Converter
dB	Decibel
dBFS	Decibels relative to Full Scale
dBm	Decibel Milliwatts
DDR4	Double Data Rate version 4
DJI	Da-Jiang Innovations
DMRS	Demodulation Reference Signal
DSM	Digital Surface Model
DTM	Digital Terrain Model
EIRP	Equivalent Isotropic Radiated Power
eNB	Evolved Node B
EPC	Evolved Packet Core
EPRE	Energy Per Resource Element
ESC	Electronic Speed Controller
FCC	Federal Communications Commission
FDD	Frequency Division Duplexing
FPGA	Field Programmable Gate Array
FSO	Free Space Optical (telecommunications)

GCS	Ground Control Station
GIS	Geographic Information System
GPIO	General Purpose Input Output
GPS	Global Positioning System
GSD	Ground Sampling Distance
GSM	Global System for Mobile Communication
HDL	Hardware Description Language
HFSS	High Frequency Simulation Software
IC	Integrated Circuit
IDW	Inverse Distance Weighting
IMSI	International Mobile Subscriber Identity
IMU	Inertial Measurement Unit
IO	Input Output
iOS	iPhone Operating System
IP	Internet Protocol
ISM	Industrial, Scientific, and Medical
JTAG	Joint Test Action Group
KI	Key
LAN	Local Area Network
LNA	Low Noise Amplifier
LoS	Line of Sight
LPDDR4	Low Power Double Data Rate version 4
LSTM	Long Short-Term Memory
LTE	Long Term Evolution
LTS	Long Term Support (in reference to operating systems)
M100	DJI Matrice 100 UAV
MAC	Medium Access Control
MCC	Mobile Country Code
MCS	Modulation Coding Scheme
MIMO	Multiple-Input-Multiple-Output
MNC	Mobile Network Code
MSP	Mobile Station Power
NLLS	Non-Linear Least Squares
NMEA	National Marine Electronics Association
NTP	Network Time Protocol
OFDM	Orthogonal Frequency-Division Multiplexing

OPC	Operator Code
OSI	Operation Systems Interconnect
PA	Power Amplifier
PDSCH	Physical Downlink Shared Channel
PLL	Phase-Locked Loop
PoE	Power over Ethernet
PRB	Physical Resource Block
PSC	Public Safety Communication
PUSCH	Physical Uplink Shared Channel
PWM	Pulse Width Modulation
QPSK	Quadrature Phase Shift Keying
RAM	Random Access Memory
RAN	Radio Access Network
RF	Radio Frequency
RISC	Reduced Instruction Set Computer
RLF	Radio Link Failure
ROS	Robot Operating System
RPI3A	Raspberry Pi 3A
RPI4	Raspberry Pi 4
RRC	Radio Resource Control
RSRP	Reference Signal Received Power
RSRQ	Reference Signal Received Quality
RSS	Received Signal Strength
RSSI	Received Signal Strength Indicator
RTH	Return To Home
RTK	Real Time Kinematics
RX	Receiver
SAR	Search and Rescue
SBC	Single Board Computer
SCTP	Stream Control Transmission Protocol
SDK	Software Development Kit
SDR	Software-Defined Radio
SIM	Subscriber Identity Module
SMA	SubMiniature version A
SMS	Short Message Service
SNR	Signal to Noise Ratio

SPDT	Single Pole Double Throw
SRS	Software Radio Systems
SSH	Secure Shell
TA	Timing Advance
TCP	Transmission Control Protocol
TDD	Time Division Duplexing
TDoA	Time Difference of Arrival
TM	Transmission Mode
ToA	Time of Arrival
ToF	Time of Flight
TX	Transmitter
UARFCN	UTRA Absolute Radio Frequency Channel Number
UART	Universal Asynchronous Receiver Transmitter
UAV	Unmanned Aerial Vehicle
UDP	User Datagram Protocol
UE	User Equipment
USAR	Urban Search and Rescue
USB	Universal Serial Bus
USRP	Universal Software Radio Peripheral
UTRA	Universal Terrestrial Radio Access
VCTCXO	Voltage Controlled Temperature Compensated Crystal Oscillator
VSWR	Voltage Standing Wave Ratio
VTOL	Vertical Take-Off and Landing
WGS84	World Geodetic System 1984
WiSAR	Wilderness Search and Rescue
WSN	Wireless Sensor Network

Glossary

Nadir	Direction pointing directly below the point of reference
Noise floor	Wide-band power of noise as measured by a radio receiver
Orthomosaic	An orthorectified image comprised of smaller high-resolution images
Photogrammetry	Using photographs to make reliable measurements
Pitch	Rotation of aircraft along left to right axis of vehicle
Quaternion	A measure of rotations in 3D space using an ordered set of four numbers
Roll	Rotation of aircraft along front to back axis of vehicle
Yaw	Rotation of aircraft along vertical axis of vehicle

1. Introduction

1.1 Background and Motivation

Due to the time-sensitive nature of locating victims after disasters, there is a constant search for new technologies and products that can increase effectiveness, and reduce the time taken to locate victims (Wong and Robinson 2004, Bäckström and Christoffersson 2006, Statheropoulos, Agapiou et al. 2015). Some of the current search and rescue tools on the market are expensive and difficult to mobilise (Statheropoulos, Agapiou et al. 2015), especially to poorer, disaster-stricken areas. Some of the current tools also have limited range and limited effectiveness (Wong and Robinson 2004, Bäckström and Christoffersson 2006, Hamp, Zhang et al. 2014, Jiao, Shang et al. 2014). This combination of factors strengthens the need for more optimal and distributable SAR tools.

Natural and man-made disasters do not discriminate based on borders or countries. search and rescue teams can be deployed from different countries to help with SAR activities (Okita, Minato et al. 2019). For example, in the 2011 Christchurch earthquake, a specialist Japanese rescue team was deployed to help rescue victims (NZPA 2011). Such deployments highlight the need to have standardised procedures and equipment in place. It is important to standardise procedures to ensure effective communication between rescue teams, and effective localisation and extrication of victims. Aspects for standardisation include deployment, localisation equipment, localisation procedures and victim extrication (Wong and Robinson 2004). Additionally, SAR attempts need to have increased speed according to Statheropoulos, Agapiou et al. (2015) and Wong and Robinson (2004). Having an inherently faster first-response tool to deploy will drastically increase the speed and accuracy by which victims can be located. There are promising technologies available that can be used to create such a first-response tool.

Aerial base stations is one of these technologies and have been a prominent figure in telecommunications research within the last 10 years. This is due to the demand of such systems for:

- network rehabilitation after natural and man-made disasters
- temporary cellular capacity increase in densely populated areas
- enhanced network performance for fast-moving users (Enayati, Saeedi et al. 2019)

Furthermore, Third Generation Partnership Project (3GPP) is looking at supporting non-terrestrial 5G networks in the not-so-distant future (Selim and Kamal 2018). Non-terrestrial networks include UAV-based networks.

Aerial base stations have the advantage of being inherently more mobile than existing solutions. Aerial base stations can move towards the User Equipment (UE) which may be buried or obstructed, allowing for a connection to be established and maintained. Unlike static base stations which may be rendered useless due to the severe attenuation properties of post-disaster scenarios (Avanzato and Beritelli 2019) or physical/structural damage.

For the reasons listed above, aerial base stations continue to be extensively studied. However, there is a limited amount of research towards the use of aerial base stations to

post-disaster localisation, or more generally, search and rescue. Post-disaster localisation has always been an active research topic, and with the prevalence of mobile devices, this application continues to become more relevant. There is a constant search for new devices and technologies which can increase the chances of finding victims faster and with greater efficacy (Murray and Hasan 2020). A study which explores the factors that affect search and rescue times in post-disaster scenarios points out that mobile phones and UAVs are both candidate technologies for future integrated search and rescue systems (Statheropoulos, Agapiou et al. 2015).

The uptake of mobile phones particularly within the last 20 years is tremendous and poses great potential for localisation. One survey study estimated that 80% of trapped disaster victims had their mobile phones present with them at the time of rescue (Zorn, Gardill et al. 2012). This warrants the development of a mobile phone-based SAR tool. However, it is important to understand the limitations of this technology in these environments.

Aerial base stations have traditionally involved mounting cellular ‘femtocells’ to UAVs, however there is a rising trend in software-defined radios that has enabled open-source cellular stack developments that are very appropriate for the application of aerial base stations. An example is presented by Murphy, Brown et al. (2017) and Murphy, Sreenan et al. (2019), whereby a software-defined radio is loaded with cellular stack firmware (YateBTS), and is used to host an aerial base station. The proposed system utilises a software-defined radio. This allows an aerial base station platform to be more modular. Modularity is a key hallmark of aerial base stations, as it allows similar systems to be built without the exact same components, whilst also retaining similar functionality and performance.

Using aerial base stations to aid with search and rescue is a relatively unexplored area in the literature. The state of the art of both cellular technology and UAV technology have advanced to such an extent that their unification is now realisable. Furthermore, utilising signal-strength-based metrics from aerial base stations provides a promising operating principle from which to develop a first-response tool.

The system proposed in this thesis utilises both UAVs and cellular technology to localise mobile phones in a fashion analogous to real-world search and rescue scenarios.

This research is heavily influenced by the premise of this project as a research and development project for the sponsor company, Salcom, who specialise in development, manufacturing, and supply of wireless hardware solutions for a wide variety of applications including emergency services. Therefore, there is a heavy emphasis on the design and build aspect of the research-based prototype.

1.2 Problem Formulation and Research Question

The problem was formulated based on the need and the research novelty of such a system. The research novelty is discussed further in chapter 2. The main research question is:

Does a cellular aerial base station provide a viable platform for locating mobile phones in search and rescue scenarios?

The sub-questions are as follows:

1. To what extent (if any) does a nadir cellular antenna provide useful inferences for localisation?
2. To what extent (if any) is a directional data link (between a ground station and UAV) warranted?

1.3 Thesis Chapter Outline

The remaining chapters of the thesis are outlined as described here. Chapter 2 details the literature review which was performed prior to determining the proposed implementation. Chapter 3 details the high-level design of the system. Chapter 4 details the UAV subset of the implementation. Chapter 5 details the ground station subset of the implementation. Chapter 6 details the cellular implementation. Chapter 7 details the software subset of the implementation. Chapter 8 details the validation of the implementation. Chapter 9 details the conclusions and the future works determined from the project.

This research will aim to establish whether:

- an aerial base station is suitable for search and rescue purposes
- cellular signal strength metrics are suitable for location inference
- a directional transmitter antenna aboard the aerial base station improves location inference

2. Literature Review

2.1 Preface

This literature review explores the extended implementations of cellular-based localisation systems for use after natural and man-made disasters. The primary focus of this literature search was exploring literature which utilise cellular technologies to locate victim's mobile phones. In the previous literature review performed by the authors, the research topic was much broader, focussing on the more holistic research around natural disasters and the general technologies used to locate victims. This previous literature review narrowed down into radio-based localisation techniques, and a research opportunity was found (Murray and Hasan 2022). The implementations covered in this previous literature review were primarily immobile (unmoving) systems. In order to warrant the development of a more advanced search and rescue system, research into more complex cellular localisation implementations must be performed. This is the literature review that details these implementations.

2.2 Current State of the Art

Cellular-based search and rescue tools are on the rise. This growth is predicated on various factors. For example, one study (Statheropoulos, Agapiou et al. 2015) discusses the candidacy of cellular technology to future integrated SAR systems due to the uptake of mobile phones in modern society.

The technology discussed within this area of research is quite varied, and it is difficult to categorise various implementations into well-defined sub-categories. One interesting observation from the radio-based technologies presented in the literature, is that the implementations can be categorised in a fashion analogous to that of the layered Operation Systems Interconnect (OSI) model (Hamp, Zhang et al. 2014). There are solutions which solely utilise the physical domain, whereas some implementations utilise higher-layer domains analogous to that of the datalink and network layers of the OSI model. An example of an implementation which works solely in the physical domain, is one which reads Received Signal Strength Indicator (RSSI) of a certain signal and does not analyse higher-level metrics in the stack such as Reference Signal Received Power (RSRP).

While cell phones can be located by the cellular provider using technologies available at the base station (i.e., triangulation), this is not guaranteed to work in inhomogeneous environments, such as earthquake rubble. Additionally, network carriers are generally reluctant to provide customer location information due to privacy concerns and confidentiality (Peral-Rosado, Raulefs et al. 2018). In the case of post-disaster localisation, network-assisted localisation is not really a guaranteed option.

Whilst most literature covered in this review utilise cellular technologies for localisation, many combine cellular technologies with other technologies to enhance performance. One example is utilising UAVs and cellular technology to enhance localisation performance. The intention of such research is to use UAVs alongside cellular implementations to

maximise localisation performance. This is an intuitive progression considering similar fields of localisation research (e.g., radio tracking of animals in wilderness) are also tending towards UAV technology. It is clear that using moving systems (i.e., flying cellular base stations) provides greater operating range and capability over static systems. Aerial-based vehicles are one of the least-impeded form of vehicle, so it is obvious that UAVs are being used for such systems. In addition to smart phones and radio technologies, Statheropoulos, Agapiou et al. (2015) highlights that UAVs are a great candidate technology for integrated Urban search and rescue systems. It is therefore established that the two unions that this literature review will focus on are radio technology (cellular in particular) and vehicle technology (UAVs in particular).

Considering cellular radio technology and UAV technology as the two primary unions for this literature review, the literature is split into four subclasses:

1. Implementations which utilise cellular radio technology and UAV technology
2. Implementations which utilise non-cellular radio technology and UAV technology
3. Implementations which utilise cellular radio technology and non-UAV technology
4. Implementations which utilise non-cellular radio technology and non-UAV technology

The rest of this literature review is organised into different sections based on these subclasses; subsection 2.3 details UAV-based systems. Subsection 2.3.1 and 2.3.2 correspond to subclass 1 and 2 respectively. Whereas subsection 2.4 details systems which do not exploit UAV systems. Similarly, subsection 2.4.1 details subclass 3 above. Subclass 4 above does not need to be covered, as implementation in this subclass were discussed extensively in the author's previous literature review (Murray and Hasan 2020), and subclass 4 is not the primary focus of this literature review.

2.3 UAV-based Search and Rescue systems

The proliferation of UAVs has afforded a whole range of services that were previously too logistically difficult to implement. Not so long ago, the idea of attaching a cellular base station to a UAV was considered a pipedream, however there is now a whole area of literature concerned with the attachment of cellular femtocells to UAV's. These papers investigate the logistics, performance, and capacity of aerial-based femtocells. These papers do not focus on localisation via aerial-based femtocells, this is a whole other research area.

Aerial base stations have been a prominent theme in telecommunications research within the last 10 years. This is due to the demand of such systems for:

- network rehabilitation after natural and man-made disasters (Gomez Chavez, Al-Hourani et al. 2015, Guevara, Rodriguez et al. 2015, Deruyck, Wyckmans et al. 2016, Deruyck, Wyckmans et al. 2018, Radišić, Muštra et al. 2019)
- temporary cellular capacity increase in densely populated areas
- enhanced network performance for fast-moving users (Enayati, Saeedi et al. 2019)

For the reasons listed above, aerial base stations continue to be extensively studied. However, there is limited research towards the application of aerial base stations to post-disaster localisation, or more generally, search and rescue.

There are other UAV-based systems which attempt to sense Radio Frequency (RF) targets based on other radio technologies such as Wi-Fi. There are also papers outlining research on raw radio measurements, such as signal strength-based measurements of a certain frequency from a UAV-based receiver. This variation in implementations reinforces the trend of papers analogous to the OSI model.

In UAV systems, an optimal trade-off has to be found “between flight performance, sensors, and computing resources” according to Tomic, Schmid et al. (2012). Another study emphasises that land-based robots equipped with wireless sensors have many issues with traversing terrain and obstacles, which can be mostly ignored with an aerial solution (Grogan, Pellerin et al. 2018). In reinforcement of this narrative, Grogan, Pellerin et al. (2018) notes that one of the primary advantages of UAVs is the unparalleled mobility and the ability to avoid difficult terrain, whilst also being able to get close to precarious structures with little risk to rescuers. This is not to say that UAVs are impervious to environmental factors. UAVs are particularly susceptible to high wind and rain. Grogan, Pellerin et al. (2018) also notes that there is a distinct lack of research (in disaster operations management research) which addresses search for injured people. This is further reinforced by Galindo and Batta (2013). It is agreed by Grogan, Pellerin et al. (2018) that UAVs should be able to fill this gap in research. Another paper addresses emergency management procedures and recognises that the first 72 hours following a disaster are the most important for the rescue of survivors (Erdelj, Król et al. 2017). Therefore, speed, mobility, resolution and efficacy are hallmarks of good emergency victim localisation system. Erdelj, Król et al. (2017) also recognises that aerial surveying provides the most effective situational awareness.

2.3.1 UAV SAR Systems Using Cellular Radio Technologies

Cellular network deployment via UAVs is a rapidly growing area of research, however the research area concerned with localisation of mobile phones via aerial base stations is also gaining traction. One of the first implementations was performed by Murphy, Brown et al. (2017), in which a BladeRF x40 Software Defined Radio was paired with a cellular stack (YateBTS) to implement a flying Global System for Mobile Communication (GSM) network. This Software-Defined Radio (SDR) is mounted on a UAV for the purpose of finding victims in search and rescue scenarios. This system localises sources using a Levenberg-Marquardt localisation algorithm. The depicted system also uses a pair of omnidirectional antennae. While this paper does not discuss any results, it focusses more on the implementation of the system. An interesting observation from this paper (and its successor (Murphy, Sreenan et al. 2019)) is that the authors purposefully augment the SDR frontend such that it appears more powerful to GSM phones in the search area, therefore target phones prioritise connection to the powerful GSM station. Another interesting observation is that association requests sent to the UAV-mounted GSM cell from the target cell phones are not accepted, so that the cell phones can maintain their connection to the original network. The connection that is established with the airborne GSM base station is adequate to measure RSSI. RSSI is the metric that is fed into the

localisation algorithm. The field-testing results discussed in the successive paper (Murphy, Sreenan et al. 2019), show that the system can localise targets to within a 1m range.

Another paper investigates the attachment of a 4G device to a UAV, for finding victims after avalanches (Wolfe, Frobe et al. 2015). This paper discusses the unique advantages of Universal Mobile Telecommunications System (UMTS) and LTE standards over previous mobile generations for localisation purposes. The primary advantages are that LTE deployments employ separate technology standards for the uplink and downlink, therefore making these signals more discernible. Additionally, 4G/LTE takes advantage of better beam-forming technology which allows for inherently better localisation due to the more focused downlink signal (Wolfe, Frobe et al. 2015). This paper also depicts a unique implementation consisting of a custom developed Android app to automate the transmission of LTE parameters from the buried device. This app checks for changes in RSSI, Reference Signal Received Power (RSRP), and Signal to Noise Ratio (SNR) on the buried phone and sends these changes via email to the 4G device attached to the UAV. This app is required to be preloaded on the device, which is a significant disadvantage. The 4G device attached to the UAV has a camera, from which the operators could see from the point-of-view of the UAV. One of the fundamental requirements of this study was to have two devices, one buried and one not buried and use the results from each to inform propagation models and resulting location inferences. One of the primary results of this study is a propagation model for both snow and air. It was also found that propagation of 4G LTE signals through snow was quite good. The system depicted in this paper was interesting due to its application, and the resulting hybrid propagation model.

Another paper which employs a similar system is presented by Avanzato and Beritelli (2020), in which a 4G femtocell is attached to a UAV for the purpose of finding disaster victims. This paper appears to be an advancement of two previous papers by the authors, Avanzato and Beritelli (2019) and Avanzato, Beritelli et al. (2019). The method presented by Avanzato and Beritelli (2019) is based on two parameters which are reported from the User Equipment to the Evolved Node B (eNB) base station in LTE networks. These parameters are RSRP and Reference Signal Received Quality (RSRQ). These measurements are performed for serving cells and neighbouring cells when the UE is moving between cells. In commercial LTE deployments, RSRP and RSRQ are usually reported to the eNB from the User Equipment in the case of an LTE A3 event (Mehta, Akhtar et al. 2015). An LTE A3 event usually occurs when the UE detects a higher received power from a neighbouring cell. Unlike the system presented by Zorn, Rose et al. (2010), the system presented by Avanzato and Beritelli (2019) does not require a cellular jammer for existing infrastructure. The UE is connected solely to the aerial femtocell. In Avanzato and Beritelli (2019), there are two main phases of operation, the classification phase and localisation phase. The classification phase attempts to determine whether a UE is inside the specified localisation area. The localisation phase attempts to find the location of the UE. Once the mobile phone is connected to the femtocell and the localisation phase has started, the RSRP is read from the femtocell, and mapped according to its location, resulting in a heat map of RSRP. Further post-processing algorithms, such as weighted-distance method, centre of gravity method, and other methods are executed dependent on the characteristics of the heat map, namely the number of "lakes" and "mountains" (high and low RSRP respectively) within the localisation area. The UAV is flown half a meter above the maximum rubble height.

Interestingly, the researchers found that a lower power was observed when the UAV was directly above the UE as opposed to areas slightly offset from the UE. This is likely due to the vertical polarisation of the omnidirectional femtocell antennae used, whereby the radiation pattern of the antenna does not correlate well with the uplink signal polarisation. The testing carried out in the author's initial papers on the topic (Avanzato and Beritelli 2019, Avanzato, Beritelli et al. 2019) does not use a UAV, instead the femtocell is moved manually, to scan walls of a building as opposed to a rubble site. The latest paper published by the authors (Avanzato and Beritelli 2020) tests the proposed system on a UAV platform. The results from this study show that a localisation accuracy of just above 60% with an average positioning error of 1m.

In another system detailed by Albanese, Sciancalepore et al. (2020), the authors claim to the best of their knowledge that their detailed system is the first 'UAV-based cellular search-and-rescue solution'. The solution, dubbed 'SARDO' uses technologies such as time-of-flight, machine-learning, feedback-based trajectory management and International Mobile Subscriber Identity (IMSI) interception. The fundamental principle of operation of SARDO is as follows: Time of Flight measurements are performed between the cellular-enabled SDR and the UE, these measurements are fed into a Convolutional Neural Network (CNN) which extrapolates relevant details from Time-of-Flight measurements to feed into a deep Feed-Forward Neural Network which "learns and implements the concept of pseudo-trilateration". The combination of this CNN and the subsequent Long Short-Term Memory (LSTM) network is used to gauge motion trajectory for future position detection. SARDO is only designed to localise UE's sequentially, not simultaneously. The concept of pseudo-trilateration is interesting and is relatively easily afforded in UAV systems. The idea of pseudo-trilateration is to travel between multiple pre-defined locations within a specific window of time to accumulate the data used for subsequent trilateration. This seems like an efficient alternative to having three or more time-synchronised UAV systems. The system detailed by Albanese, Sciancalepore et al. (2020) operates by deploying an LTE cell with omnidirectional antennae. The results of this paper claim that SARDO can determine the location of mobile phones at a rate of 3 minutes per UE and achieve an accuracy of tens of meters.

From the aforementioned selection of papers, it can be seen that there is a rising trend in cellular-based UAV SAR systems.

2.3.2 UAV SAR Systems Using Non-cellular Radio Technologies

While there is a whole research field concerned with aerial base stations, there are other radio technologies that can be deployed on a UAV platform for search and rescue purposes. One prevalent implementation amongst this subset of research is localisation of Wi-Fi enabled devices through Wi-Fi probe requests (Wang, Joshi et al. 2013, Sun, Wen et al. 2018, Kashihara, Yamamoto et al. 2019). The results from one such study (Wang, Joshi et al. 2013) show that devices can be reliably detected from up to 200m aerially. One disadvantage of this system was that, for best performance, the Media Access Control (MAC) address of the Wi-Fi device needed to be known prior to flying. The intended use case for this system is wilderness scenarios where the propagation environment is relatively homogeneous, as compared to a post-earthquake environment.

There are also other aerial systems which attempt to localise RF targets via Wi-Fi probe requests. Another example is detailed by Sun, Wen et al. (2018), which sniffs for probe requests from mobile phones. The RSSI from these probe requests is extracted and processed through a Kalman filter to remove fluctuations due to multipath and other signal physics issues. This RSSI is used to calculate distance based on propagation models. It then finds a direction 'gradient' using a circular flight path. A localisation accuracy of 7m was achieved in this study.

A similar technique is detailed by Acuna, Kumbhar et al. (2017), except the post-processing workflow consists of machine learning networks. There is also more geographical pre-processing involved in this paper, resulting in an overall estimation accuracy of 81.8%. An interesting point mentioned in this paper regards the flight path priority. The authors mention that the UAV should fly sufficiently slow to maximise the effective sampling rate. However, due to the time-sensitive nature of the operation, the UAV should also cover this area as quickly as possible. This is the trade-off between flight area and quality/accuracy that is evident across most research in this field.

The system depicted by Petitjean, Mezhoud et al. (2018) attempts to localise RF devices irrespective of their operating protocol, by using antenna switching. The system uses four separate low-gain directional antennae to localise a transmitting RF source based on intermittent bearing estimation. Whereby the UAV will find the bearing of the RF source, then fly towards the source for a fixed distance. This algorithm repeats until the transmitting source is found. The authors extended the scope of the project to find the optimal location between two ground users for investigative purposes. It is worth noting that the authors only attempt to target a transmitting SDR, and not a mobile phone. This is a limitation of the study and is an opportunity for further exploration. The exploitation of antenna switching between the four directional patch antennae was found to be a good method for estimating the transmission source bearing in relatively homogeneous propagation environments.

The main contribution by Dressel and Kochenderfer (2018) is demonstrating a two-antenna system for pseudo-bearing measurements, this paper focusses on a Wi-Fi implementation. The system uses a 9dBi Yagi-Uda directional antenna for bearing measurement and an omnidirectional antenna for normalising bearing measurements. The paper concludes that the proposed system is faster at locating RF sources than other systems which exploit 'rotate for bearing' modalities. Another paper by the same authors (Dressel and Kochenderfer 2018) uses low-gain directional antennae (Moxon antennae) paired to an RTL-SDR radio to localise a variety of sources, including a handheld radio, a RF enabled collar, and a smartphone. In this paper, the smartphone is forced into a phone call in order to constantly transmit a signal. This method seems somewhat unrealistic for a disaster scenario. However, the main contributions of this paper are to create a general RF localisation tool that is faster than existing systems. Isaacs, Quitin et al. (2014) exploits the use of directional antennae for the localisation and tracking of RF sources by measuring Received Signal Strength (RSS). This system uses a particle filter approach to inform the path planning algorithm. The directional antenna used is a PCB-based quad-patch antenna. The system is sensing using a pair of 2.4GHz XBee transceivers.

One paper presents a novel algorithm which leverages an array of directional antenna from a fixed wing UAV platform to localise targets in sparse sensor networks (Sorbelli, Das

et al. 2018). The authors claims that the use of directional antenna means that each sensor only requires one trilateration for localisation, therefore optimising the workflow over omnidirectional implementations. Additionally, by using directional antennae, rough estimation of the sensor position does not need to be performed initially.

It can be seen from the literature that there are a few key components in each implementation, such as RF target type, antennae used, and specific deployment environments.

2.4 Non-UAV-based Search and Rescue Systems

As mentioned previously, most of the papers in this literature review focus on UAVs due to their fundamental advantages in mobility and perspective. However, it is interesting to explore systems which utilise cellular radio technologies *not* in conjunction with UAVs.

2.4.1 SAR Systems Using Cellular Radio Technologies

One example of a SAR system using cellular technology is depicted by Tang, Shu et al. (2017) which uses a hybrid Angle-of-Arrival/Received Signal Strength Indicator (AoA/RSSI) positioning scheme to localise cell phones. The mechanism by which this is achieved is a ground-based OpenBTS equipped system. Like YateBTS, OpenBTS is another cellular stack which can be deployed in conjunction with Software Defined Radios. The proposed positioning process is as follows: The UE's position is coarsely estimated via AoA and a sector antenna. Following this phase, a more directional Yagi-Uda antenna is used for accurate positioning. Some interesting criteria were imposed upon the solution by the authors to make the proposed system disaster-friendly, such as keeping the weight of the entire system below 30kg and making the system easy to carry. This paper makes reference to another study (Hatorangan and Juhana 2014) which proposes a similar solution. Similar to the aforementioned paper, Hatorangan and Juhana (2014) also make use of a static network. However, instead of using antenna modalities to infer the location of the UE, the Global Positioning System (GPS) location is logged from Short Message Service (SMS) messages sent from each User Equipment to the base station. Tang, Shu et al. (2017) alludes to the fact that Hatorangan and Juhana (2014) do not make use of power devices such as power amplifiers or low noise amplifiers to enhance the localisation process, reinforcing the relatively small detection range. The system proposed by Tang, Shu et al. (2017) sets up a GSM network using a Universal Software Radio Peripheral (USRP) SDR, laptop, Low Noise Amplifier (LNA), Power Amplifier (PA) and battery. The system has a maximum transmission power of 20W allowing a larger detection range than the implementation proposed by Hatorangan and Juhana (2014). The authors use a long open road as a testing site instead of a disaster site. When testing the yagi antenna for accurate positioning, it was found that three parameters changed with respect to the direction of the antenna. These were RSSI, Mobile Station Power (MSP) and path loss. Intuitively, it was found that if the antenna faces the direction of the mobile device, the MSP and path loss decrease, and the RSSI increases. A large limitation of this study is the handheld nature of the yagi antenna. This means that the time taken to locate victims may be quite long due to the arduous nature of traversing post-disaster terrain. There is,

perhaps, an opportunity to attach this yagi antenna to a vehicle for more optimised searching.

Another example similar to Tang, Shu et al. (2017) is presented by Zorn, Rose et al. (2010). The analysis of this paper was covered more extensively by Murray and Hasan (2020). However, the premise of the implementation, was that a custom GSM cell was deployed in a portable setup and a GSM jammer was used to jam existing GSM infrastructure. First responders could then scan the area on foot with a handheld ‘power meter’ and sense areas of high signal strength.

More recent papers tend to avoid static, non-UAV cellular implementations.

2.5 Radio Considerations for Search and Rescue

2.5.1 Architecture of Cellular 4G/LTE Deployments

While localisation is not the primary purpose of flying (or aerial) base stations, it can be a beneficial side feature depending on the implementation. Another excerpt that can be taken from the research field of aerial base stations, is the cellular implementation. 4G/LTE is widely regarded as the most prevalent cellular implementation at the time of writing. The 4G/LTE architecture consists of two main components:

1. EPC: Evolved Packet Core
2. RAN: Radio Access Network, commonly referred to as the ‘eNB’

In most implementations, the radio access network is connected via a high-capacity wired link to the EPC. This connection is critical, because the EPC performs most of the packet routing and ‘heavy-lifting’ in the network. The EPC is also the interface between the cellular network and the wide area network (e.g., internet). In some cases, the EPC is connected to the eNB via a high bandwidth microwave link. However, the consistent theme across implementations, is a high bandwidth link between EPC and RAN. However, given the constraints of UAVs, which include limited battery life, and limited payload, it is important to minimise the weight and power draw of the onboard equipment. Therefore, there is an ever-increasing need for more powerful and power-efficient single board computers which can satisfy these constraints and provide enough computing performance to satisfy the cellular network requirements.

One solution to this problem is to separate the eNB and EPC and have the EPC running on a ground-based computer. This is discussed extensively by Sundaresan, Chai et al. (2018), whereby the authors *propose* a UAV-based eNB and a ground-based EPC. The link between these two systems would be a steered microwave antenna. This allows the directional microwave antenna to ‘follow’ the UAV as it flies. The authors propose this implementation for enhanced LTE connectivity as opposed to a dedicated SAR system. In the use case of increased LTE connectivity, the backhaul link is even more critical due to the increased traffic that will flow over said link.

2.5.2 Applicability of Time Versus Signal Strength Metrics

Literature in the area tends to use a mix of different metrics from which to infer the location of RF targets. The two most prevalent paradigms for localisation metrics are signal time and signal strength. Time-based metrics can be broken down into many subcategories (i.e., Time-Difference-of-Arrival (TDoA), Time-of-Flight (ToF), Time-of-Arrival (ToA)), as can signal-strength-based metrics (i.e., RSSI, SNR, RSRP). There are many respective advantages and disadvantages to time and signal-strength metrics for localisation.

Whilst time-oriented metrics, such as ToA, appear to provide the most accurate location results (Xu, Li et al. 2020), there is significant computational complexity involved in processing time-oriented metrics for location inferences. Although signal-strength-based metrics are inherently less computationally expensive for localisation inferences, significant post-processing can be done with these to extract location information (e.g., characterising propagation models). The methods presented by Dehghan, Farmani et al. (2012) use particle filters for both RSSI and AoA from an aerial point of view to localise RF sources. Another paper focussing on RSSI-based localisation uses a Kalman Filter to reduce the localisation error (George and Vadivukkarasi 2015). Papers like this provide promising improvements to RSSI-based localisation, which is notoriously coarse (Konings, Alam et al. 2019). Another study (Wang, Ji et al. 2017) depicts a system in which RSSI and AoA are combined in an aerial sensing fashion with custom path planning and algorithms to find Wi-Fi access points (the targets).

One area of research which bears similarity to post-disaster victim localisation is localisation of workers in underground mines. The similarity mainly lies in the similar inhomogeneous radio propagation environments. Localisation of workers in underground mines is an important aspect for health and safety. Ming, Hu et al. (2017) expresses the prevalence of RSSI-based techniques in inhomogeneous underground environments where significant signal propagation challenges are present. The paper also references many papers which attempt to use time-based techniques. Ge, Wang et al. (2015) discusses the inapplicability of time-based metrics to inhomogeneous mine environments, due to the inherent signal physics issues that are present in such environments (i.e., multipath). It is not a far stretch of the imagination to see that inhomogeneous mine environments bear a lot of similarity with post-disaster rubble environments. Within RSSI-based mine personnel localisation, there is a range of solutions proposed. Han, Yang et al. (2013) proposed a weighted centroid-based algorithm based on a Wireless Sensor Network (WSN) within the mine network, obtaining favourable results. However, Ge, Wang et al. (2015) comments that there is a significant instability with the system proposed by Han, Yang et al. (2013). Ge, Wang et al. (2015) goes on to explain the superiority of RSSI-based methods for localisation in mine environments. The author explains that proposed methods suffer from inherent environmental factors (such as multipath, diffraction, and shadowing from obstacles). There are many methods to account for these fluctuations and inconsistencies, the most accurate methods being Gaussian location algorithms (Jianwu and Lu 2009, Ge, Wang et al. 2015).

2.5.3 Processing of Radio Metrics for Localisation Purposes

Regardless of the radio technology used in the search and rescue system, there will be some processing of radio metrics to inform the location of target radio devices. These metrics vary depending on the implementation, and can be based on different characteristics of signals, such as frequency, time, and strength. Some common metrics used in such implementations include RSSI, TDoA and ToA. The processing of these metrics will differ depending on the type of metric. Signal-strength measurements are often used due to their intuitive variation with respect to transmitter and receiver distance (in free space conditions).

For the sake of simplicity, this subsection of the literature review will focus primarily on signal-strength-based radio metric processing. It is often difficult to characterise position as a function of RSSI due to the seemingly non-deterministic nature of RSSI measurements in inhomogeneous environments. However, as Koledoye, Martini et al. (2018) mentions, RSSI generally scales better as a localisation metric than time-based methods in such environments. This is because of the relatively simple hardware requirement of RSSI measurement as compared to the complex hardware of time-based measurement.

RSSI measurements often need to be pre-processed before being fed into positioning algorithms. This is to remove random fluctuations which are often present in continuous RSSI measurements. Oftentimes, a channel model is used to characterise distance as a function of RSSI. If there are multiple receivers measuring the RSSI, then these extrapolated distances can be used to trilaterally localise the RF target. The filtering step must occur before the readings are fed into the localisation algorithm. For a filtering algorithm, there are a few important qualities that must be upheld to be efficient, including minimal computational overhead, and minimal delay. This is to ensure the real-time nature of the localisation process. There are many different filtering algorithms (adapted from Koledoye, Martini et al. (2018)), including:

- Moving average filter: Fixed length with an equal weight assigned to each sample. This filter is suitable in situations where individual samples are *not* relatively important.
- Exponential moving average: Fixed length with exponentially decreasing weights applied to old samples. Useful for fixed nodes which 'self-localise'.
- Moving median: Similar to moving average, except uses median. Suitable for situations in which there are many erroneous readings (e.g., heavy non-line of sight).
- Moving mode: Similar to moving average and moving median. Better suited to unimodal RSSI environments such as Line of Sight (LoS) environments

These algorithms are compared to the Cramer-Rao Lower Bound. The Cramer-Rao Lower Bound gives the lower bound for the variance of an unknown, deterministic parameter (Koledoye, Martini et al. 2018, Paúr, Stoklasa et al. 2018). In this context, the parameter is distance between a transmitter and receiver calculated from RSSI. According to Koledoye, Martini et al. (2018), the simple moving average and exponential moving average filters suffer less from RSSI fluctuations than the moving median and moving mode filters. It is also found that the moving mode filter has the least favourable performance for range

estimation. The authors also express that the moving average-based filters have better computational efficiency, as they can be computed in real time, $O(1)$, in contrast to moving mode and moving median, which are $O(n)$ and $O(n \log(n))$ respectively (Koledoye, Martini et al. 2018). It was found that the equipment used as well as the environment (line of sight or non-line of sight) directly affects the RSSI distribution which in turn affects the filtering performance. Yet, filtering appeared to improve the range estimation over using raw RSSI measurements.

2.5.4 Other Radio Considerations

Systems which use RSSI as their method of localisation often have the issue of characterising distance as a function of RSSI, especially in inhomogeneous environments. This could be due to phenomena such as log-normal shadowing due to obstacles in the propagation environment, as well as multipath effects (Aditya, Molisch et al. 2018). According to Aditya, Molisch et al. (2018) and Qi, Kobayashi et al. (2006), high bandwidth time-of-arrival localisation is an attractive metric because of the fine time resolution provided by high-bandwidth ranging signals. This is due to the Fourier relationship between frequency and time. The limitation of high bandwidth ToA localisation is apparent in its namesake, high bandwidth. High bandwidth is a rarity considering the congested nature of RF spectrum. Additionally, it is advantageous to utilise technologies that already exist on the user's device, such as Wi-Fi and cellular technologies.

A common method of estimating the direction or angle-of-arrival of a received signal is through a phased array. As mentioned by Hood and Barooah (2011), phased array systems require very complex signal processing algorithms, such that the receiver is a coherent receiver. Processing of data from phased arrays is also known to be an inherently computationally expensive process. Additionally, phased arrays require the use of multiple antennae, which does not lend itself well to size and weight constraints of UAVs. It is also important to note that antenna size generally gets larger with lower frequencies, which poses issues at lower cellular frequencies, such as 700MHz, where antenna size can be prohibitively large.

Antenna design is recognised as a fundamental part of signal-strength-based geolocation. Many papers settle on using omnidirectional antennae and relying on post-processing for resolving any ambiguities that arise. However, well-designed directional antennae have the advantage of removing much of the post-processing required. Another research area that bears similarities to the research area concerned in this review is localisation of RF collars worn by endangered wildlife. Many parallels can be drawn between the two research areas, such as the shared goal of locating an RF source accurately. One such example of wildlife localisation using RF collars is detailed by Webber, Hui et al. (2017) whom discuss the applicability of UAVs to RF wildlife tracking. This is especially apparent considering the traditional method of traversing outback terrain on foot using a hand-held antenna and spectrum analyser. The authors also used Ansys Electronics Desktop to design a custom antenna for aerial wildlife tracking. The paper goes on to discuss the advantages of equipping their SDR system with a bandpass filter to suppress unwanted noise, however they rationalise the lack of filter because of the geographical remoteness of their experiments. The authors state that a bandpass filter would be required for an urban deployment. The authors also state the importance of using other beneficial radio

components such as a Low Noise Amplifier (LNA) for improving the signal quality. This is important in order to create discernible radio hotspots from the noise floor. Webber, Hui et al. (2017) also mentions the importance of investigating the noise that may be present from the UAV itself (i.e., the Electronic Speed Controllers (ESC), motors, GPS). By measuring the noise floor from an RTL-SDR with the UAV operating, the authors concluded that it was inconclusive as to whether the UAV was contributing to the measured noise floor.

Radio propagation is a large consideration in the context of radio-based search and rescue systems. Whilst a transmitted signal from an overhead aerial source would be inherently less susceptible to shadowing and path-loss from the perspective of a ground-based receiver, there are other considerations, such as the UAVs control frequency, noise from motors/ESCs, and so forth. Additionally, systems such as aerial base stations must ensure that there is sufficient uplink and downlink radio propagation characteristics to ensure good communication. One such method to ensure this, is to use directional antenna aboard the aerial base station. Using directional antenna on the aerial base station can significantly increase the transmit and receive gain in certain directions. Additional components such as power amplifiers, and low noise amplifiers can also assist in increasing transmit and receive gain. Most directional antennae are provided with a data sheet of their RF characteristics, such as gain, beamwidth, and radiation pattern. These are all useful parameters for planning a network. To properly plan the coverage of an aerial base station, it is important to consider how the beamwidths of the antenna determine the placement of the UAV, in terms of height and position. This consideration is reinforced by Sundaresan, Chai et al. (2018), in which backhaul antenna beam-widths are considered for high-bandwidth linking. Looking further into this problem, as the UAV moves (i.e., pitch, yaw, and roll), the coverage pattern on the ground will change if the directional antenna is mounted statically aboard the UAV. Some of these effects can be mitigated if the directional antenna is forced to remain nadir (i.e., always pointing at the ground directly below the UAV, regardless of pitch, yaw, and roll). This can be achieved through the use of a gimbal mechanism. Nadir is a familiar term in UAV camera-based mapping, whereby the gimballed camera performs compensation based on the pitch, yaw and roll of the UAV. This will allow the coverage pattern to move linearly with the spatial position of the UAV. There appears to be a lack of implementations which deploy directional antennae aboard UAVs, let alone nadir antennae.

2.6 Other Review

2.6.1 UAV Path Planning Algorithms for SAR

Many UAV-based systems present path planning algorithms only. This is a large aspect of any UAV-based localisation system. The intuitive approach would be to use wardriving (or more appropriately, war flying). However, there are many different approaches to this.

The system proposed by Yu and Ye (2019) uses D2D (Device-to-Device) communication and 3GPP proximity-based services (ProSe) for estimating the number of victims in the search area. The paper justifies development based on the claim that existing Public Safety Communication (PSC) networks are not suitable for emergency responses. D2D

and ProSe complement each other in disaster scenarios, ProSe allowing discovery and communication between mobile devices, and D2D providing a realisable full coverage solution for mobile devices. Yu and Ye (2019) also proposes an implementation of an LTE base station mounted aboard a UAV. The authors also claim that UAV-mounted base stations have the fundamental limitation of core network connection. This builds upon the UAV backhaul issue mentioned previously. Unlike other papers, the system proposed by the authors purports to “accelerate the rescuing process in emergency responses”. This is in contrast with systems which purport precise localisation of devices. The paper proposes a four-UAV implementation. By initially narrowing the search window with the UAVs, the number of devices in each ‘emergency area’ are counted based on the devices with D2D connections. The paper goes on to analyse and attempt to correct errors in victim counting algorithms. This paper seems to be based purely on simulation with no practical implementation.

Tomiyama, Takeda et al. (2020) proposes an algorithm for localising RF targets based on RSSI sensing in real environments. The authors claim that existing research which relies on localisation via RSSI alone does not account well enough for situations in which the target may be covered by obstacles. The authors propose to use the deviation of RSSI as the UAV traverses the terrain. A visual depiction of the algorithm is shown in Figure 1. The paper focusses on the implementation and analysis of the algorithm. From the scanning area, a smaller ‘scanning’ square (denoted by S_n) is set, with one of those vertices being the starting RSSI measurement point. The length of one side of the square is denoted as d . The UAV traverses the vertices of the square, measuring RSSI at each vertex. The vertex with the maximum RSSI is defined as the symmetric point, from which a new square is set. This new square is set such that the new square and the previous square share the vertex with maximum RSSI. The deviations between square S_n and S_{n-1} are then calculated. The distance d is changed if there is a large difference. Once the measured RSSI reaches a threshold (-50dBm in this case), the location of the target is said to be found. There is a trade-off between search time and success rate, depending on the value of d . The authors state, that with a value of $d=2.5\text{m}$, the success rate was 90%, however the search time was high. It was found that a value of $d=10\text{m}$ resulted in the lowest search time.

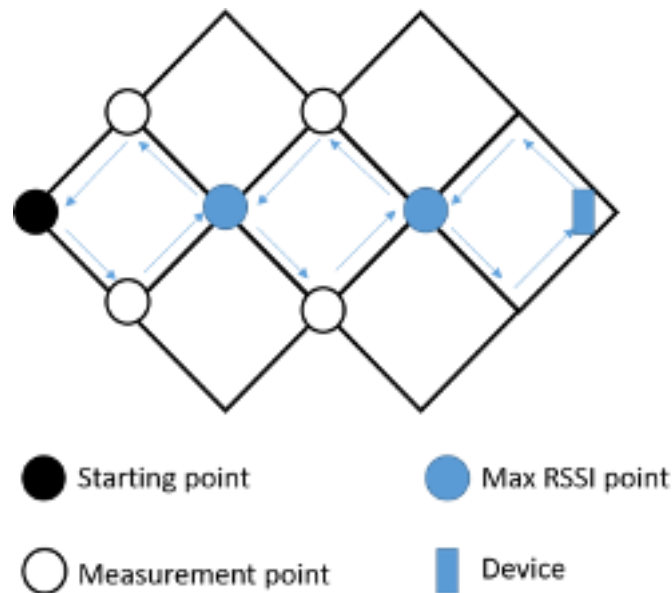


Figure 1: NLSS based algorithm, adapted from algorithm depicted by Tomiyama, Takeda et al. (2020)

Whilst not based on *conventional* disaster sites, Tiemann, Feldmeier et al. (2018) focusses on maritime search and rescue through UAV-based localisation. The proposed system equips a UAV with the capability to listen to mobile communications when the mobile device is still connected to mainland cellular base stations. The UAV also has the capability to deploy a cellular network to communicate with mobile targets. The authors propose that the base station and the mobile target will communicate using silent SMS to get regular RSSI updates. This can then be used to inform the localisation algorithm. This paper focusses on a Non-Linear Least Squares (NLLS) approach to localise the mobile target from the virtual anchor nodes on the predetermined UAV flight path, by measuring RSSI at these nodes.

Along with the parallel sweep path planning method, the paper also investigates other path planning methods such as expanding square, which starts from a central location and expands outwards in a rectangular fashion. Lastly, the sector search is investigated, whereby the UAV flies outwards (from the centre of the search area) at certain angles in order to localise mobile targets within the defined sector. This is depicted in Figure 2.

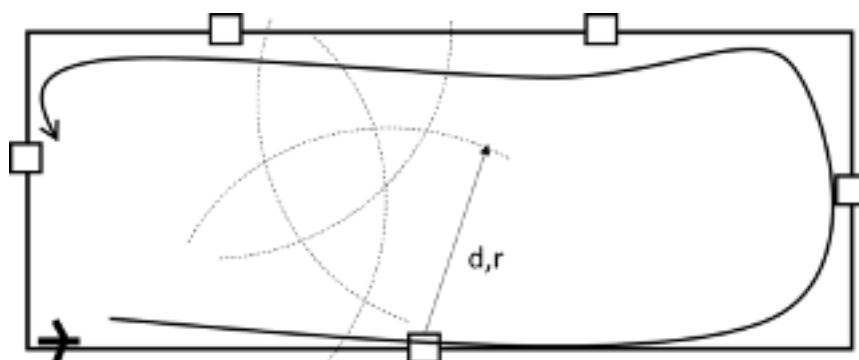


Figure 2: Proposed flying algorithm from Tiemann, Feldmeier et al. (2018)

Efficient path planning algorithms are an incredibly important aspect of automated UAV operations, especially with regard to battery life.

Another flight path algorithm which appears to be standard in capture of images for photogrammetry and creation of orthomosaics is grid-style flight paths. In flight planning software, this style of mapping requires the user to input the desired height at which to map the selected area, and also the longitudinal and latitudinal overlaps for sufficient orthomosaic stitching performance (Strecha, Küng et al. 2012). For search and rescue, grid-style mapping provides excellent coverage (Weldon and Hupy 2020), at the cost of very large datasets. Longitudinal and latitudinal overlaps of 80% are recommended by Weldon and Hupy (2020) in order to capture sufficient detail for visual search and rescue.

2.6.2 Special Considerations for UAV Implementations

There are a few limitations of UAVs at the time of writing. Whilst most UAVs have powerful flight computers, they do not necessarily support conventional computation and General-Purpose Input/Output (GPIO). Therefore, to capture data and perform processing with third-party sensors (e.g., SDR) onboard the UAV, an embedded computer will have to be mounted to the UAV. Unfortunately, all the added componentry decreases the battery life of the UAV, due to power consumption, and added weight. Therefore, an optimisation problem is born. Whereby the solution must strike a compromise between flight-time and onboard features. An ideal solution would have minimum componentry mounted aboard the UAV, while moving non-essential processing to a ground station.

Of course, some of the inherent issues with UAVs in this context is battery life and the ability to maintain a backhaul link (to existing infrastructure). There are a number of papers which propose solutions to these issues (Pascual Campo 2018, Pokorny, Ometov et al. 2018, Selim and Kamal 2018). Selim and Kamal (2018) mentions the advantages of 'tethering' UAVs to stable power sources and/or high-speed backhaul data links. This allows for theoretically unlimited flight time, and/or unimpeded network performance. However, the mobility of such a UAV would be limited by the tether. Selim and Kamal (2018) propose a grid-array of non-tethered UAVs for the purpose of network rehabilitation after large-scale natural disasters. In addition to the grid of UAVs, the authors propose three types of UAVs, a tethered backhaul UAV, a powering UAV, and a communication UAV base station. In the implementation, the communication UAVs construct the grid, while the tethered backhaul UAV communicates with the grid of communication UAVs via RF/Free Space Optical (FSO) link, and the powered UAV visits each UAV to charge it when required. This is a multi-UAV implementation which takes advantage of the mobility of untethered UAVs, yet also harnesses the advantages of tethered UAVs. While the authors only consider the mathematical optimisation of such a network, the implementation would be very difficult. Therefore, for the purpose of localisation in rough post-disaster scenarios, it is important to explore the most flexible mobile solutions (i.e., untethered).

In a similar fashion to vehicle-based networks such as cell-on-wheels, aerial-based networks require sufficient backhauling to make the system effective as a communications relay. In the context of localisation however, there is not much need for data backhaul. This is because the primary purpose of the aerial base station is to locate the target UEs, not enable large data transfers. A non-backhauled system is known as a standalone system. However, due to the computational complexity of running a full cellular stack (RAN and EPC), there is a large power draw, rendering such a system non-optimal for an untethered UAV. Therefore, if some of the processing can be relieved from the UAV, and

shifted onto a more capable ground station computer, the UAV will have more resources to remain in flight. Therefore, instead of backhauling the wide area network connection, the constituent components of the cellular network can be separated and backhauled (i.e., RAN to EPC backhaul link). Both Pokorny, Ometov et al. (2018) and Pascual Campo (2018) propose antenna steering backhaul links between ground stations and UAVs for the purpose of using the UAV as a communications relay. Sundaresan, Chai et al. (2018) introduces the challenges of designing a flexible, untethered aerial base station. The authors note that the rate at which the radio channel characteristics change for the RAN-UE connection is much higher than the EPC-RAN backhaul link. This is an important aspect to consider when optimising the backhaul and UAV placement. The communication mode of the EPC-RAN backhaul link is also an important consideration for optimisation. Additionally, antenna size can be prohibitive for such a backhaul link, especially at lower frequencies. At high frequencies, the directionality of a backhaul antenna needs to be much higher due to the greater propagation losses. The clear choice appears to be 2.4GHz Wi-Fi, this is due to the widespread compatibility of Wi-Fi with most single board computers. However, Wi-Fi operates in unlicensed spectrum, which can be congested in busy areas. The intricate details of different backhaul communication modes are further discussed by Sundaresan, Chai et al. (2018).

Another issue which impacts backhaul quality is the orientation of the UAV. This is because the orientation of the backhaul antenna also changes. The effects of this can be somewhat mitigated by using an omnidirectional antenna on the UAV. This is because the polarisation of an omnidirectional antenna would not change drastically during different vehicle movements (i.e., yawing). However, having a non-directional backhaul antenna on the UAV impinges on the link capability.

2.7 Defining the Opportunity

Within the research field of UE localisation via aerial base station (or SAR more generally), there appears to be a lack of research in which highly directional nadir antennae are used. Additionally, there are very few systems which utilise higher-layer metrics of the LTE stack, whilst maintaining compatibility with Commercial Off-The-Shelf (COTS) UEs. Furthermore, there is a lack of SAR systems which separate the cellular stack onto separate machines. Therefore, the findings from this literature review warrants the development of a UAV-based system which employs a separated cellular stack for the purposes of search and rescue localisation, utilising nadir directional antenna and higher-layer signal-strength-based metrics.

The context and implementation of such a system within post-disaster management and organisation also needs to be considered. This alludes to the use case of such a system within the search and rescue process. Such a system can be used as an initial tool that's deployed which provides location inferences (i.e., first response tool). Alternatively, such a tool can be used more for highly accurate location prediction mid-way through the search and rescue process. Ultimately, this decision needs to be made after assessing the accuracy of such a system and assessing the needs of search and rescue teams. A paper which focused on the use of UAV systems by dedicated SAR groups sent a survey to various SAR groups and obtained responses on ideal operation characteristics for similar

systems (Półka, Ptak et al. 2017, Półka, Kuziora et al. 2018). It was found that respondents were not overly focused on high accuracy of a system and were looking for a system which would provide early insights on victim location (i.e., first response tool). Such a system should ultimately accelerate the victim localisation and extrication process.

3. Informing Design from Research

3.1 Developing Requirements

Generally speaking, the gap in research should inform the target area of subsequent research. The research question of this thesis is based on gaps in research isolated in chapter 2.

A certain knowledge of the state of the technology must be known to translate areas of research novelty into distinct functions and features of a system. During the literature review, a simultaneous exploration into the state of relevant technology was taking place. Running these two processes in conjunction was a mutually beneficial process as it allowed for more informed and salient function and feature definition.

The research novelty highlighted in subsection 2.7 defines a set of high-level features, functions, and architecture insights for the system. The novelty highlighted in this subsection can be broken down into several domains:

- Architecture: The way in which features are implemented in an overall system
- Feature: A distinct aspect/attribute which enables a function
- Function: An action, process or task performed to achieve an objective

Some of these research-extrapolated features, functions and architecture insights are summarised in Table 1.

Table 1: Features, functions and architecture insights gained from literature review

Insight	Premise, Cause or Novelty	Domain
System based on a UAV	Aerial vehicles are inherently less impeded than ground-based vehicle	Architecture
Highly directional antenna in nadir fashion	Highly directional antennae are inherently more selective in receiving/transmitting RF signals	Feature
Segregated cellular stack over directional link	This is deemed to be complementary to UAV constraints	Architecture
Maintain compatibility with COTS UEs	Using COTS UEs is more representative of a 'real-world' SAR scenario	Function
Simultaneously localising target devices and mapping the area of interest	Provides a more salient depiction of the target device in the area of interest	Function

The proposed system is an implementation of an aerial base station, geared towards search and rescue deployments.

More specifically, the proposed system will have the following functions:

- Simultaneously collect cellular signal data from mobile phones in the scanning area *and* collect photo imagery from the scanning site for photogrammetric mapping.
- Deploy an LTE cellular network from a Software Defined Radio (SDR) frontend from which mobile phones in the scanning area can connect to. The SDR enables the deployment of an open-source cellular stack.
- Utilise a cellular metric (e.g., Energy Per Resource Element (EPRE)) to build a 'heat map' of signal-strength metrics with respect to position
- Utilise the radio map to infer the location of individual mobile phones in the scanning area

These have been derived with respect to the state of relevant technology. All these functions were curated with adherence to research novelty. In the existing research, there is a significant lack of aerial base station implementations for the purpose of SAR. To the best of the authors knowledge, the proposed implementation is the first aerial base station system intended for search and rescue which:

- simultaneously localises target devices and maps the surrounding area
- utilises a nadir directional antenna for enhanced localisation
- segregates the LTE Evolved Packet Core (EPC) and eNB such that they run on separate processors

3.2 Functional Hierarchy

A functional hierarchy shows how a complex function or objective can be decomposed into constituent functions. In this case, these functions are further decomposed into features and enabling hardware based on function to feature relationships. The enabling hardware is then allocated to a platform (UAV or ground station) according to the nature of the hardware.

The functional hierarchy is shown in Figure 3. This figure details the workflow which translates a high-level objective into categorised hardware.

An awareness of research-proposed workflows and technology limitations was required to transition from the system-level objective to the functions, from functions to features, and finally, to enabling hardware. This transition is where the synergy of research and corresponding state-of-the-art technology was exploited. The basis of exploring this transition was a mix of literature review and researching open-source frameworks (e.g., different open-source cellular deployments). The transition to responsible hardware was more of a high-level engineering optimisation problem.

The categorised hardware forms the base elements of the product architecture.

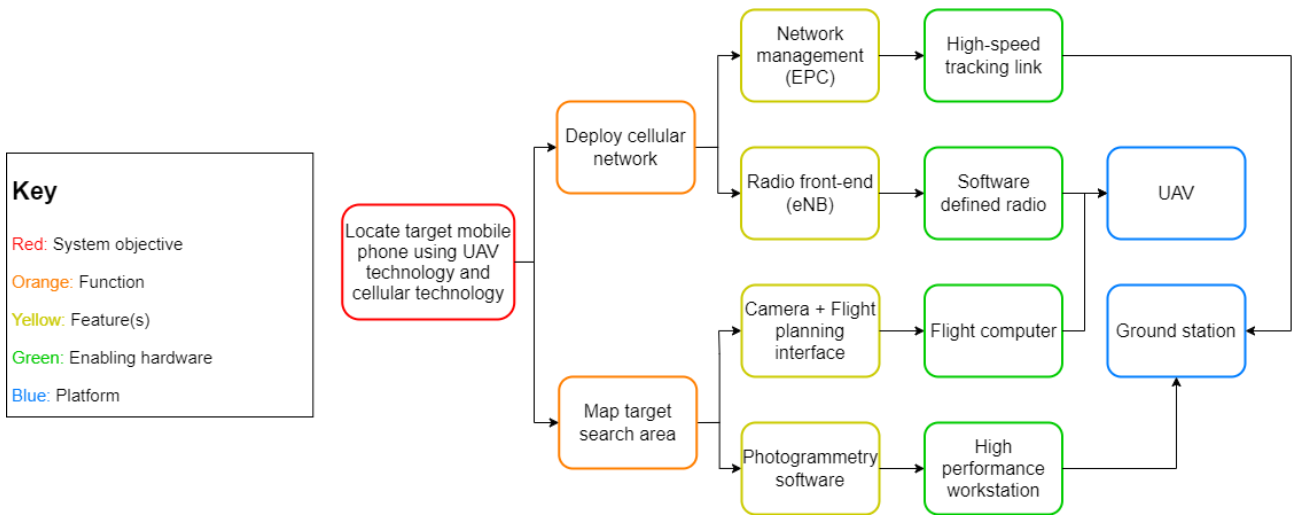


Figure 3: Proposed high-level functional hierarchy

3.3 Product Architecture

A product architecture shows how a system can be decomposed into components according to logical and physical layout. In this case, the product architecture is decomposed based on system (platform) to module relationships.

The product architecture was made after making the functional hierarchy. The product architecture was formed with an awareness of the limitations of the project scope, as well as the state-of-the-art of the constituent technologies (i.e., UAV technology, Software Defined Radios). The product architecture can be seen in Figure 4. After the lowest-level components were specified, the project scope and resources were considered to decide which components should be COTS, modified, or custom built.

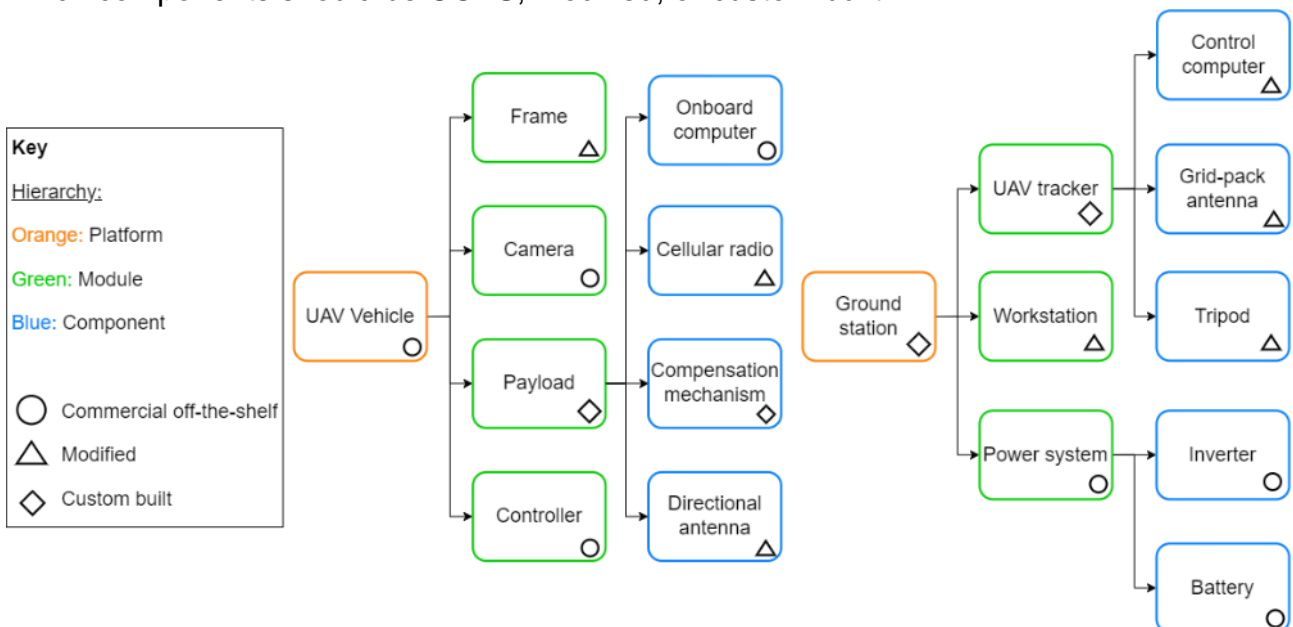


Figure 4: Proposed high-level product architecture

3.4 Proposed Modus Operandi

While deciding which hardware components should be purchased off-the-shelf, modified or custom built, a study of the flow of data and the requisite software processing resulted in the following proposed design.

Flight planning software is used to select the area of interest that the UAV will scout and map. All the parameters from the UAV (including UE connection status) can be observed from the ground station. Once the UAV is connected to the target UE, the UAV will begin the mapping process, flying a grid pattern over the area of interest. Once the UAV has completed its flight plan, it will fly back to its 'home' position. The relevant data will be processed immediately by the ground station, from which the radio heat map will be generated and overlaid on top of the orthomosaic of the area of interest. In this context, orthomosaic refers to the collection of many high-resolution images, and the subsequent stitching of these images together to form a high resolution, larger image. This heat map will be geo-referenced, and accessible via Geographic Information System (GIS) software, such that location hotspots can be given directly to first responders.

4. UAV Implementation

4.1 Baseline Vehicle

4.1.1 Vehicle Overview

Aerial base stations encompass many different vehicle types, including quadcopters, fixed-wing Vertical Take-Off and Landing (VTOL) aircraft, and hexacopters to name a few. The applicable vehicle types can be broken down into two main categories: Fixed-wing and multicopters.

For the purposes of this research, multicopters are better suited due to their enhanced mobility and ability to hover. From considering the available multicopters on the market, the DJI Matrice 100 (M100) quadcopter was selected. The Matrice 100 sports a 1200g payload capability, supports Robot Operating System (ROS) and has a very modular airframe which allows for extensive customisation.

The Matrice 100 has four DC motors each attached to a separate carbon fibre rod. All of which are attached to the main chassis. The Matrice 100 is controlled via a DJI N1 flight controller which receives control signals from the DJI GL-658C remote controller. The N1 flight controller also collects information from the onboard sensors (e.g., GPS, Inertial Measurement Unit (IMU)) and uses these in conjunction with the remote-control signals to inform the control signals sent to the ESC for each motor. The Matrice 100 is unique in the fact that it is enabled with Robot Operating System. The key specifics of the Matrice 100 are listed in Table 2.

Table 2: Key specifications of DJI Matrice 100, sourced from DJI (2019)

Parameters	Value
Max. Take-off weight	3600g
Max. Payload weight	1200g
Max. Speed	22 m/s
Max. Wind Resistance	10 m/s
Hovering time with 1kg payload (TB48D battery)	16 mins
Operating temperatures	-10°C to 40°C
Estimated LoS transmission distance	Federal Communications Commission (FCC) rating: 5km
Operating Frequencies	Video: 5.725 - 5.825GHz Data: 2.400 - 2.483GHz

The Matrice 100 is marketed as a 'developer UAV'. The Matrice 100 has a range of available chassis mounts that can be adapted and changed for different payloads. The Matrice 100 can be fitted with a gimbaled camera.

The camera chosen for this system was the DJI Zenmuse X3. The Matrice 100 supports many different DJI-made cameras, however, the X3 is the lightest camera of the available selection, and still retains excellent performance. The X3 is capable of 4K video recording and full-HD still shots. The X3 is fully gimbaled and can move independently of the vehicle.

The Matrice 100 can be fitted with either a DJI TB47D battery or a TB48D battery. The TB47D battery is slightly lower capacity, at 4700 mAh, and is also slightly lighter than its higher-capacity counterpart. The TB48D has a capacity of 5700 mAh and is 76g heavier than the TB47D. A second battery compartment can also be mounted upon the M100 to allow for dual battery configuration, as seen in Figure 5. This helps to extend the flight time of the M100. This second battery compartment plugs into a XT60 connector on the UAV chassis. There are two extra XT30 connectors on the chassis, which can be used to power peripherals. The primary battery compartment position was changed such that it was on the top side of the UAV. This allowed the payload mechanism to be mounted below the UAV as intended.



Figure 5: Baseline Matrice 100 UAV with dual batteries. Image sourced from DJI (2019)

The Matrice 100 communicates with the GL-658C remote controller via the frequencies mentioned in Table 2. A tablet or phone can be connected to the Universal Serial Bus (USB) port of the GL-658C for control and observation. The M100 is controllable via the DJI GO app which is supported by major mobile operating systems.

4.1.2 Vehicle Software

The DJI Matrice 100 ships with proprietary software and control protocols. In many respects, the Matrice 100 is quite locked down: third-party controllers and cameras are not supported. For the purposes of this research, this is a nonissue.

Whilst the control software is proprietary, DJI have built their own Onboard-SDK (Software Development Kit) such that their enterprise aircraft can communicate with third-party systems for integrated solutions. The Onboard-SDK can communicate via ROS, Linux

Application Programming Interfaces (API), and some serial-enabled microcontrollers. The Onboard-SDK ROS wrapper allows for control and observation of aircraft parameters, including, but not limited to:

- Flight actions (i.e., take-off, land)
- Advanced flight control (i.e., path planning)
- Camera and gimbal control
- Aircraft status data (e.g., GPS position, height above take off, battery level)

DJI also provide a simulation environment for the Matrice 100. This is enabled through the DJI Assistant PC/Mac app. DJI Assistant allows the user to change the Onboard-SDK parameters. The DJI Assistant app also allows the following functionality:

- Change basic UAV settings
- Show the simulator
- Upgrade firmware (on UAV and controller)
- Extract flight data from UAV

For this project, the simulator was not used. In addition to the output rate parameters, the user can change the data type of various parameters. This changes the message representation in the relevant ROS topic messages.

The software versions that were loaded onto the DJI components are shown in Table 3.

Table 3: Software versions of constituent components

Description	Version
M100 N1 Flight Controller	1.3.1.82
DJI GL658C Remote Controller	1.7.80
DJI Go (IOS App)	3.1.68
DJI Assistant Version	1.2.4

4.1.3 Vehicle Control

The DJI GL-658C controller is used to control the DJI Matrice 100 aircraft. The GL-658C has a USB port into which a smartphone or tablet can be plugged. The DJI Go app is used as the control interface for the UAV. The app shows important details about aircraft status, camera settings, battery life and so forth. An annotated screenshot for the DJI Go interface is shown in Figure 6.

There are a variety of apps which assist with flight-plan automation. For the purposes of this system, photogrammetry flight planning software was sufficient for planning the flight paths required for testing. This software serves a double purpose, because photogrammetry data is being captured as part of the workflow.

The flight planning software used for testing was Pix4DCapture. Pix4DCapture allows a variety of different flight planning algorithms. The following settings can be tailored to suit a custom mission plan:

- Horizontal and vertical overlap: The amount (as a percentage) that adjacent flight paths overlap with each other
- Flight height: Adjustable between 10m and 500m
- Camera settings: Such as white balance and trigger mode

An annotated screenshot from the Pix4DCapture app is shown in Figure 7.

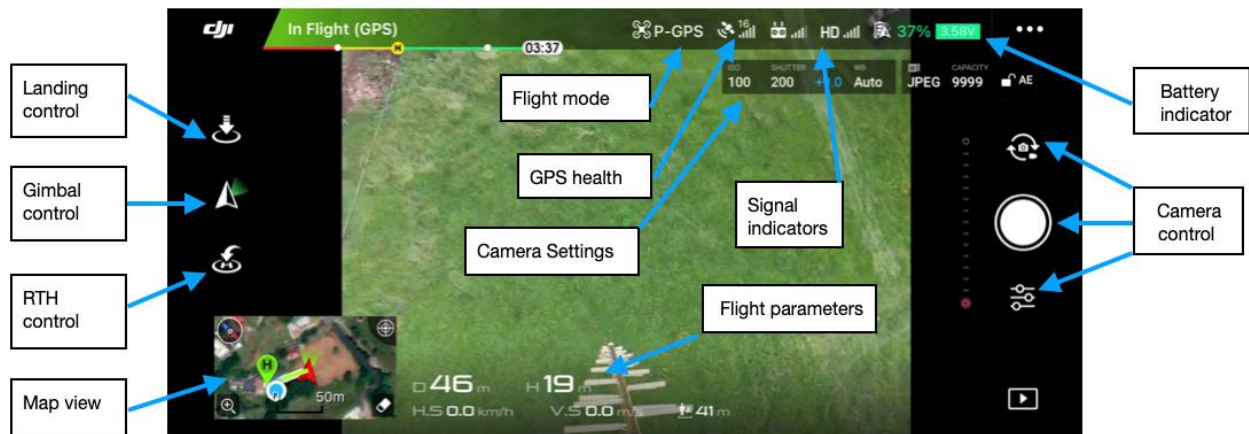


Figure 6: Annotated view of DJI Go App

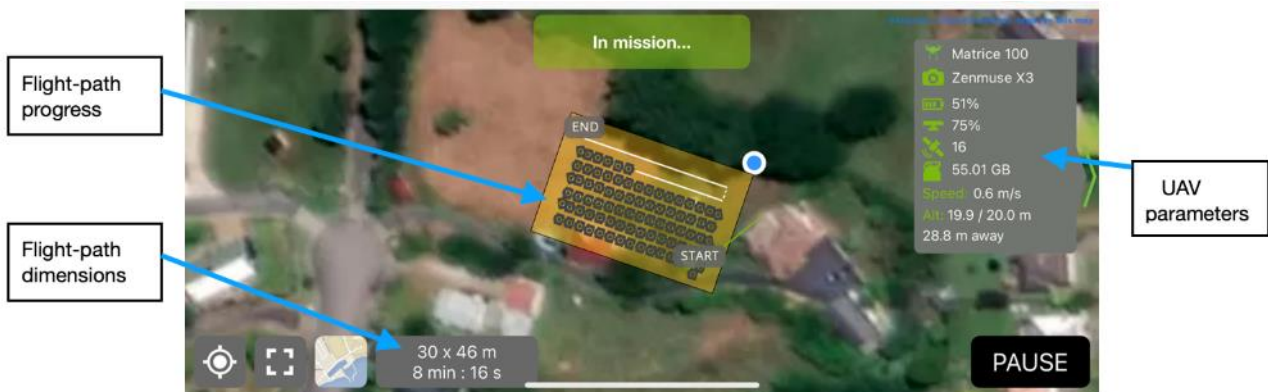


Figure 7: Annotated view of Pix4DCapture App

4.2 Payload Hardware

4.2.1 Cellular Radio

Due to the nature of the system as an aerial base station, particular attention needs to be given to the cellular hardware. Software Defined Radios are modular and capable devices which can be deployed as a cellular Radio Access Network (RAN). The SDR chosen for the proposed implementation was a Nuand BladeRF xA4. The BladeRF xA4 appeared to be a well-supported radio by the cellular firmware chosen, srsRAN. The BladeRF xA4 also appears to be one of the lightest options available, with rugged mounting hardware.

The key parameters of the BladeRF xA4 SDR are shown in Table 4, information sourced from Nuand (2022).

Table 4: Key parameters of Nuand BladeRF xA4 SDR

Parameters	Value
Frequency Range	47MHz - 6GHz
Maximum sampling rate	61.44MHz
Field-Programmable Gate Array (FPGA)	Altera Cyclone 5
Connectivity	USB3
RF Input Output (IO)	2 x Transmitter (TX) SubMiniature version A (SMA) ports and 2 x Receiver (RX) ports. Supports 2x2 Multiple-Input Multiple-Output (MIMO)

The BladeRF SDR is loaded with a specific FPGA image which allows it to be paired with an open-source cellular stack called srsRAN.

The srsRAN suite (previously srsLTE) is an open-source cellular stack which allows for a full implementation of an LTE network, including EPC (Evolved Packet Core) and eNB RAN (Radio Access Network). The latter is commonly abstracted as the evolved Node B (eNB). This cellular stack is made by Software Radio Systems, founded in Ireland (Gomez-Miguel, Garcia-Saavedra et al. 2016). This open-source cellular stack appeared to have a large support base, as well as explicit support for the BladeRF series of SDR's. There are other options available, and due to the standardised nature of LTE, different offerings can be combined in a segregated architecture e.g., a srsENB paired with and OpenLTE EPC. Initially, srsRAN was released to be compatible with LTE release 8 (Gomez-Miguel, Garcia-Saavedra et al. 2016), but has since been made compatible with LTE release 10 (Zhu 2018).

4.2.2 Onboard Computer

Due to the weight-sensitive nature of the UAV, the chosen class of computers was limited to Single Board Computers (SBCs). The Raspberry Pi 4 was chosen due to its performance, and support. The Raspberry Pi runs Ubuntu Server 20.04, and contains installations of ROS Noetic, srsRAN and all the other constituent software packages. The Raspberry Pi interfaces with the BladeRF xA4 SDR via USB. The Raspberry Pi 4 hosts the srsRAN eNB. The srsRAN EPC is hosted upon a more powerful ground-based Ubuntu workstation.

The features of the Raspberry Pi 4 SBC are described in Table 5.

Table 5: Features of Raspberry Pi 4 SBC

Specification	Value
CPU	Quad Core A72 Cortex Advanced Reduced Instruction Set Computer (RISC) Machine (ARM) 64-bit processor @ 1.5GHz
RAM	8GB LPDDR4-3200 RAM
Networking	2.4GHz/5GHz 802.11AC Wi-Fi and Gigabit Ethernet
IO	2 x USB3.0 and 2 x USB2.0 ports
GPIO	28 pins (3 hardware Pulse Width Modulation (PWM) pins)

The Pi controls the execution of software upon the UAV. The Pi 4 contains the connections as seen in Table 6.

Table 6: The connections between the onboard Pi and other components

Connection/Interface	To	Purpose
USB	BladeRF xA4 SDR	Controlling the RAN
Universal Asynchronous Receiver-Transmitter (UART)	DJI N1 flight controller	Subscription to flight computer data (through Robot Operating System topics)
Wi-Fi	Ground station MikroTik Metal Wi-Fi Access Point (AP)	Transferring Robot Operating System topics to Ground Control Station (GCS) and allowing remote control

4.2.3 Directional Antenna

The payload of the UAV includes a servo mechanism which is used to move a multi-band cellular ‘yagi’ broadband directional antenna. This antenna supports GSM, Code-Division Multiple Access (CDMA), third generation (3G), fourth generation (4G) and fifth generation (5G) frequencies. The operating frequencies of the antenna are split into three main bands, as seen in Table 7. The horizontal and vertical beamwidths change depending on the frequency, as seen in Figure 8. While the antenna is referred to as a yagi antenna, it is technically a log-periodic antenna. This fact can be discerned from the mechanical design of the elements, which is essentially two yagi antenna fused together with the feed point at the end of the antenna.

The cellular antenna originally came with a plastic shroud which covered the director elements. However, this shroud was quite heavy, constituting over 65% of the total weight of the antenna. This was removed, and the total weight of the antenna was reduced to 250g. The centre of mass of the antenna is situated near the base of the antenna.

Consequently, the balance point of the antenna is only 30mm from the base, therefore reducing the torque required to move the antenna.

The boom of the antenna is attached to a metal backplate, which acts as a shield to attenuate any signals that may be received *behind* the antenna. This is quite useful, because the UAV communicates with the controller within the 2.4GHz Industrial, Scientific, and Medical (ISM) band, which is within the resonant range of this antenna. Sufficient bandpass filtering occurs within the SDR, so this is a non-issue for cellular performance. The measured return loss of this antenna within the resonant bands is shown in Appendix A.

Table 7: Specifications of cellular antenna for different frequency ranges

Frequency Range	698~960MHz	1710~2700MHz	3300~3800MHz
Gain (dBi)	9±1	9±1	9±1
Hor. Beam width (°)	85±15	80±15	75±15
Ver. Beam width (°)	60	65	60
Front-to-back ratio (dB)	≥15	≥15	≥15
Voltage Standing Wave Ratio (VSWR)	≤1.5	≤1.5	≤1.5

The vertical and horizontal beamwidths of the antenna are shown in Figure 8 for more clarity.

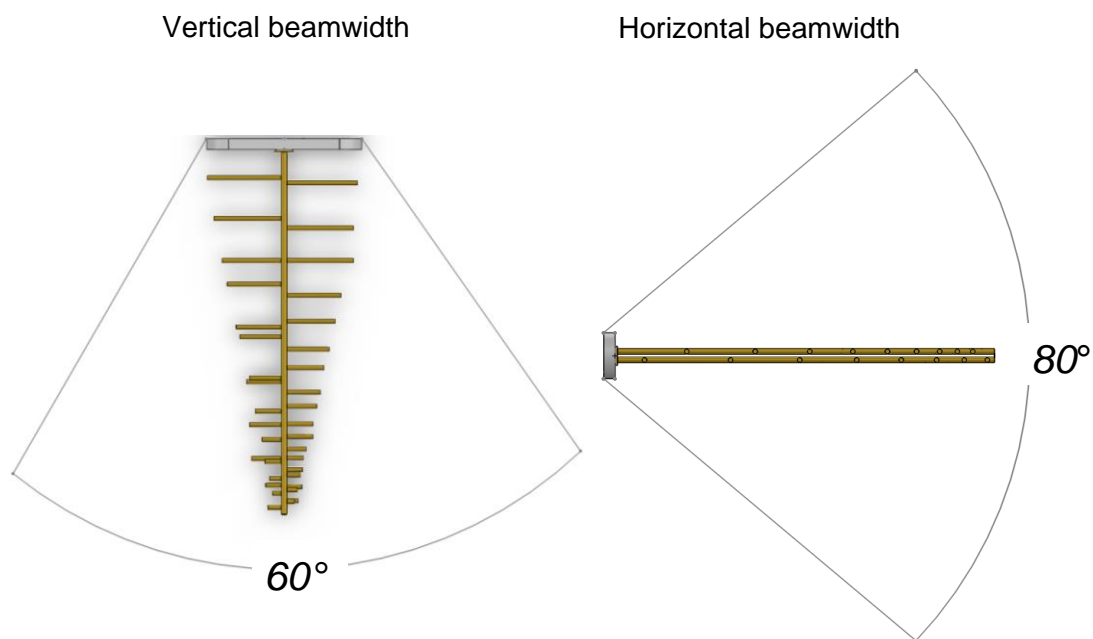


Figure 8: The approximate vertical and horizontal beamwidths of the directional antenna

Whilst the antenna is resonant within the frequency ranges mentioned in Table 7, the performance varies between these bands *and* within these bands. Return loss is a good measure for the resonant performance of the antenna. Return loss plots of the antenna in these bands are detailed in Appendix A. These return loss plots show that the greatest performance (return loss > 40dB) within the 1700-2700MHz band, which is the band used within this system.



Figure 9: Three renders showing the operation of the antenna upon the M100

4.2.4 Nadir Mechanism

The antenna is attached to a servo mechanism which is designed to keep the directional antenna in nadir position during flight. Which essentially means that the antenna will always be directed to the point (on the ground) which is directly below the UAV, regardless of vehicle pitch. This can be seen in Figure 9, which shows the take-off/landing position, static flight position and the antenna compensation position respectively. The mechanism was designed to attach directly to the bottom chassis rails of the vehicle. The mechanism was also designed such that the UAV would retain its centre of gravity whilst in flight. This was achieved by shifting the mount point of the servo mechanism slightly off-centre towards the rear of the UAV.

This mechanism is only single axis. Which means that the servo mechanism only compensates the angle of the antenna based on the (forward/backward) pitch of the vehicle. Whilst it would be advantageous to have more than one axis of movement (i.e., to compensate for roll as well), such a mechanism would exceed the payload capacity of the Matrice 100.

Table 8: Specifications of Hi-Tec HS755HB servo

Specification	Value
Voltage Range	4-6V (DC)
Stall torque (6V)	13.2 kg.cm

Specification	Value
Weight	110g
Travel per μsec	$0.109^\circ/\mu\text{sec}$
PWM Range	556-2410 μsec

The antenna servo mechanism is a Hi-Tec HS-755HB metal gear servo. Table 8 shows the specifications of the HS-755HB servo. The servo is paired to a servo mounting block, which is a mechanism designed to reduce lateral loading on the servo shaft. A mount was designed to bolt onto the chassis rails of the M100 and secure the mounting block assembly. A separate antenna mount was designed to interface between the antenna mounts and the aluminium hub shaft of the servo mounting block. Renders of this mechanism are shown in Figure 10.

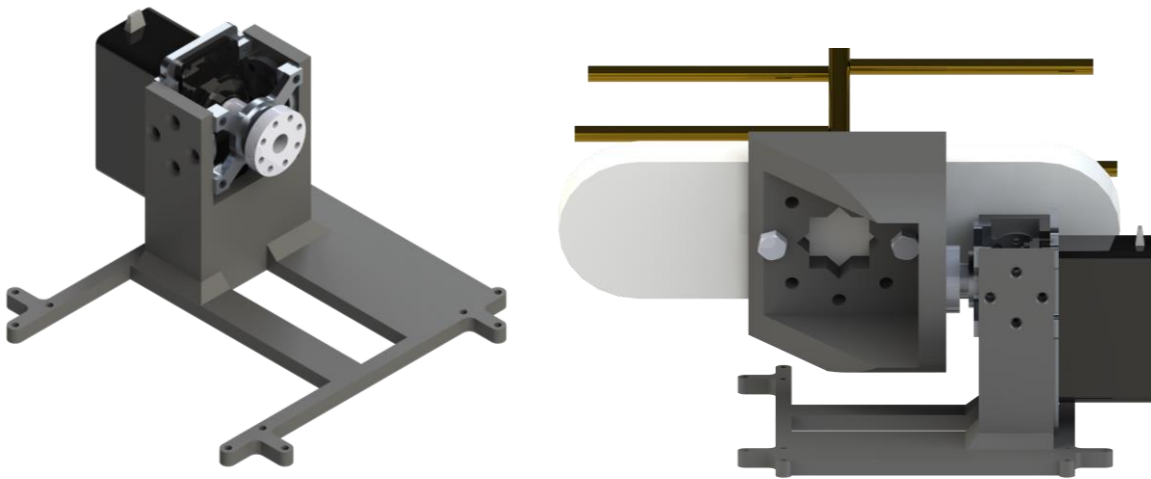


Figure 10: The antenna compensation mechanism which mounts to the M100

4.3 Payload Control

4.3.1 Nadir Antenna Control

As mentioned previously, the onboard Raspberry Pi controls the angle of the antenna compensation servo. The servo signal line is connected to a PWM GPIO of the Pi 4.

There are two data inputs for this control script, these are the ROS topics *attitude* and *height_above_takeoff*. The *attitude* topic takes raw measurements from the UAVs IMU sensor. The *height_above_takeoff* topics takes measurements from the UAVs GPS sensor. A Python script was written to interpret the messages from both topics and output an appropriate control signal to the antenna servo. However, to setup the script, a ROS node must be initiated. In the script, the ROS node is initiated within a function *listener()*, shown below:

```

def listener():
    rospy.init_node('listener')
    height_sub = rospy.Subscriber('height_above_takeoff', Float32, check_height)
    attitude_sub = rospy.Subscriber('/dji_sdk/attitude', QuaternionStamped,
    calculate_control_signal)
    rospy.spin()

```

The first line of the *listener()* function initiates a ROS node under the name 'listener'. Each node must have a unique name in order to subscribe to topics. The second and third lines of the function initiate different subscriptions for the *height_above_takeoff* and *attitude* topics. Each of these subscriptions call a different function in the main script. The final line of the *listener()* function initiates *rospy.spin()*. Rospy is the Python client library for ROS, and the *spin()* function essentially acts as a *while* loop, and prevents the program from executing until the user exits the program (i.e., Pressing Ctrl+C in terminal).

As seen in Table 8, the HS-755HB has a PWM range of 556-2410 μ S, and a resolution of 0.109 $^\circ$ / μ S, therefore the required control signal for the mechanism can be calculated. To control the servo, a 50Hz PWM signal is used. This results in a PWM period of 20ms. A pseudo-code function for the algorithm is shown below. The function takes the pitch angle as an input:

```

def servo_control(self, pitch):
    print("Pitch - ", pitch)
    if pitch > 0: #+Ve pitch_angle corresponds to forward pitch
        control_usec = 1400-(pitch*9.0909090909)
        control_percentage = control_usec*(1/200)
    else: #-Ve pitch_angle corresponds to backwards pitch
        control_usec = 1400+(pitch*9.0909090909)
        control_percentage = control_usec*(1/200)
    p.ChangeDutyCycle(control_percentage)
    return control_percentage

```

As seen in Figure 11, the mid-point of the antenna is at 1.4ms PWM pulse width. The code snippet above shows that when the UAV is pitched forward the control signal generated is subtracted from the mid-point PWM period (1400 μ S) by a value directly proportional to the pitch angle. This is reversed for the case where the UAV is pitching backwards. The scaling factor 9.90909 corresponds to the fraction $\frac{100}{11}$. This is calculated from the 0.109 $^\circ$ / μ sec travel of the servo (as seen in Table 8), whereby $0.109 \times \frac{100}{11} = 1$. The control percentage is calculated by dividing the pulse width value by 200, as this calculates the percentage value of the pulse width value as a function of the PWM range.

Figure 11 shows the position of the cellular antenna with respect to the servo control signal value.

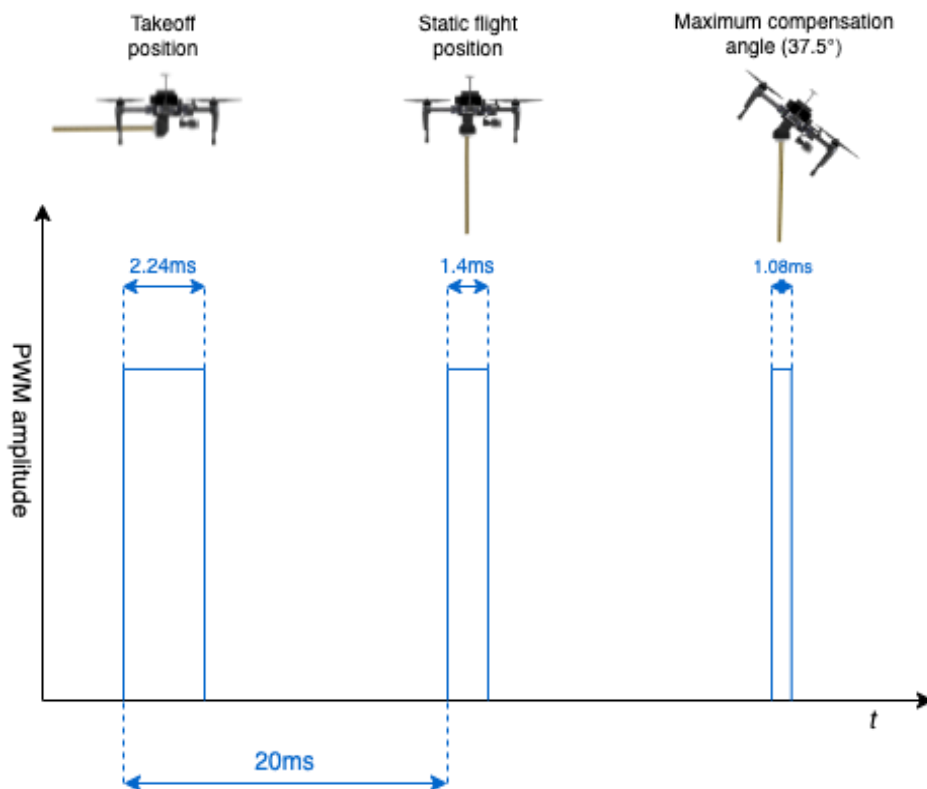


Figure 11: PWM control of the antenna compensation servo

4.4 UAV Operation

4.4.1 Flight Planning Considerations

With regular photogrammetry, the important parameters to determine the quality of the output photos are:

- UAV height
- UAV flight speed
- Front and side overlap (also referred to as latitudinal and longitudinal overlap respectively)
- Camera settings

Because the principle of operation of the system assimilates closely with UAV-based photogrammetry, these parameters are used to calculate flight path parameters.

One characteristic which is very important in UAV-based photogrammetry is Ground Sampling Distance (GSD). In traditional UAV photogrammetry, this is the effective cm-per-pixel resolution of the camera and is directly influenced by camera altitude.

This analogy can be transported to radio measurements as well. From a two-dimensional aerial perspective, the vertical GSD is defined as the GSD in the same direction (heading) of the UAV. The horizontal GSD is said to be the GSD in the direction orthogonal to the heading of the UAV.

When the radio is taking cellular samples, the samples are taken at approximately 75Hz. This is configured in the srsRAN scripts. Therefore, the biggest factors which control the effective ground sampling rate of the radio is UAV flight speed *and* parallel flight path distance. If these factors are analysed with respect to the polarisation of the antenna (as seen in Figure 12), the horizontal beamwidth corresponds to the vertical radio GSD, and the vertical beamwidth to the horizontal GSD. Given that the UAV flight speed directly affects the effective ground distance between vertical samples, the UAV must be flying slow enough to sample the ground at a rate which would receive a cellular signal sufficiently, yet fast enough to make efficient use of UAV battery power. For example, if the vertical radio GSD is set to a typical mobile phone size of 5 inches (12.7cm), the maximum flight speed to fulfill a vertical radio GSD of 12.7cm is:

$$t = \frac{1}{75} = 0.0133 \text{ seconds}$$

$$v = \frac{d}{t} = \frac{0.127}{0.01333} = 9.525 \text{ m/s}$$

Therefore, the maximum flight speed of the UAV will be approximately 9.5m/s to satisfy a vertical radio GSD of 12.7cm. The main factor which affects the horizontal GSD is the distance between parallel flight paths (assuming a grid pattern mapping). The distance, d , between the parallel flight paths in a grid-style flight plan can be changed to make the distance between parallel radio samples smaller. In photogrammetric flight planning software, the distance between adjacent, parallel flight paths is determined primarily by the height of the UAV, as well as the percentage of side overlap between samples. In this case, the UAV height will determine the overlap between radio samples. This is because the vertical and horizontal beamwidths of the antenna are fixed. To strike a trade-off between battery life and area coverage, one (or both) of these radio GSDs needs to be compromised. If the vertical GSD is compromised, then the UAV will have a greater flight speed. If the horizontal GSD is compromised, the parallel flight paths will be further apart. Within flight-planning software, there are limits to both flight speed and parallel flight path distance (d). Due to the complex polarisation interactions when the UAV is turning corners, the data at these vertices can be interpolated or scrubbed.

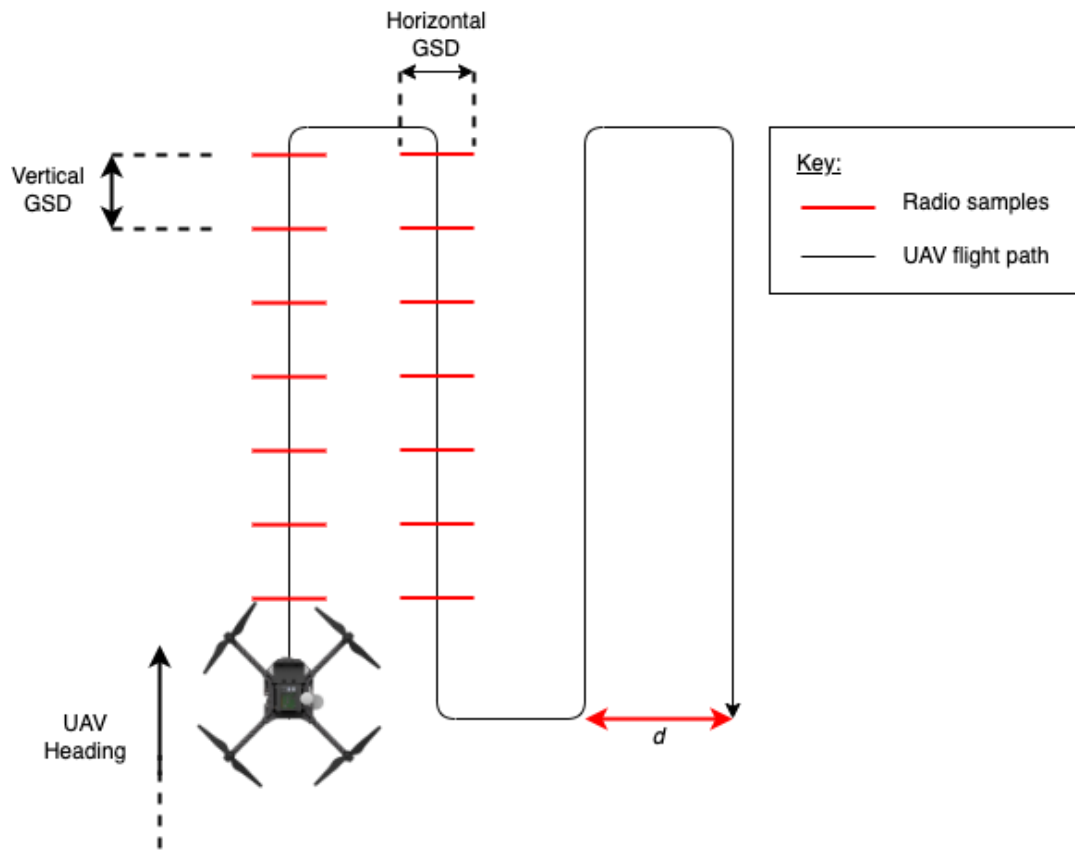


Figure 12: A depiction of the horizontal and vertical GSDs of radio samples

4.4.2 Antenna Beam-width Considerations

Another important characteristic that feeds into the flight height is vertical and horizontal beam widths of the onboard directional transmitter antenna. The horizontal and vertical beam widths indicate the angles (from each axis) of highest gain of the antenna, as seen in Figure 8. The gain of the antenna across all its resonant frequencies is 9 ± 1 dB. This gain is strongest *within* the bounds of the vertical and horizontal beamwidths and is most concentrated UAV along the boresight of the antenna. The beam-width illumination area (or coverage area) directly affects the required sampling rate of the system.

The frequencies being used for testing are within the central 1710~2700MHz band of the antenna. As mentioned previously, there are different vertical and horizontal beamwidths for each different resonant band of the antenna. The effective coverage areas for this band at different flight heights is shown in Figure 13. This shows the approximate area in which the antenna transmits with the highest gain. Note, the realistic radiation footprint is elliptical in accordance with directional antenna radiation pattern, as seen in Figure 14. This radiation pattern was modelled in Ansys High Frequency Simulation Software (HFSS).

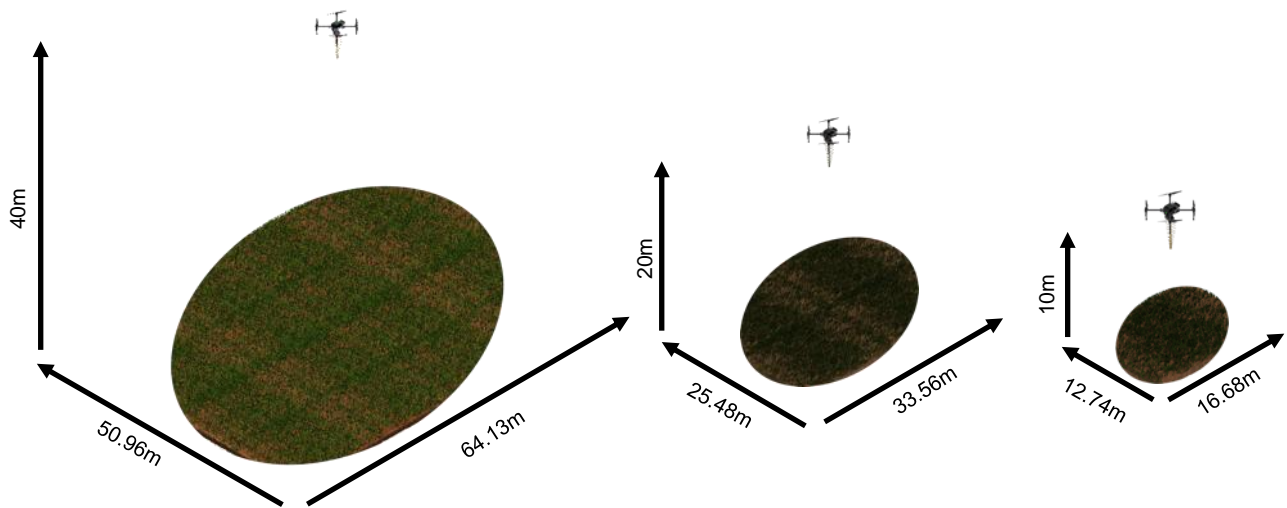
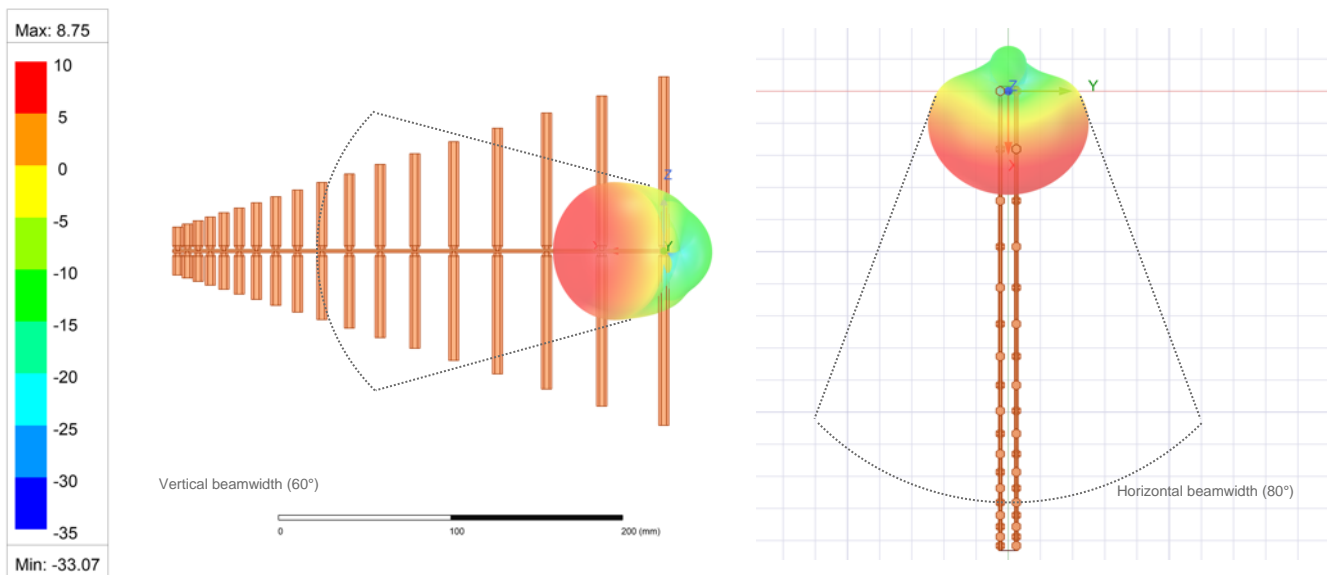


Figure 13: The approximate transmit coverage areas corresponding to different flight heights

In a similar fashion to UAV photogrammetry, the effective resolution is inversely proportional to flight height. At an example flight height of 40m, the antenna will provide optimal coverage within an ellipse of vertical and horizontal bounds of approximately 64m and 50m with respect to antenna polarisation. It is pertinent to place higher importance on the measurements within the high-gain zone of the antenna. As seen in Figure 14, the angles of highest gain occur within the horizontal and vertical beamwidths. This explains why the coverage patterns are longer in one direction, due to larger vertical beamwidth.

Ultimately, the highest-strength signal hotspots, as measured from the antenna, will occur when the UAV is directly above the mobile phone (and a sample is taken). However, in the case where the UAV does not fly directly above the mobile phone and sample, the signal should still be received at nearby samples, albeit with lower effective signal strength.



dB

Figure 14: Radiation pattern of directional cellular antenna from side and top views respectively

5. Ground Station Implementation

5.1 Overview

The ground station consists of various components:

- Workstation computer
- Antenna steering mechanism
- Networking equipment
- UAV battery charging system

Due to the sensitive nature of the eNB - EPC link, a high-bandwidth, low-latency connection is required (Moradi 2018). However, this link needs to be optimised for speed and latency if the eNB and EPC are to be run on separate processors. Signalling between EPC and eNB is very time sensitive (Moradi, Sundaresan et al. 2018). As mentioned by Moradi (2018), the wireless medium is inherently unreliable for such a critical link. Hence most cellular implementations employ a high-bandwidth *wired* link between the EPC and RAN (Sundaresan, Chai et al. 2018).

In the context of the proposed implementation, a directional wireless link is required to satisfy the speed and latency constraints.

5.2 Computer and Network Setup

The workstation computer needs to be quite powerful, as it plays a key role in the operation and post-processing phases of the system. The workstation computer has the following functions:

- Run Network Time Protocol (NTP) server, such that other computers can synchronise to a central clock
- Run the Evolved Packet Core (EPC)
- Parse log files after landing
- Orthomosaic processing
- Geo-referencing of signal hotspots

The computationally expensive nature of these tasks requires a high-performance Central Processing Unit (CPU), and a large amount of Random Access Memory (RAM). The workstation is equipped with an 8-core, 16-thread processor, which is paired to 32GB of Double Data Rate version 4 (DDR4) RAM. The workstation runs Ubuntu Desktop 20.04.3 Long Term Support (LTS) as the operating system.

The workstation computer is connected via ethernet cable to a gigabit switch. Two other ports of this switch are occupied by the ground station components. One other port is connected to the Raspberry Pi 3A which controls the two servos of the pan/tilt mechanism, and the other port is connected to a MikroTik Metal Wi-Fi access point. All the networked components in the system are given static IP addresses in the range 192.168.0.0/24, as seen in Figure 15. The power to the Access Point (AP) is provided through a 24V Power

over Ethernet (PoE) injector. The Local Area Network (LAN) cable connecting to the PoE injector is connected to the gigabit switch.

The MikroTik AP is capable of 31dBm transmit power at 2.4GHz. The AP has a minimum receiver sensitivity of -93dBm. The 19dBi 2.4GHz grid-pack antenna increases both the receive and transmit gain of the AP. The transmit power of the AP is set to 17dBm to fit within the legal Equivalent Isotropic Radiated Power (EIRP) limit of 36dBm at 2.4GHz:

$$EIRP = 17 + 19 = 34 \text{ (assuming no cable loss).}$$

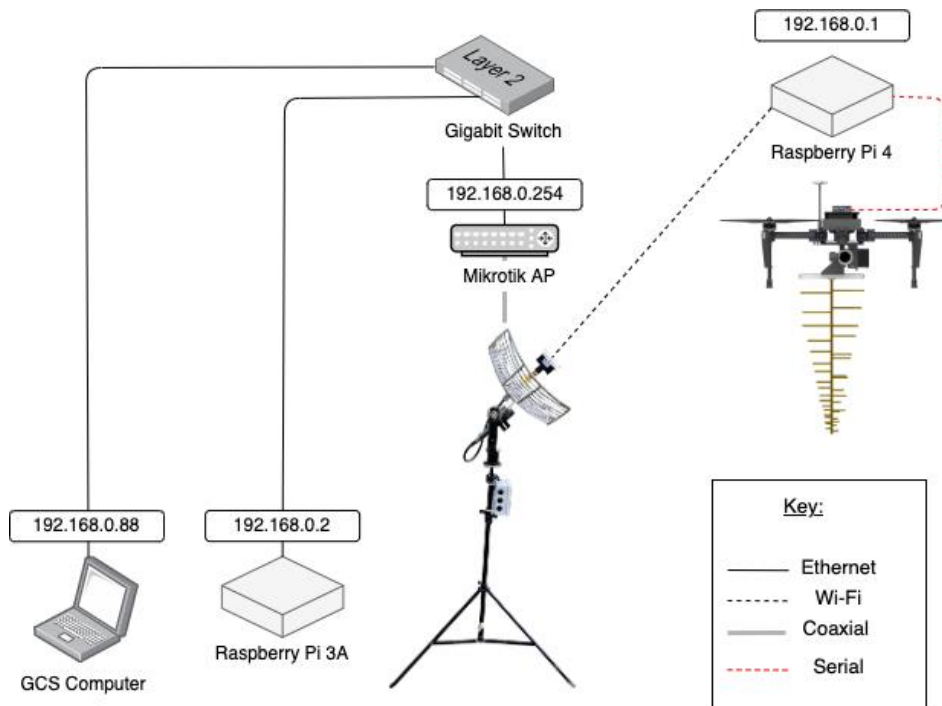


Figure 15: The network and data architecture of the ground control station

5.3 Antenna Steering Mechanism

5.3.1 Specifications

The antenna steering mechanism is based on a panning and tilting mechanism. This mechanism is paired to two Hi-Tec HS785HB servos, one for panning, and one for tilting. This mechanism provides a 7:1 gearing ratio on both axes. The mechanism can move at a maximum speed of 37 degrees/second. This allows a full rotation on both axis in just over 10 seconds, as seen in Table 9.

Table 9: Specifications of the pan/tilt mechanism fitted with Hi-Tec HS785HB servos

Specification	Value
Voltage Range	4-6V (DC)
Stall torque (6V)	13.2 kg.cm

Specification	Value
Travel per μS	$0.224^\circ/\mu\text{sec}$
PWM Range	600-2400 μsec
Maximum Speed	10.5 sec/360° (each axis)

The pan/tilt mechanism is mounted onto a tripod such that the rotating platform is approximately 1.5m above ground level. The two servos require 4-6VDC input, as well as a PWM signal. The mechanism is supplied 5VDC, and the PWM signals are provided by a Raspberry Pi 3A. A 19dBi 2.4GHz grid-pack antenna is mounted to the platform, which is connected to a MikroTik Metal access point via an N-type connector. The AP is also mounted to the platform such that the coaxial cable connecting the antenna to the AP is subject to minimal strain during movement. These details can be seen in Figure 16.

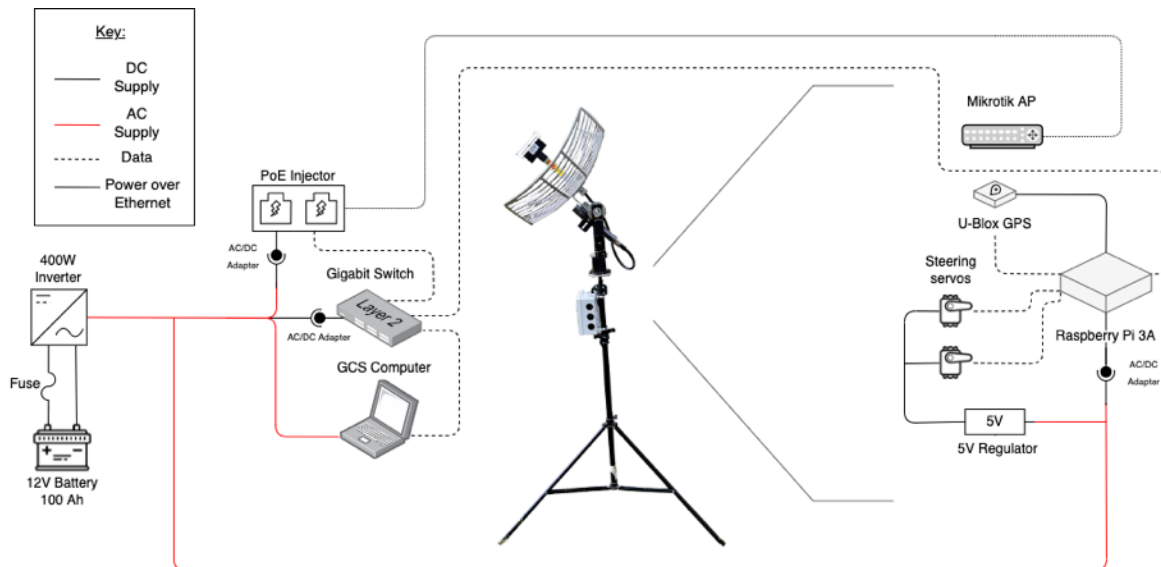


Figure 16: The power and control architecture of the ground control station

5.3.2 Antenna Steering Calculations

To move the pan and tilt mechanism according to the position of the UAV, the following details need to be known:

- The latitude and longitude of the UAV
- The relative height of the UAV
- The latitude and longitude of the ground station
- The height of the ground station antenna (above ground level)

The Raspberry Pi 3A controlling the pan/tilt mechanism informs its control signals based on the following two ROS topics: *gps_position*, and *height_above_takeoff*. The Raspberry Pi 3A subscribes to these two topics over LAN.

The Raspberry Pi 3A is also connected to a USB GPS (u-Blox M8P). This allows the Pi to know the location of the GCS in the world. The output of this GPS is converted from National Marine Electronics Association (NMEA) format into latitude and longitude. All locations are based on the World Geodetic System 1984 (WGS84) coordinate reference system. Therefore, when the Pi subscribes to the *gps_position*, and *height_above_takeoff* topics from the UAV, it knows the location of the ground station, the location of the UAV, and the height of the UAV. This allows the Pi to dynamically calculate the azimuth and elevation angles to point the grid-pack antenna at the UAV, as seen in Figure 17.

Of course, there is a delay between the UAV resolving its own GPS position, sending this over ROS topic to the ground station, and then the ground station subsequently moving the antenna. This might be a greater issue in a high frequency system due to the shorter wavelength, however the relatively low frequency of 2.4GHz Wi-Fi is more forgiving. Especially considering the inherently wide horizontal beam-widths of sub-6GHz directional antennae (Sundaresan, Chai et al. 2018). The grid-pack antenna has horizontal and vertical beamwidths of 12° and 16° respectively, allowing for some leniency in tracking delay. The high gain and relatively forgiving beamwidth angles were the reason a grid-pack antenna was chosen over other antenna types.

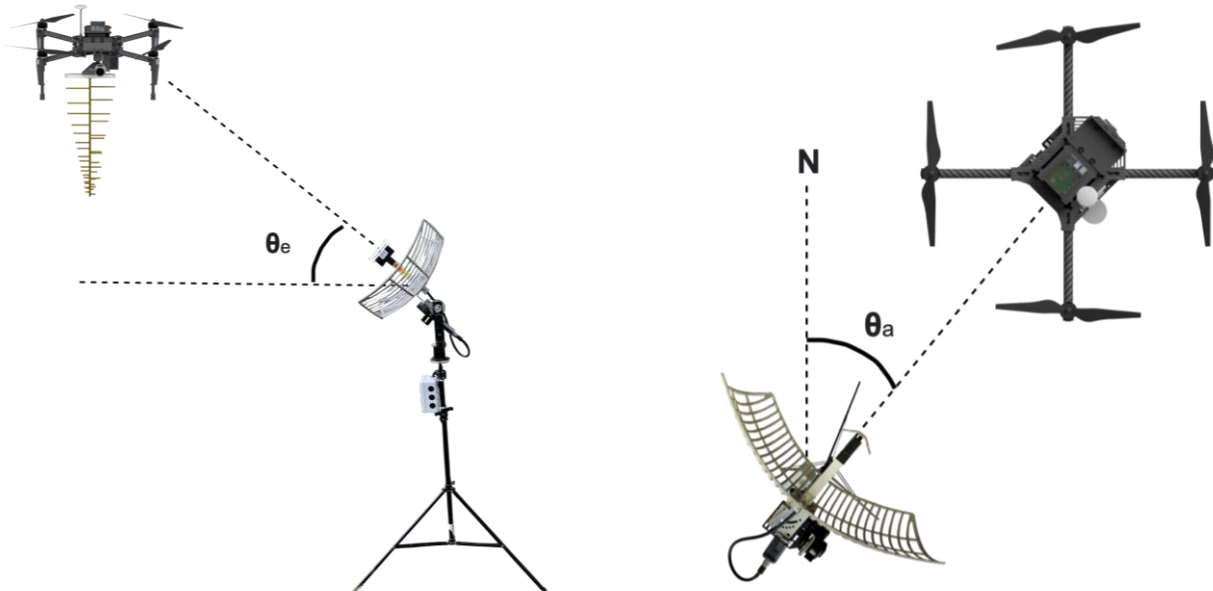


Figure 17: Diagrams representing elevation and azimuth angles respectively

The mathematical workflow to calculate the bearing/azimuth between two points (latitude and longitude) is as follows:

- Let λ be latitude
- Let ϕ be longitude
- Let θ_a be bearing. Where bearing is measured clockwise from North

The bearing between two points, λ_A, ϕ_A and λ_B, ϕ_B can be calculated:

$$X = \cos(\theta_B) \times \sin(\Delta L)$$

$$Y = \cos(\theta_A) \times \sin(\theta_B) - \sin(\theta_a) \times \cos(\theta_B) \times \cos(\Delta L)$$

Therefore, $\theta_a = \arctan2(X, Y) \times \frac{180}{\pi}$ degrees

The mathematical workflow to calculate the elevation angle between two points is as follows:

- Let $R = 6,371\text{km}$ be the radius of the earth
- Let Δd be the horizontal distance between the two points
- Let h be the relative height of the highest point

The formula to calculate the distance between two points (latitude, longitude) is based on the Haversine formula (Robusto 1957). The Haversine formula calculates the great circle distance between two points:

$$a = \sin^2\left(\frac{\Delta\lambda}{2}\right) + \cos(\lambda_A) \times \cos(\lambda_B) \times \sin^2\left(\frac{\Delta\phi}{2}\right)$$

$$c = 2 \times \arctan2(\sqrt{a}, \sqrt{1 - a})$$

$$\Delta d = R \times c$$

The elevation angle (θ_e), can be represented using a right-angle triangle, as seen in Figure 18.

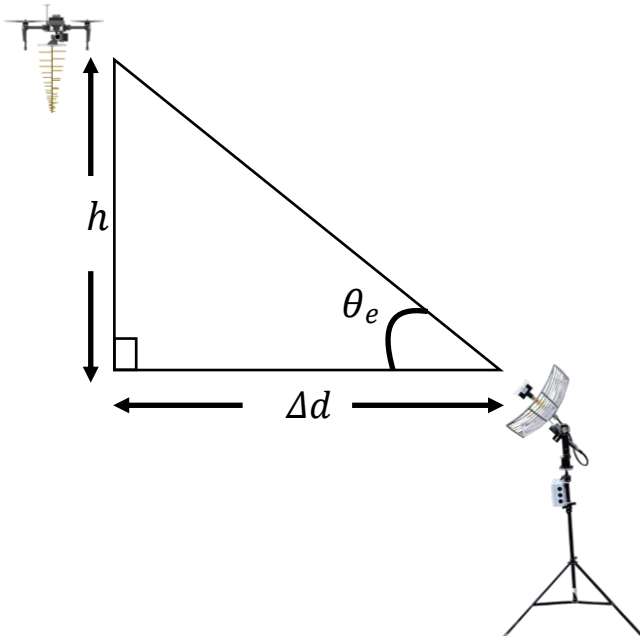


Figure 18: Triangle representing mathematical relationship between GCS and UAV

The elevation angle (θ_e) is given by: $\theta_e = \arctan\left(\frac{h}{\Delta d}\right)$

Therefore, the bearing angle (θ_a) and elevation angle (θ_e) are known. These values are then converted to a PWM pulse width and used to control the pan and tilt servos.

5.3.3 Antenna Steering Limitations

An additional consideration is the tracking speed of the antenna steering mechanism. As seen in Table 9, the speed of the pan/tilt mechanism is 10.5sec/360° on both the pan and tilt axes. The absolute maximum speed of the M100 UAV is 22m/s. It is unlikely that the M100 would reach these speeds in normal flying conditions, nor in a predefined path plan. However, to find the worst-case distance between the GCS and UAV, the angular velocity and speed of the pan/tilt mechanism is calculated with this maximum UAV speed:

$$\omega = \frac{v}{r} = \frac{2\pi}{T} = \frac{2\pi}{10.5} = 0.598 \text{ rad/s}$$

$$0.598 = \frac{22}{r}, \text{ therefore } r = \frac{22}{0.598} = 36.76\text{m}$$

Therefore, the worst-case minimum distance (to retain a tracking link) between the UAV and the GCS is 36.76m, as seen in Figure 19.

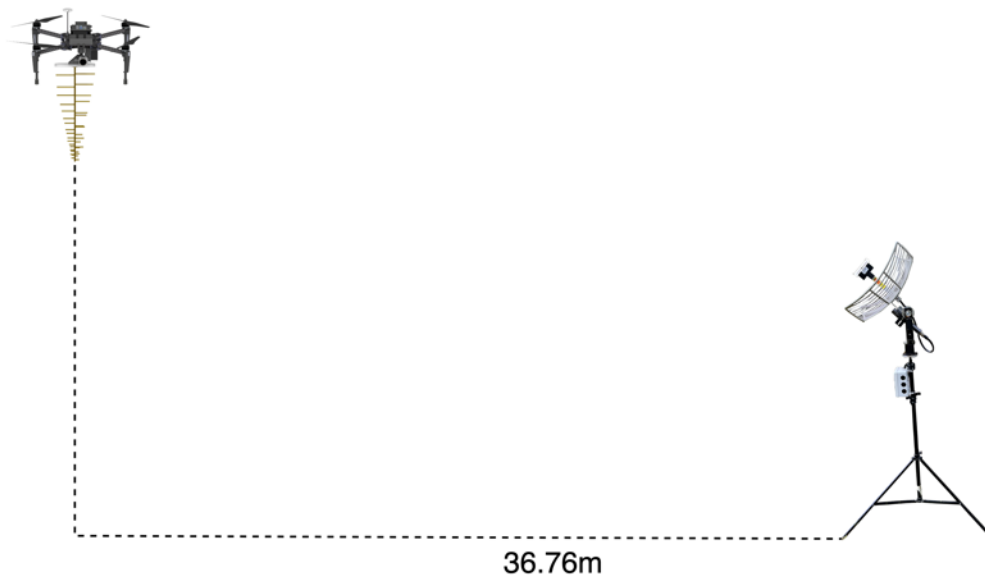


Figure 19: Minimum distance between the GCS and full-speed UAV to maintain tracking

Another limitation of this mechanism is the maximum tilt angle of the antenna. Due to the mechanical design of the system, the antenna can reach a maximum tilt angle of 80° (from horizontal). However, if the UAV flight height is limited below 208m, and the GCS is located at the worst-case minimum distance (see Figure 19), this limitation will not be reached.

Other Equipment and Considerations

5.3.4 Wi-Fi Link Range

Another consideration is the effective range of the wireless 2.4GHz link. The 19dBi 2.4GHz grid-pack antenna on the GCS steering mechanism points at the 4dBi omnidirectional 2.4GHz whip antenna (part of the Wi-Fi dongle) on the UAV. Therefore, the maximum theoretical distance of this link can be calculated if it is modelled as a point-to-point link in free space. While the link is full duplex (i.e., both radios act as transceivers), the bottleneck of the link range is the antenna gain and receiver sensitivity of the UAV Wi-Fi dongle. Therefore, the UAV Wi-Fi dongle will be modelled as the receiver (R), and the GCS grid-pack antenna as the transmitter (T) to realistically depict the worst-case range.

To maintain sufficient speed for the EPC-RAN link, a minimum link speed of 50Mbps is assumed, which is a minimum requirement according to Coldrey, Berg et al. (2013). A link margin of 15dB is assumed to account for other losses.

The calculation parameters are as follows:

- P_T is the transmitter power of the GCS AP (dBm): $P_T = 17\text{dBm}$
- G_T is the antenna gain of the GCS AP: $G_T = 19\text{dBi}$
- G_R is the antenna gain of the UAV Wi-Fi dongle: $G_R = 4\text{dBi}$
- L_{margin} is the link margin: $L_{margin} = 15\text{dB}$
- c is the speed of light: $c \approx 3 \times 10^8 \text{ m/s}$
- d is the relative distance between GCS and UAV Wi-Fi antennae
- f is the frequency of the signal: $f = 2.4 \text{ GHz}$

The minimum receiver sensitivity of the UAV Wi-Fi dongle for different link speeds at 2.4GHz (802.11n) is:

- 54Mbps: -68dBm
- 11Mbps: -85dBm

Therefore, to sustain a minimum link speed of 50Mbps, the minimum receiver sensitivity is -68dBm. The maximum distance considering the UAV Wi-Fi dongle as the receiver and GCS antenna as the transmitter can be calculated:

$$P_T + G_T + G_R - L_{margin} - P_{loss} \geq -68$$

$$17 + 19 + 4 - 15 - P_{loss} \geq -68$$

$$\text{Therefore } P_{loss} \leq 93\text{dB}$$

$$FSPL = 20\log_{10}(d) + 20\log_{10}(f) + 20\log_{10}\left(\frac{4\pi}{c}\right)$$

$$20\log_{10}(d) + 20\log_{10}(2.4 \times 10^9) + 20\log_{10}\left(\frac{4\pi}{3 \times 10^8}\right) \leq 93$$

$$d \leq 10^{\frac{93 - 20 \log(2.4 \times 10^9) - 20 \log(\frac{4\pi}{3 \times 10^8})}{20}}, \text{ therefore } d \leq 444.3\text{m}$$

The maximum link distance between GCS and UAV, while maintaining a 15dB link margin and maintaining a >50Mbps link, is approximately 444m in free space LoS conditions. In reality, this distance will be lower due to unaccountable propagation losses. It is safe to assume that the UAV and GCS will be in line of sight of each other within a typical operating scenario. It is also worth noting that the theoretical link range would be significantly larger (approximately 1.2km) if the maximum transmit power of the MikroTik AP was selected.

5.3.5 Charging and Power Considerations

Of course, more equipment is required to make the system fully operational. To maintain the operation of the UAV, multiple batteries will be required. Additionally, a battery charging station would be required to replenish used batteries. The charging system used is a Smart PowerCharge SPCM100. This charging system charges four TB47D/TB48D batteries simultaneously, as well as two remote controllers, and two USB devices. This allows for near continuous operation of the UAV, only requiring landing to swap in a charged battery.

Whilst the computer in this setup is a desktop computer, a well-equipped laptop computer (e.g., six-core processor or greater, with 16GB RAM) would likely be sufficient in terms of computation performance. The total power draw of the GCS does not exceed 400W. Therefore, a 100Ah 12V lead-acid battery can be paired with a 400W inverter to provide power to the GCS in remote scenarios. Assuming no conversion losses from the inverter, and assuming a 50% depth of discharge, the battery would be able to provide 400W of power for a period of approximately 1.5 hours.

For field tests and real-world applications, many of the ground station components can be relocated within a vehicle, such that the vehicle can provide power for the GCS.

6. Cellular and Radio Implementation

6.1 Cellular Stack

6.1.1 Segregated Architecture

4G/LTE is widely regarded as the most prevalent cellular implementation at the time of writing. The 4G/LTE implementation consists of two main components:

- EPC: Evolved Packet Core
- RAN: Radio access network, commonly referred to as the 'eNB'

In most implementations, the radio access network is connected via a high-capacity wired link to the EPC. This connection is critical, because the EPC performs most of the packet routing and 'heavy-lifting' in the network. The EPC is also the interface between the cellular network and the internet. In some cases, the EPC is connected to the eNB via a high bandwidth microwave link. In the system depicted in this thesis, the EPC is separated from the RAN via a 2.4GHz Wi-Fi link. The RAN controls the relay of uplink and downlink information to and from the UE via radio connections.

The EPC is run on a ground station computer, and the RAN is run on the UAV's onboard computer (Raspberry Pi 4). The RAN is purely focused on handling the communication between eNB and UE (mobile phones in this context).

While srsRAN has a standard architecture, as seen in Figure 20, the architecture deployed in the proposed system is different, as shown in Figure 21. The main difference being the eNB and EPC hosted on different computers. Additionally, the customised architecture does not have a connection between the EPC and the internet. This customised architecture is conducive to the constraints of the UAV platform and the available computing power. The constraints of the UAV platform preclude the fitment of a high-performance computer.

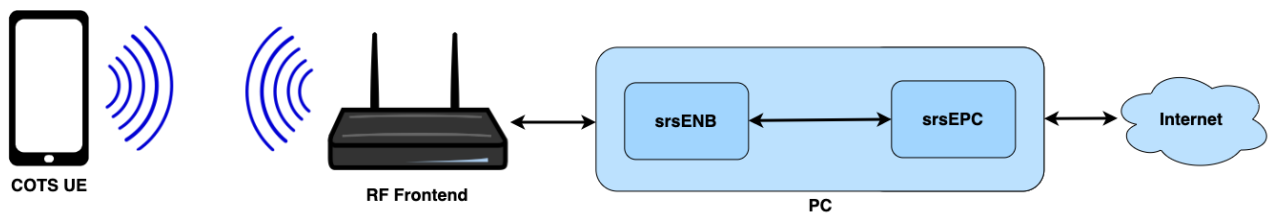


Figure 20: Standard srsRAN architecture

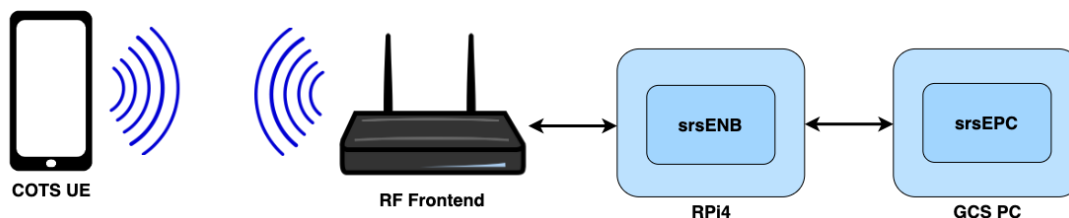


Figure 21: Customised srsRAN architecture

As seen in Figure 21, the customised srsRAN architecture does not have a connection to the internet. The operating principle of the system is such that an internet connection is not required. Additionally, due to the limited processing capability of the onboard computer, more traffic from outside the network could impede the performance of the system. It is worth noting that in realistic deployment of such a system, there would be another connection between the EPC and some form of network operations centre. This could also include some connection to the internet on the infrastructure side.

6.1.2 Cellular Radio Frontend

The RF frontend is the Nuand BladeRF xA4 SDR. This SDR is well supported by the srsRAN stack. The BladeRF is a very flexible software-defined radio. In terms of architecture, the BladeRF xA4 contains the following major components:

- Analog Devices AD9361 transceiver: This Integrated Circuit (IC) interfaces with the FPGA, and connects to the four SMA ports on the BladeRF xA4
- Intel Cyclone V E FPGA: The FPGA is loaded with a Hardware Description Language (HDL) image. The FPGA is the processing unit which controls the AD9361, and controls the data flow between the USB controller and the AD9361 IC
- Cypress FX3 USB controller: This controller handles the data between the BladeRF xA4 and a connected computer

The hardware architecture of the BladeRF xA4 is shown in Figure 22.

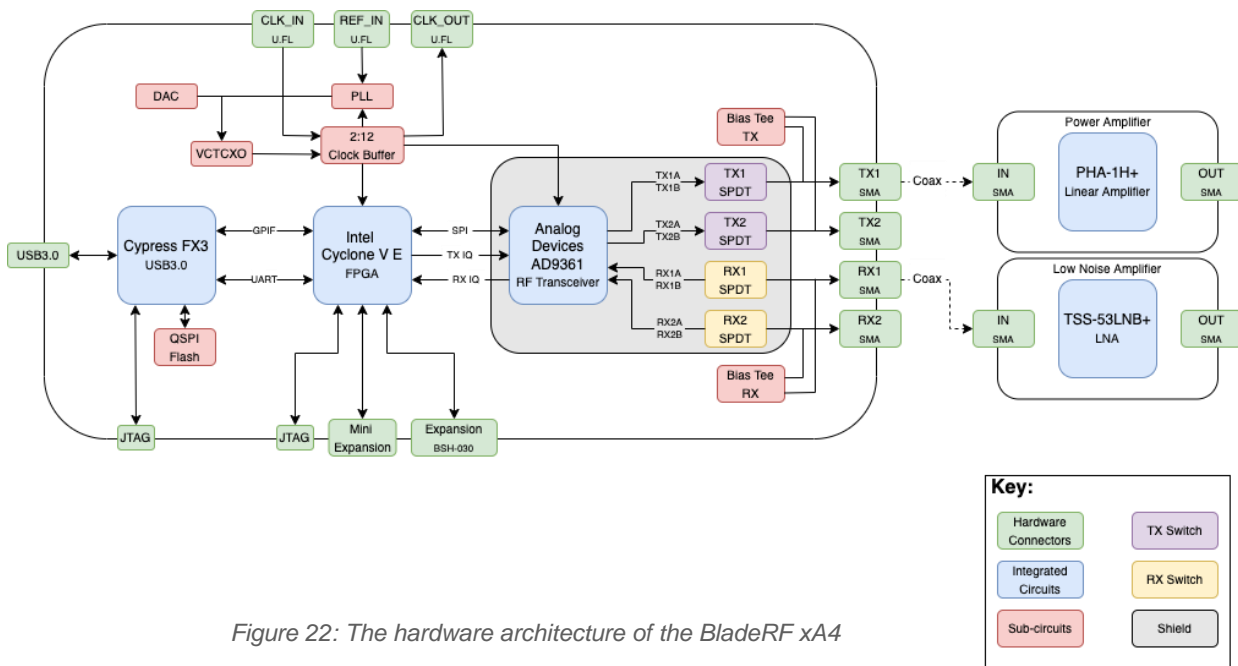


Figure 22: The hardware architecture of the BladeRF xA4

The BladeRF xA4 can be tuned to any LTE Frequency Division Duplex (FDD) band within the range of 47MHz to 6GHz. The BladeRF xA4 is also capable of Time Division Duplex (TDD) operation, however this mode was not used due to the tight timing requirements imposed on the onboard Raspberry Pi 4. The BladeRF is connected via USB to the onboard Raspberry Pi 4. A customised HDL image is loaded onto the FPGA. This image can be edited to achieve greater versatility in the RF hardware.

The Raspberry Pi 4 runs the eNB software, which interfaces directly with the BladeRF.

The PHA-1H+ Integrated Circuit (IC) within the BT-100 power amplifier is connected to the TX1 port of the BladeRF xA4 and provides approximately 8dB of transmit gain at 1800MHz. The TSS-53LNB+ IC within the BT-200 low noise amplifier is connected to the RX1 port of the BladeRF xA4 and provides approximately 22dB of receive gain at 1800MHz and only 1.5dB of noise figure at 1800MHz.

A 3dBi omnidirectional antenna is connected to the LNA. The 9dBi nadir directional antenna is connected to the PA. A directional antenna was chosen for the transmitter antenna due to the qualitative goal of *directionally* transmitting the downlink cellular signals to the UE. An omnidirectional antenna was chosen for the receiver antenna because this would allow for a much larger uplink coverage area, instead of the relatively selective area of a directional nadir antenna, if that were to be used instead. The metric used for location inference is based on the UE's measurement of the downlink reference signals (see subsection 6.3.2).

6.2 Cellular Network Setup

6.2.1 SIM cards and COTS UE

For testing, a COTS mobile phone was used. As this gives the most realistic representation of real-world performance. To enable the COTS UE to connect to the custom cell, bespoke Subscriber Identity Module (SIM) cards were required. These SIM cards must have the following features:

- Unlocked IMSI
- Unlocked Operator Code (OPC)
- Unlocked key (KI)

The acquired SIM cards all came with a Mobile Country Code – Mobile Network Code (MCC-MNC) of 901-70, which does not conflict with any other MCC-MNC combination. The Sysmocom SIM cards were installed into an iPhone 6s (model A1688), which was used as the target UE during testing.

6.2.2 Cellular Channel Setup

The cellular implementation, srsRAN, required certain settings to be configured. This subsection discusses the radio settings that were decided upon for this system. The capabilities of srsRAN are extensive, supporting FDD bandwidths of 1.4, 3, 5, 10, 15 and 20MHz (corresponding to Physical Resource Block (PRB) values of 6, 15, 25, 50, 75 and 100). The BladeRF SDR can support transmission mode 2 with the two receive and transmit ports, however transmission mode 1 was used for this system due to limited payload capability, and reduced complexity.

The primary downlink LTE Universal Terrestrial Radio Access (UTRA) Absolute Radio Frequency Channel Number (UARFCN) used for testing was 1937 (LTE band 3). This corresponds to an uplink frequency (UE to eNB) of 1783.7MHz, and a downlink frequency (eNB to UE) of 1878.7MHz. Channel 1937 was chosen for regulatory reasons. Additionally, the directional cellular antenna appears to have the best performance within

this band (see Appendix A). This channel was configured to a bandwidth of 1.4MHz with the number of LTE PRBs set to 6. A PRB of 6 is the lowest possible number of physical resource blocks configurable in srsRAN. This reduces the effective throughput on the channel; however, it reduces the computational load on the onboard Raspberry Pi, which is necessary. The configuration was trialled with a PRB of 15. With this configuration, the eNB was exceeding transmission time intervals. This is a characteristic of CPU overload.

6.2.3 Parameter Configuration

The LTE software suite used is srsRAN, which consists of three major components:

- srsENB: Deployed upon onboard computer
- srsEPC: Deployed upon ground station computer
- srsUE: Unused in this system, because a COTS mobile phone is the target UE

These various components of srsRAN are built in Linux environments.

srsRAN is configurable via different scripts, which can then be called to initiate each component respectively. Table 10 shows the configuration files.

Table 10: The configuration scripts used in srsRAN

Configuration Script	Explanation
epc.conf	Configures the Evolved Packet Core
enb.conf	Configures the Evolved Node B
rr.conf	Configures the radio resources for the eNB
sib.conf	Configures the system information block for the eNB

Table 11 shows an abridged subset of the various software parameters that have been configured for this system. The remaining parameters can be seen in Appendix B.

Table 11: The configurable parameters in srsRAN

Parameter	Explanation	Set as	Justification	Configured in
Downlink UTRA Absolute Radio Frequency Channel Number	Unique channel number which corresponds to the downlink radio frequency used by srsENB	1937	UARFCN of 1937 corresponds to 1878.7MHz downlink frequency, and 1783.7MHz uplink frequency. This is in LTE band 3	enb.conf
LTE Transmission Mode	The transmission mode denotes the antenna configuration for Physical	TM1	TM1 denotes single transmission antenna and single receiver antenna	enb.conf

Parameter	Explanation	Set as	Justification	Configured in
	Downlink Shared Channel (PDSCH)			
Transmit gain	Transmit gain	75dB	Realistic gain saturates at approximately 75dB. See subsection 8.1.2 for justification	enb.conf
Receive gain	Receive gain	35dB	LNA provides sufficient gain (22dB) without much need for digital gain	enb.conf
Number of physical resource blocks	Number of physical resource blocks to offer on the cellular channel. This also determines the bandwidth of LTE channel	6	PRB of 6 is the least computationally intensive PRB option. PRB of 6 corresponds to 1.4MHz bandwidth	enb.conf
Minimum receiver sensitivity	The minimum required receiver power within the cell	-115dBm	Decreasing receiver sensitivity allows for eNB to UE connections to be maintained in worsening signal conditions	rr.conf
P_max	Maximum transmit power from the UE. Controlled by the eNB.	3	Category 3 limits maximum UE transmit power of 23dBm (Haider and Hwang 2019)	rr.conf

The srsRAN parameters were configured such that the computational load on the Raspberry Pi 4 was not prohibitive, whilst also maintaining functionality as a ‘bare bones’ LTE RAN.

6.3 Flight Considerations

6.3.1 RF Propagation Characteristics in Environment

Specific attention needs to be paid towards the environment that the system will be used in. There are two primary types of search and rescue; Urban Search and Rescue (USAR) and Wilderness Search and Rescue (WiSAR). As the name suggests, USAR pertains to search and rescue in urban environments, events such as earthquakes, tsunamis and so forth. WiSAR is more of an umbrella term and pertains to more rural environments. These two practices are fundamentally different in their methods of procedure. However, particular attention must be paid to the radio propagation differences in these two different scenarios. Radio communication through large buildings has been a challenge for many

SAR personnel due to the signal propagation characteristics of different building materials (Wong and Robinson 2004, Holloway, Young et al. 2008). The attenuation of signals is largely dependent on the type of building, its materials and the respective locations of the transmitters and receivers. A series of studies were undertaken to analyse RF propagation characteristics prior to and following the collapse of public buildings (Holloway 2005, Holloway, Koepke et al. 2005, Holloway 2006, Holloway, Young et al. 2008, Holloway, Koepke et al. 2014). These studies noted the following observations: with a receiver based outside the buildings, and a transmitter inside, there is generally a 10-30dB attenuation of signals prior to collapse. Yet, after the collapse, this attenuation can be between 20dB and 70dB, or even higher (Holloway, Koepke et al. 2005, Holloway, Koepke et al. 2005). This highlights the difficulty of radio transmissions after the collapse of large buildings. In some cases, propagation was better for different test frequencies after the collapse, due to the coupling of signals onto metal debris (Holloway, Young et al. 2008).

For the purposes of testing this system, environments that were more akin to WiSAR environments were chosen (as opposed to USAR environments). This was due to the scope of the project.

The radio frontend of the BladeRF does not feature discrete filtering hardware (e.g., cavity filters). Filtering is instead implemented digitally, which is inherently worse performing than discrete filtering componentry.

6.3.2 Location Inference Parameters

The eNB has many different parameters that can be extracted to infer the position of the UE. The obvious parameters that come to mind are signal strength-based metrics, such as RSRP, RSRQ, SNR, EPRE and so forth. This is because it seems intuitive that signal strength-based metrics will vary significantly based on the distance between the UE and eNB. However, there are a number of limitations to using these parameters. For example, RSRP and RSRQ are only measured by the UE when an LTE A3 event is triggered (Mehta, Akhtar et al. 2015). This occurs when the UE detects a neighboring cell with greater power. Additionally, RSRP measurements are based on a linear average of the reference signal resource element measurements. RSRP exclusively measures the reference signal power and does not take noise and interference power into account. The relationship between RSRP and EPRE can be distilled to the following equation, as adapted from (Sevindik, Wang et al. 2012):

$$RSRP = EPRE - P_{PL} - P_{LTF} - P_{STF}$$

Where:

- P_{PL} is path loss
- P_{LTF} is long term fading
- P_{STF} is short term fading

EPRE can be thought of as power per 15kHz, or power per Orthogonal Frequency-Division Multiplexing (OFDM) symbol.

EPRE is measured constantly by the UE and then relayed to the eNB in uplink control channels. SNR is another good metric, however signal to noise ratio measures the ratio of

signal power to noise power. Noise power is not necessarily affected by distance between a UE and eNB. It is more affected by obstructed propagation paths (Chen, Loschonsky et al. 2012) and RF noise sources.

There are a number of other metrics that can be extracted from the eNB log file:

- **CQI: Channel Quality Indicator:** As the name suggests, CQI is a measure of the quality of the channel as measured by the UE. However, CQI is based on downlink SNR (Kawser, Hamid et al. 2012). CQI informs the transport block size, which is directly proportional to throughput. CQI is also directly correlated with MCS.
- **MCS: Modulation Control Scheme:** MCS is derived from CQI, which changes the modulation scheme (e.g., Quadrature Phase Shift Keying (QPSK)). Changes in MCS are communicated across the Physical Uplink Shared Channel (PUSCH), which carries Radio Resource Control (RRC) signaling messages (Perez 2015). Yet, MCS is based on downlink SNR (Kawser, Hamid et al. 2012).
- **CFO: Carrier Frequency Offset:** A compensation by the oscillators on the radio frontend to compensate for doppler shift (Vijay, Sasibhushana Rao et al. 2019). This is applicable where the UE is moving at high speed with respect to the eNB. This also requires characterisation of the frequency components on the radio frontend, which could vary with temperature, or other environmental effects.
- **TA: Timing Advance:** Ensures maintenance of scheduling requirements between UE and eNB. The eNB sends timing advance requests to the UE to accelerate or delay its transmissions (Jarvis, McEachen et al. 2011). Timing Advance has been investigated for distance estimation between UE and eNB (Jarvis, McEachen et al. 2011). The TA metric is heavily dependent on the timing margins of the radio frontend, which is inherently inaccurate for the SDR-based frontend depicted in this system. This is due to processing delays from the onboard computer, and manual calibration of timing advance.
- **DMRS: Demodulation Reference Signal:** This is the reference signal sent by the UE to the eNB for demodulation purposes. DMRS gives a good estimation of uplink channel characteristics. This can be subsequently used in post-processing and location inference. However, this process requires very good characterisation of the radio frontend of the SDR and any other frequency-distorting elements. Additionally, DMRS is measured by the eNB, which would mean switching the directional antenna to the RX port of the SDR.

EPRE (as measured by the UE) appears to be the parameter that satisfies the limitations and characteristics of the SDR radio frontend of the eNB. This is because the value of EPRE is not affected by bandwidth or the number of PRB's. This is important because both bandwidth and the number of PRB's is likely to be higher in a realistic deployment of such a system (with a more capable onboard computer). EPRE is also independent of the LTE resource element type (i.e., reference signal or PDSCH) (ShareTechnote 2014). EPRE is the most granular power measurement available in a typical LTE deployment, as it is based on the smallest data unit (one resource element). EPRE values logged by the eNB are measured with units dBFS. This unit pertains to decibels relative to full scale and does not pertain to an absolute power measurement (i.e., dBm).

6.3.3 Cellular Link Range

To find the effective range of the system, the following information is needed:

- The transmit power of the SDR
- The maximum transmit power of the UE
- The minimum receiver sensitivity of the SDR
- The minimum receiver sensitivity of the UE
- The gains (or losses) of any additional components (i.e., PA, antenna)

The Nuand BladeRF xA4 has a maximum Continuous Wave (CW) power of 8dBm. However, the channel power with a 1.4MHz LTE bandwidth is approximately -18dBm (see subsection 8.1.2). This calculation will assume that the BT-100 Power Amplifier will be in line between the TX port of the BladeRF and the antenna. This PA has a gain of approximately 8dB at this frequency and bandwidth. This calculation also assumes that the 9dBi directional antenna is attached to the PA. A free space path loss model is also assumed for this calculation. This is a theoretical assumption, and is not entirely applicable to post-disaster, inhomogeneous propagation environments. However, it is useful to gain an understanding of the theoretical limits of the system.

3GPP specify an uplink power limit of 23dBm (Haider and Hwang 2019). A power of 23dBm is still higher than the maximum transmit power of the transmitter chain from the SDR. The EIRP of the transmitted signal originating from the SDR will be approximately 9dBm. A $Q_{rxlevmin}$ value of -115dBm will also be assumed, which is a typical value for $Q_{rxlevmin}$ (Garavaglia, Brunner et al. 2005). $Q_{rxlevmin}$ essentially refers to the minimum 'useable' cellular receiver sensitivity. For the purposes of these calculations, it will be assumed that the UE has 0dB of gain on its cellular antennae. A link margin of 15dB will also be assumed. Although LTE is full duplex, it will be assumed that the transmitter is the SDR, and the receiver is the A1688 to depict a worst-case range.

Where:

- P_T is the transmitter power of the BladeRF (including PA): $P_T = -10\text{dBm}$
- G_T is the antenna gain of the directional cellular antenna: $G_T = 9\text{dBi}$
- G_R is the antenna gain of the A1688 iPhone antenna: $G_R = 0\text{dBi}$
- L_{margin} is the link margin: $L_{margin} = 15\text{dB}$
- c is the speed of light: $c \approx 3 \times 10^8 \text{ m/s}$
- d is the relative distance between SDR and UE antennae
- f is the frequency of the signal: $f = 1.8 \text{ GHz}$

Therefore, the maximum distance to maintain the link can be calculated:

$$P_T + G_T + G_R - L_{margin} - P_{loss} \geq -115$$

$$-10 + 9 + 0 - 15 - P_{loss} \geq -115$$

$$\text{Therefore } P_{loss} \leq 99\text{dB}$$

$$FSPL = 20\log_{10}(d) + 20\log_{10}(f) + 20\log_{10}\left(\frac{4\pi}{c}\right)$$

$$20\log_{10}(d) + 20\log_{10}(1.8 \times 10^9) + 20\log_{10}\left(\frac{4\pi}{3 \times 10^8}\right) \leq 99$$

$$d \leq 10^{\frac{99 - 20\log_{10}(1.8 \times 10^9) - 20\log_{10}\left(\frac{4\pi}{3 \times 10^8}\right)}{20}}, \text{ therefore } d \leq 1,182.1\text{m}$$

Therefore, the maximum link distance between the UE and the SDR RAN is approximately 1,182m with the aforementioned information and assumptions. Realistically, this range will be lower due to the non-ideal propagation environments. Due to the nadir orientation of the directional antenna attached to the SDR RAN, this maximum link distance pertains to the maximum height that the UAV could be above the location of the UE in order to retain the link. This is because this calculation assumes the directional cellular antenna is pointing directly at the UE.

7. Software Implementation

7.1 System Architecture

This section is distinctly separate from firmware. This section is intended to articulate the higher-level unification of the separate subsystems through software. The software system architecture can be broken into three distinct subsystems:

- UAV vehicle (DJI Matrice 100)
- Hardware additions (payload)
- Ground control station

All the computers within the system are linked via Transmission Control Protocol/Internet Protocol (TCP/IP). The intermediary components are interfaced via many different protocols, as shown in Figure 23.

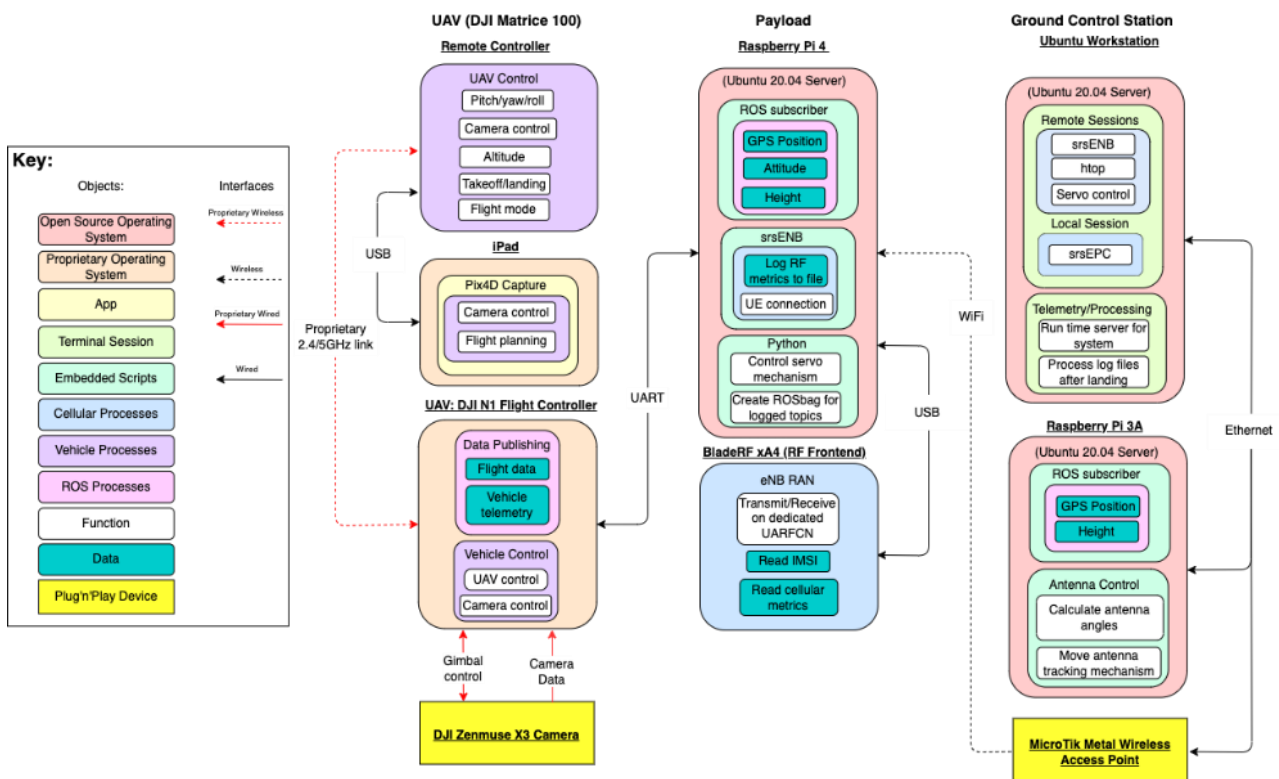


Figure 23: The software architecture of the system

The high-level interfacing protocol in this system is TCP/IP and is implemented over a variety of media. For the RAN to EPC connection, the packet type used is Stream Control Transmission Protocol (SCTP), which is similar to User Datagram Protocol (UDP) yet supports multi-streaming, therefore ensuring delivery of data if one stream is blocked (Hasan 2019). UDP is the primary packet type in the rest of the network and is used by other subsystems such as ROS and NTP. The lower-level interfaces are implemented over a variety of different protocols including UART, USB and other proprietary interfaces. Due to their nature as hardware-deployed protocols, these lower-level interfaces have inherently tighter timing requirements than TCP/IP.

7.2 ROS Setup

7.2.1 ROS Topics

A ROS topic is essentially a data bus for a stream of messages from a specific sensor or subsystem. There are 25 different ROS topics that can be subscribed to or published in this ROS environment. Publishable topics can be written to, allowing control over the UAV, whereas subscription topics can only be read from the UAV flight computer. This system is only concerned with subscription topics. The onboard Raspberry Pi 4 is connected to the M100 through UART running at 38,400 baud (see Table 13). The M100 must initialise ROS and activate the UAV based on a developer key. If the credentials on the M100 match the credentials in the setup script, the connection is activated. This hand-shaking procedure is executed with the following ROS terminal commands:

```
cd ~/catkin_ws
catkin_make
source ~/catkin_ws/devel/setup.bash
roslaunch dji_sdk sdk.launch
```

If the handshaking procedure is successful, the terminal output will display the output as shown in Figure 24.

```

dji_sdk (dji_sdk/dji_sdk_node)
auto-starting new master
process[master]: started with pid [2941]
ROS_MASTER_URI=http://localhost:11311

setting /run_id to 74320704-d6e9-11eb-8bce-dbc56242548e
process[rosout-1]: started with pid [2951]
started core service [/rosout]
process[dji_sdk-2]: started with pid [2958]

STATUS/1 @ init, L55: Attempting to open device /dev/ttyAMA0 with baudrate 230400...
STATUS/1 @ init, L65: ...Serial started successfully.
STATUS/1 @ parseDroneVersionInfo, L727: Device Serial No. = 041D491856
STATUS/1 @ parseDroneVersionInfo, L729: Hardware = M100
STATUS/1 @ parseDroneVersionInfo, L730: Firmware = 3.1.10.0
STATUS/1 @ parseDroneVersionInfo, L733: Version CRC = 0xA6453AAC
STATUS/1 @ initSubscriber, L778: Telemetry subscription mechanism is not supported on this platform!
STATUS/1 @ initMFIO, L981: MFIO is not supported on this platform!
STATUS/1 @ initHardSync, L1077: Hardware Sync is not supported on this platform!
STATUS/1 @ activate, L1313: version 0x3010A00
STATUS/1 @ activate, L1326: Activation successful
[ INFO] [1624758377.232722925]: drone activated
[ INFO] [1624758377.331670047]: Use legacy data broadcast to get telemetry data!
```

Figure 24: Terminal output showing successful hand-shaking procedure

Then, a new Secure Shell (SSH) session can be initiated, and the proper operation of the system can be verified by running the command `rostopic list`. If the system is operating properly, the output as shown in Figure 25 will be displayed. This is the list of available

ROS topics. The `rostopic list` command can also be run on another ROS node within the network e.g., the ground station computer.

To subscribe to a ROS topic, a subscriber function is required. However, the subscriber function needs to understand the message *type* to interpret the content of the ROS messages. Table 12 shows the subscribed topics and important subscription parameters.

Table 12: Subscribed ROS topics and corresponding details

Subscribed Topic	Explanation	ROS Message Type	Calling Script
gps_position	The real-time GPS position of the UAV	sensor_msgs/NavSatFix	gps_subscriber_code.py
height_above_takeoff	The height of the UAV above take-off position	std_msgs/Float32	height_subscriber_code.py
attitude	The real-time pitch, roll and yaw of the UAV	sensor_msgs/Imu	servo_subscriber_code.py

The onboard Raspberry Pi ‘subscribes’ to the three aforementioned topics through a collection of Python scripts. The *attitude* quaternions are converted into angles, from which the pitch, yaw and roll angles of the UAV can be gauged in real-time. The pitch angle is fed into a separate script which controls the onboard antenna compensation servo. This servo is connected to a PWM GPIO on the Raspberry Pi. The *height_above_takeoff* topic is also subscribed to by the onboard Raspberry Pi. The data from this topic is used to set a flag when the UAV is at least 1.5m above ground. This flag is used as an enable signal to allow the antenna to transition from take-off/landing position to nadir position. The onboard Raspberry Pi is configured as the ROS Master, this means that any other ROS nodes within the LAN can subscribe to the ROS topics published by the UAV.

```

ubuntu@ubuntu:~/catkin_ws$ rostopic list
/dji_sdk/attitude
/dji_sdk/battery_state
/dji_sdk/flight_control_setpoint_ENUposition_yaw
/dji_sdk/flight_control_setpoint_ENUvelocity_yawrate
/dji_sdk/flight_control_setpoint_generic
/dji_sdk/flight_control_setpoint_rollpitch_yawrate_zposition
/dji_sdk/flight_status
/dji_sdk/from_mobile_data
/dji_sdk/from_payload_data
/dji_sdk/gimbal_angle
/dji_sdk/gimbal_angle_cmd
/dji_sdk/gimbal_speed_cmd
/dji_sdk/gps_health
/dji_sdk/gps_position
/dji_sdk/height_above_takeoff
/dji_sdk/imu
/dji_sdk/local_frame_ref
/dji_sdk/local_position
/dji_sdk/rc
/dji_sdk/time_sync_fc_time_utc
/dji_sdk/time_sync_gps_utc
/dji_sdk/time_sync_nmea_msg
/dji_sdk/time_sync_pps_source
/dji_sdk/velocity
/dji_sdk/vo_position
/rosout

```

Figure 25: Terminal output of ROS topics available

The baud rate and data rates for the various topics is shown in Table 13.

Table 14 shows the specific output types selected for multiple format parameters. These parameters and output types can be configured in the DJI Assistant computer program. Generally speaking, higher data rates will increase CPU load, whilst a lower data rate might incur under-sampling.

Table 13: The various data parameters and corresponding transmission rates

Data Parameter	Output Rate
Baud Rate	38400
Timestamp	50Hz
Attitude Quaternions	50Hz
Acceleration	10Hz
Velocity (Ground Frame)	10Hz
Angular Velocity (Body Frame)	10Hz
Position	100Hz
Remote Controller Channel Data	10Hz

Table 14: The data type settings of specific vehicle parameters

Data Type Parameters	Data Type
ACC	Raw Data
GYRO	Raw Data
ALTI	Data Fusion
HEIGHT	Altitude to Home Point

7.2.2 Bagging ROS Data

ROS has a feature whereby data can be recorded in a fashion such that it can be played back synchronously with other recorded data sources. This procedure in ROS is known as bagging. This is achieved through a set of ROS tools collectively known as *roscap*. Essentially, *roscap* allows for recording and playing back ROS topics. This is used to record data from the ROS topics mentioned in Table 12 for subsequent post-processing. Once bagged, the data is compressed and stored in a '.bag' format. These bags are

decompressed in a post-processing step. This is a similar concept to a log file except the rosbag can be fed into ROS simulation packages to accurately re-enact the captured data.

7.3 Prototype Software Workflow

7.3.1 Shell Scripts

There are a series of shell scripts which are responsible for automating the execution of the software. These shell scripts are run as part of a *tmux* server. The *tmux* server is essentially a terminal multiplexer. This allows the GCS to view the parallel output from all the various scripts, see Figure 26. There is one master shell script, which synchronises the Pi with the NTP time server. This script then configures the Pi as the ROS master. The script then calls four subsequent shell scripts:

- *start_ros.sh*: Activates ROS on the M100
- *run_servo.sh*: Subscribes to *height_above_takeoff* and *attitude* topics and runs the antenna compensation script
- *srsenb.sh*: Starts the RAN and communicates with the SDR
- *rosbag.sh*: This creates ROS bags of the *gps_position* and *height_above_takeoff* topics
- *htop.sh*: This shows the tasks being run on the Pi and shows available computational overhead

By running these functions as shell-scripts, it allows for a degree of automation.

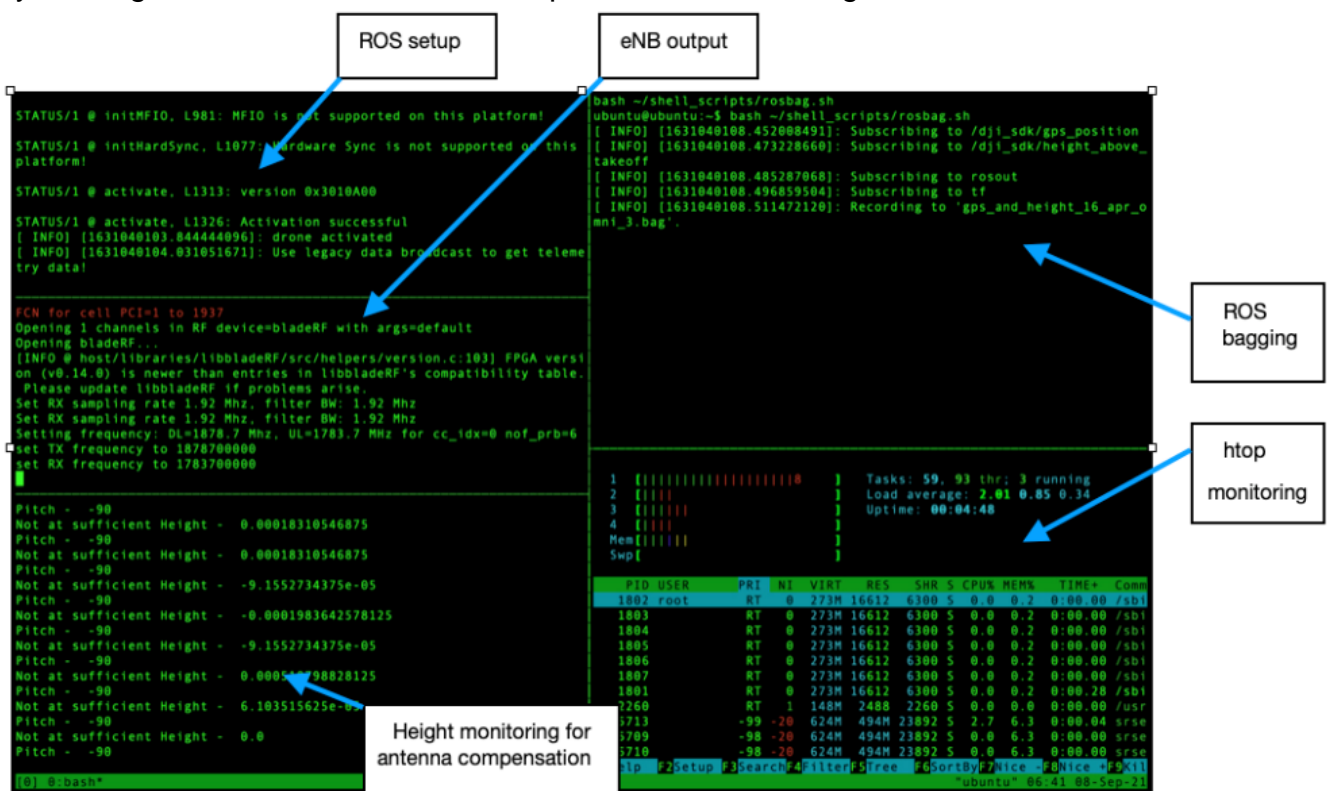


Figure 26: Annotated tmux interface

The workflows depicted in Appendix C show the important steps required for system initiation. The software workflows detailed in Appendix C are all depicted from the perspective of the GCS workstation which is the control centre. The control centre connects to the UAV's onboard Raspberry Pi and the GCS Raspberry Pi via separate SSH sessions.

7.4 Processing Software Workflow

This subsection depicts the processing which occurs once the UAV has landed, and the relevant log files have been extracted from the onboard computer.

There are three major constituent sub-processes which are detailed in the following subsections.

7.4.1 Raw Data Processing

The two files extracted from the onboard computer are:

- eNB log: High verbosity log file containing all radio frontend details. Referenced via timestamp
- ROS bag: A 'bagged' dataset containing flight data. Referenced via timestamp

These two files both need to be processed to extract the relevant data and align with each other based on timestamp. By aligning via timestamp, the cellular metrics can effectively be geo-referenced. The enabling feature which allows these two scripts to be aligned by timestamp is the implementation of a NTP server on the GCS. The GCS acts as a NTP server, from which the other devices in the local network can synchronise to. Interestingly, the different processes running on the onboard computer do not inherently synchronise with the system time, this must be configured manually. The raw data processing is performed by a Python script, which is depicted in Figure 27.

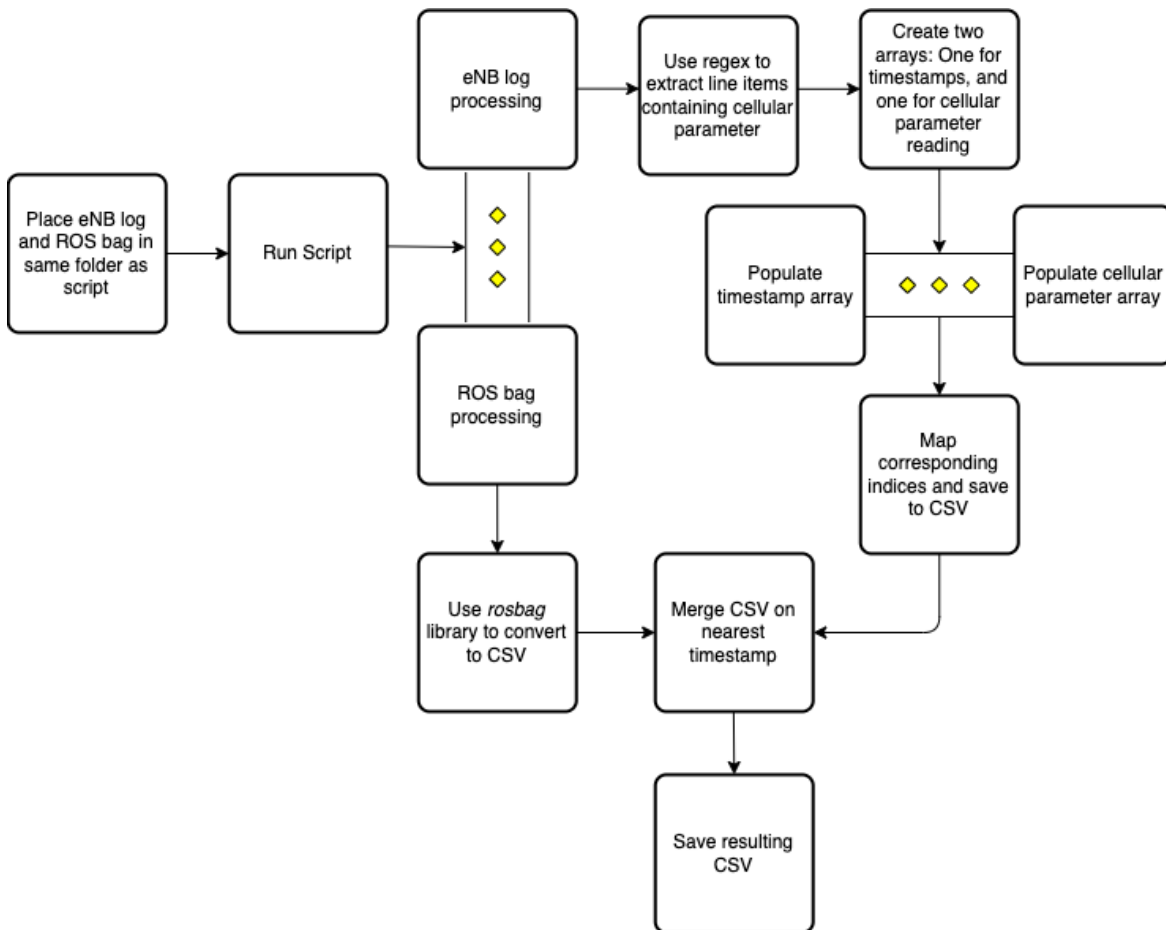


Figure 27: Raw data processing workflow

7.4.2 Raw Image Processing

An additional step to the processing software workflow is the raw image processing. This sub-process takes the geo-referenced images taken from the UAV's onboard camera and effectively 'stitches' the images into an orthomosaic. An orthomosaic is a high resolution, geo-referenced image. Depending on flight height, an orthomosaic can provide a higher resolution base map of the target search area. The workflow is depicted in Figure 28.

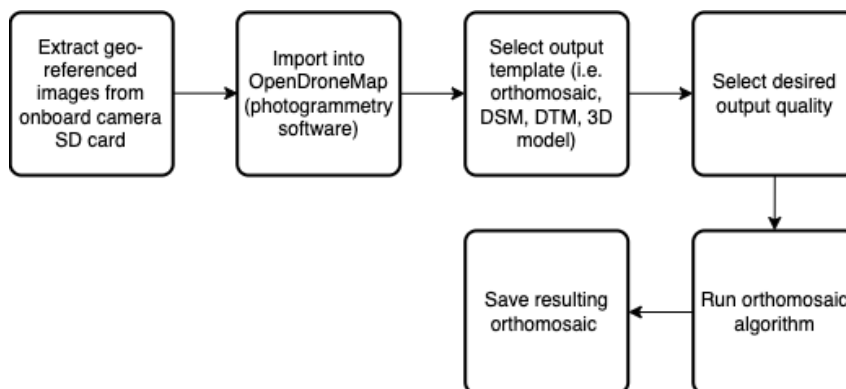


Figure 28: Raw image processing workflow

7.4.3 Geographical Alignment and Post-Processing

This sub-process concerns the importation of the outputs detailed in the previous subsections into GIS software, in this case, QGIS. QGIS is open-source GIS software which allows for extended customisation and plug-in development.

The QGIS project is initialised with a Google Satellite base map and the high-resolution orthomosaic. The Google Satellite base map provides an overarching base map which covers a much larger area than the orthomosaic. The bounds of the orthomosaic are determined by the flight plan. The remaining parts of the workflow are shown in Figure 29.

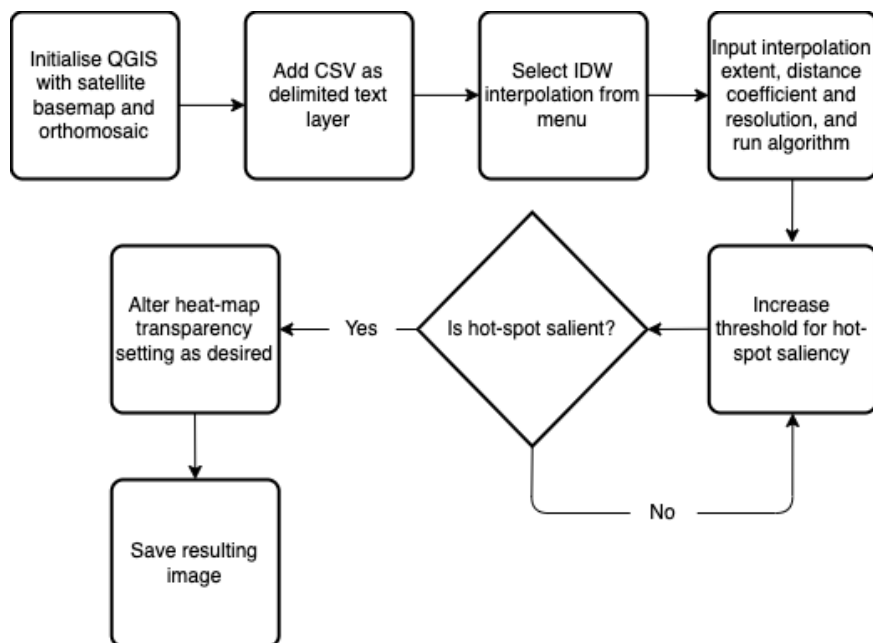


Figure 29: Post-processing workflow

There is an important parameter set in the Inverse Distance Weighting (IDW) interpolation algorithm which has a significant effect on the cellular signal hotspots. This parameter is called the distance coefficient (P). The magnitude of P determines the *influence* of the measured point on the surrounding unknown points as part of the interpolation process. The larger the magnitude of P , the greater the spread of the hotspots. This is essentially a scale factor by which the magnitude and influence of hotspots can be increased.

This brings into question the methodology by which the radial error is measured. In theory, the distance coefficient should have little effect on the radial error if the centroid method is used. The centroid method is to use the centroid of a hotspot as the location of the target. However, if the methodology instead treats the measured location as the nearest point with a certain threshold (e.g., >20 dB), then the distance coefficient would have a much greater effect. Therefore, the radial error measurement method was based on the centroid method.

8. Validation

8.1 Subsystem Testing

There is subsystem testing that can be performed to characterise other aspects of the implementation. One of the key components of this system is the wireless link between the UAV and the GCS. This system needs to stay reliably connected for the system to work as intended. This is also required to answer research subquestion 2. It is also pertinent to validate the output transmission power of the SDR frontend. This provides a realistic measure of output power, which is useful to validate simulation models.

8.1.1 Speed Testing

To verify the need for a directional wireless link, speed-testing was performed between the GCS and the UAV. There were two configurations tested on the GCS Wi-Fi AP:

- Omnidirectional: MikroTik 6dBi omnidirectional antenna
- Directional: 19dBi directional grid-pack antenna

There were two configurations tested on the UAV:

- External: TP-Link TL-WN722N 4dBi 150Mbps Wi-Fi dongle
- Onboard: Raspberry Pi 4 Wi-Fi chip

For the sake of simplicity, these are aggregated into the following configurations:

1. Omnidirectional antenna on GCS and external TL-WN722N dongle on UAV
2. Omnidirectional antenna on GCS and onboard RPi4 Wi-Fi on UAV
3. Directional antenna on GCS and external TL-WN722N dongle on UAV
4. Directional antenna on GCS and onboard RPi4 Wi-Fi on UAV

For testing, the GCS was setup in a static position, and the UAV was flown in a specific flight path. The flight path was performed in a free-space environment at Massey University's Palmerston North campus. There were very few objects for multipath artifacts, and there was a lack of obstructive objects for shadowing. The specific flight path flown was a straight line of approximately 170m in length, as seen in Figure 30. This distance is a good test of the GCS-UAV Wi-Fi link. Figure 31, Figure 32, Figure 33 and Figure 34 show the results of these different configurations respectively.

The speed testing was measured using the network tool *iPerf3*. This tool measures bandwidth from client to server by default. The GCS workstation was set as the server, and the Raspberry Pi 4 was set as the client. The link was tested for TCP traffic to represent the worst-case link bandwidth. This is because TCP is slower than UDP *if* IP packets get lost, due to the re-transmission algorithm.

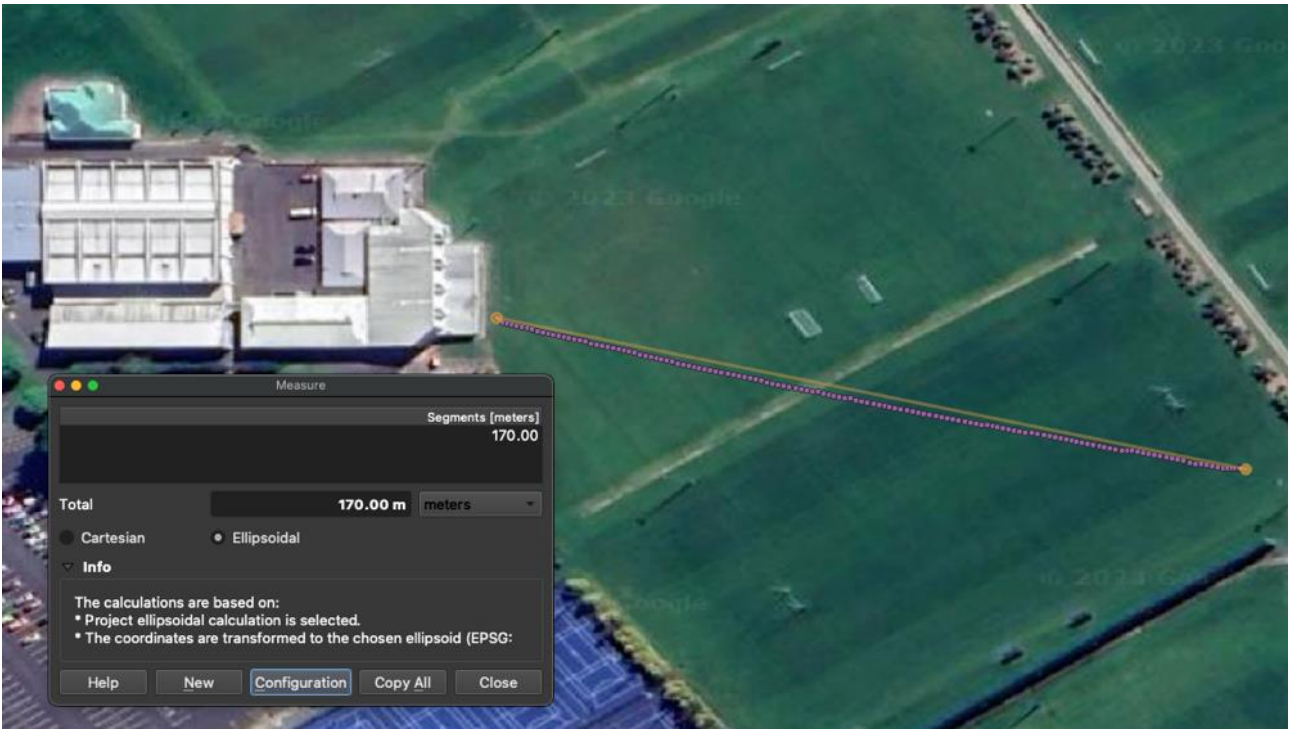


Figure 30: UAV flight path flown for speed testing

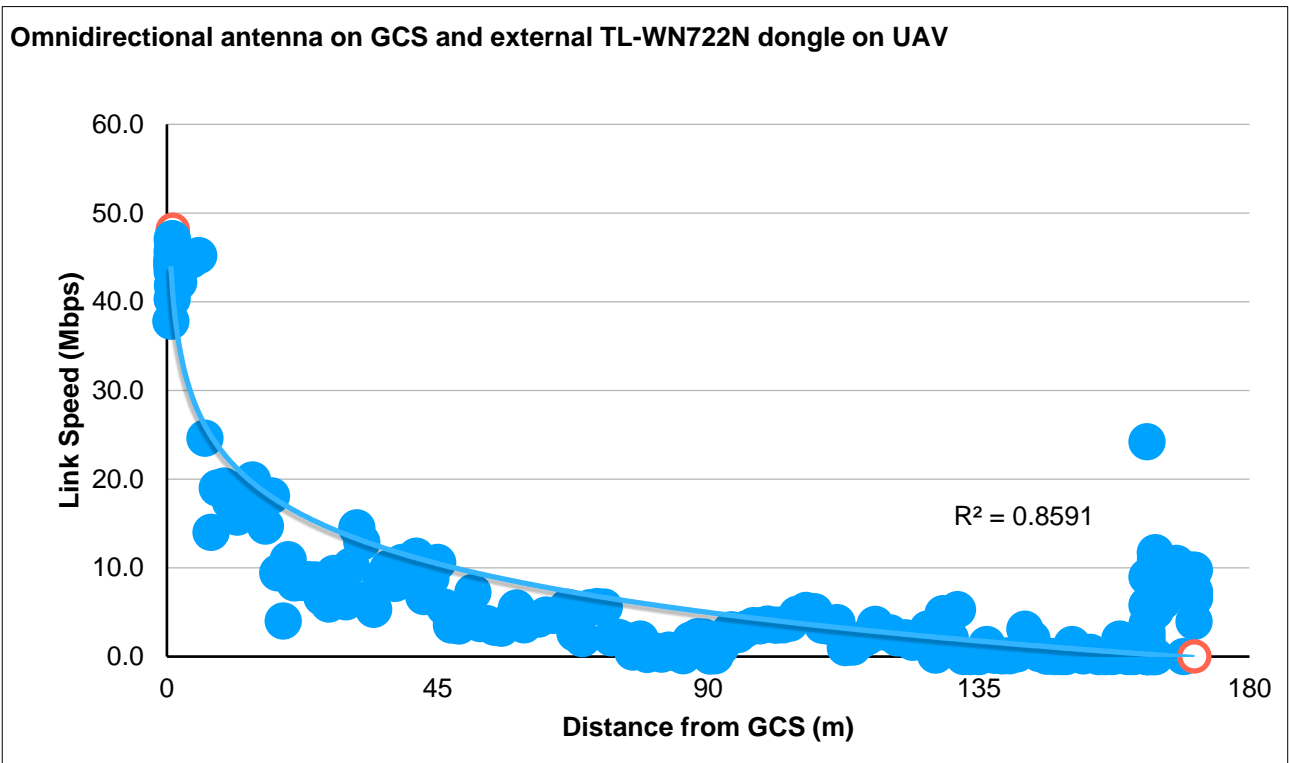


Figure 31: Speed test of omnidirectional antenna on GCS and external dongle on UAV

Average speed of 9.7 Mbps. Maximum of 48.1 Mbps, minimum of 0 Mbps

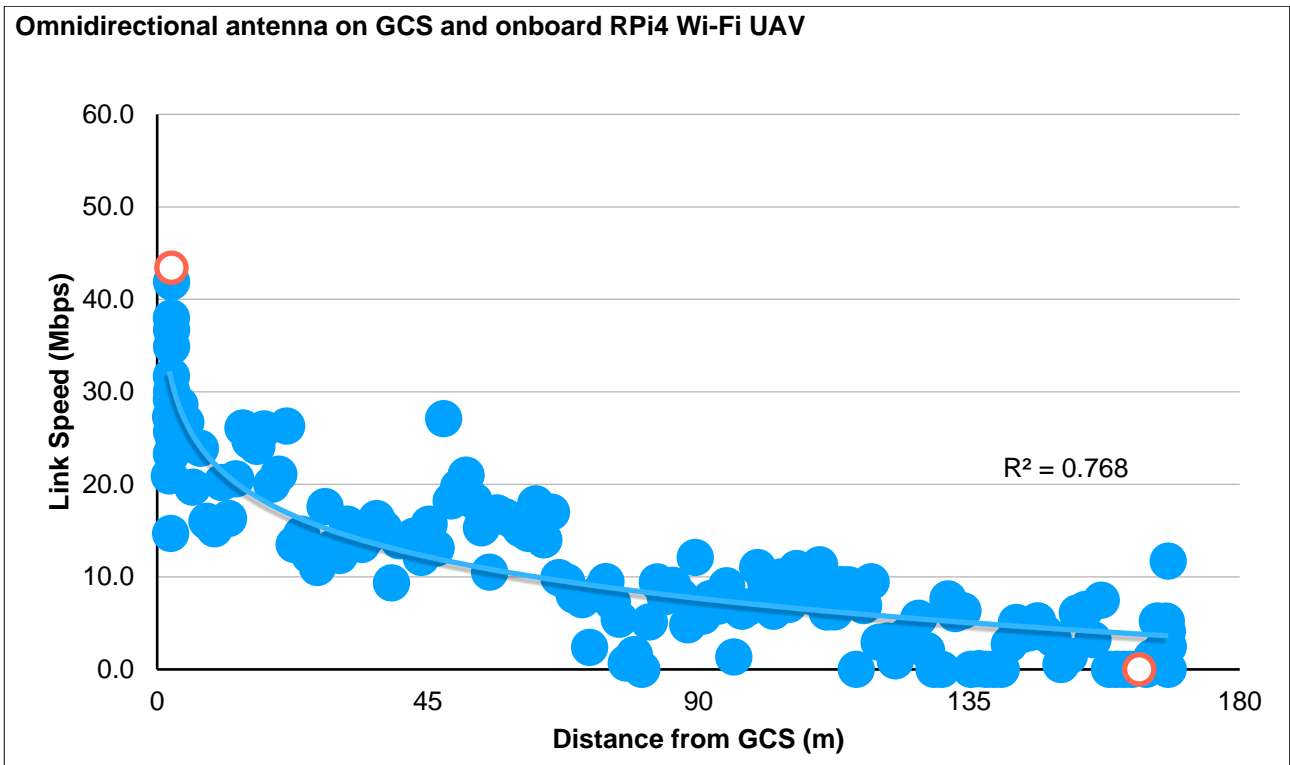


Figure 32: Speed test of omnidirectional antenna on GCS and onboard RPi4 Wi-Fi on UAV

Average speed of 11.7 Mbps. Maximum of 43.4 Mbps, minimum of 0 Mbps

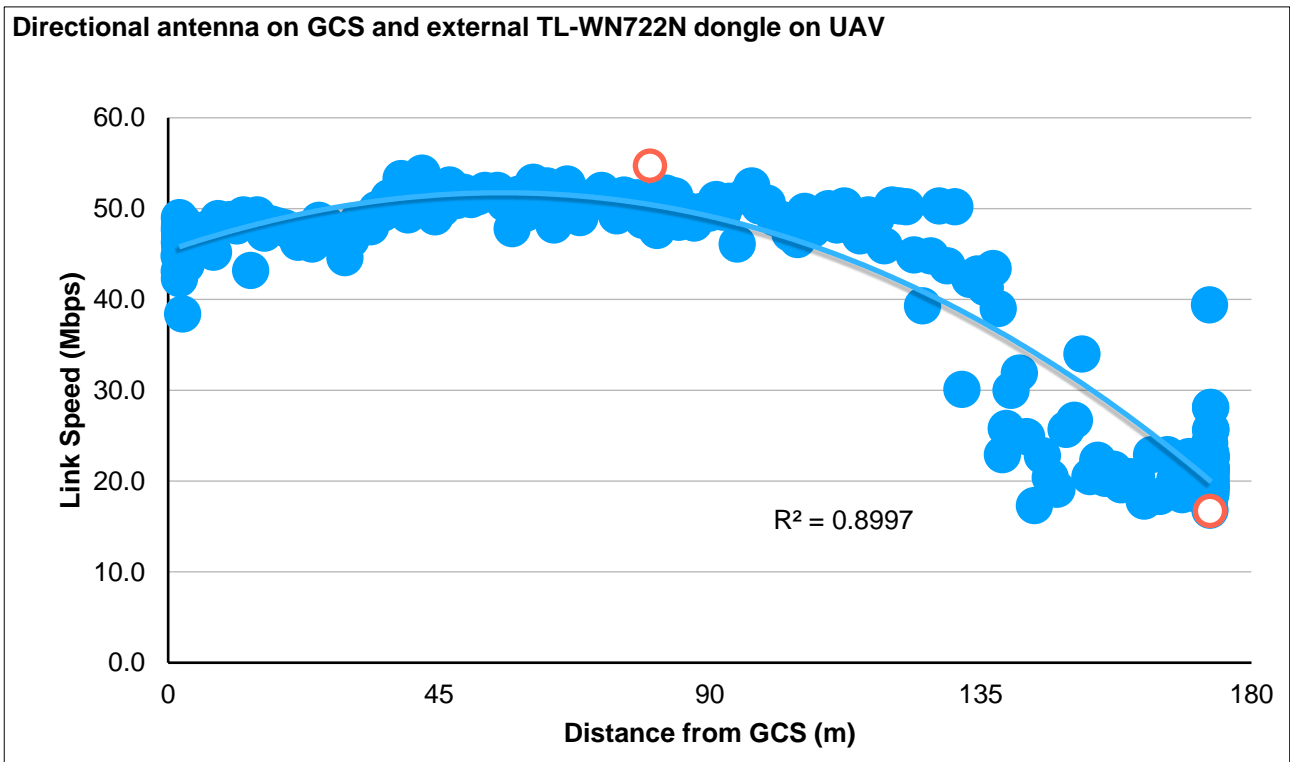


Figure 33: Speed test of directional antenna on GCS and external dongle on UAV

Average speed of 39.3 Mbps. Maximum of 54.7 Mbps, minimum of 16.7 Mbps.

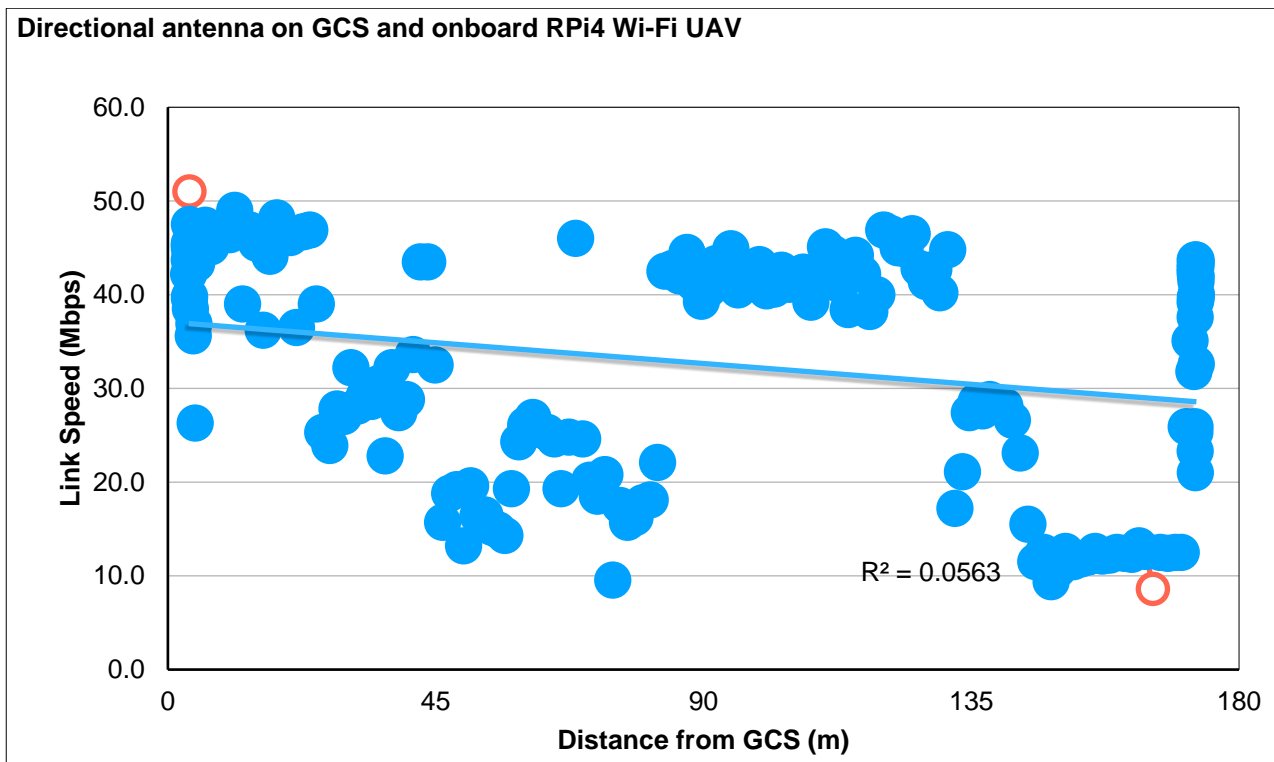


Figure 34: Speed test of directional antenna on GCS and onboard RPi4 Wi-Fi on UAV

Average speed of 32.5 Mbps. Maximum of 51 Mbps, minimum of 8.59 Mbps.

In the figures above, the minimum and maximum values are emphasised for clarity. The R^2 value for each fitted curve is shown to determine how well each trend line fits the data. Figure 31 and Figure 32 are fitted with logarithmic trendlines, showing relatively high R^2 values. Figure 33 is fitted with a 2nd order polynomial which gives the highest R^2 value of all the results. Figure 34 gives the most sporadic dataset, and is fitted with a linear trendline, yielding the lowest R^2 value. This highlights the variability of this configuration where the directional antenna is used on the GCS and the onboard Raspberry Pi 4 Wi-Fi is used on the UAV.

The most important criterion of the GCS - UAV link, is that it never reaches a speed near 0 Mbps. It can be seen from the above results that the combinations involving the omnidirectional antenna on the GCS do not fit this criterion. Therefore, the directional antenna is warranted on the GCS. It appears configuration 3 mentioned above (Directional antenna on GCS and external TL-WN722N dongle on the UAV) yielded the best performance (Average speed of 39.3 Mbps. Maximum of 54.7 Mbps, minimum of 16.7 Mbps). Therefore, this was the optimal configuration chosen for the proposed system. Curiously, the maximum decay rate of link speed as a function of distance is greatest for this configuration after 90m. This contrasts with configurations 1 and 2 in which the maximum decay rate occurs between 0m and 45m. In contrast to the Wi-Fi link range calculation in subsection 5.3.4, a link speed of ≥ 50 Mbps is possible when the distance between GCS and UAV is less than approximately 140m. This distance factored in choosing the maximum size of the test areas in preliminary and primary testing. This mismatch in distance between theoretical and realistic distance values can be attributed to factors such as computational throughput limitations on the *iPerf3* client or server. Furthermore, the bandwidth was tested with TCP packets, which has reduced bandwidth

(as compared to UDP) if there are lost packets due to retransmissions. Due to relatively good performance, it is assumed that configuration 3 will be sufficient.

According to Coldrey, Engström et al. (2014) and Coldrey, Berg et al. (2013), the minimum backhaul bitrates for small LTE cells is around 50Mbps. This is an estimate for users who are utilising 20MHz of bandwidth (corresponding to 100 PRBs). This bitrate is characteristic of a small cell, where there are several users streaming. However, in the context of search and rescue, there is not necessarily a need to support high bitrates for streaming. In this proposed system, the number of PRBs is constrained to 6, corresponding to a bandwidth of 1.4MHz.

8.1.2 BladeRF Channel Power

Another aspect that needs to be tested is the output power of the SDR frontend as a function of the variable parameters. The primary power output parameter that can be varied from within the srsENB configuration scripts is *tx_gain*. This parameter can be set to any value between 1 and 100. It is unknown what the scaling factor of this parameter is with respect to measurable output power, hence why this needs to be tested. A representative setup for the radio frontend was used as seen in Figure 35. For this test, the BT-100 PA was attached to the TX port of the BladeRF xA4 such that the test setup was similar to what is seen at the input port of the directional antenna. Remember that the directional TX antenna has an approximate gain of 9dBi.

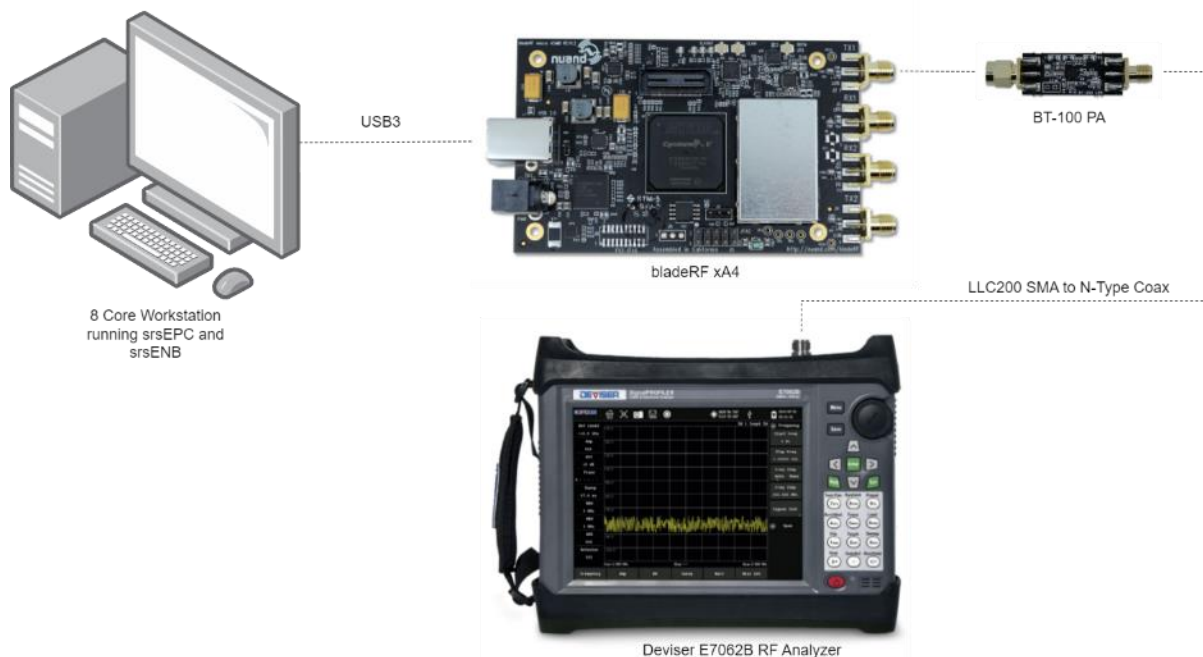


Figure 35: Test Setup for Output Power Analysis

The Channel Measurement mode on the Deviser E7062B RF Analyzer was used to characterise the output power as a function of channel bandwidth. This was tested with two different PRB settings; PRB of 6 and PRB of 100. The results can be seen in Figure 36.

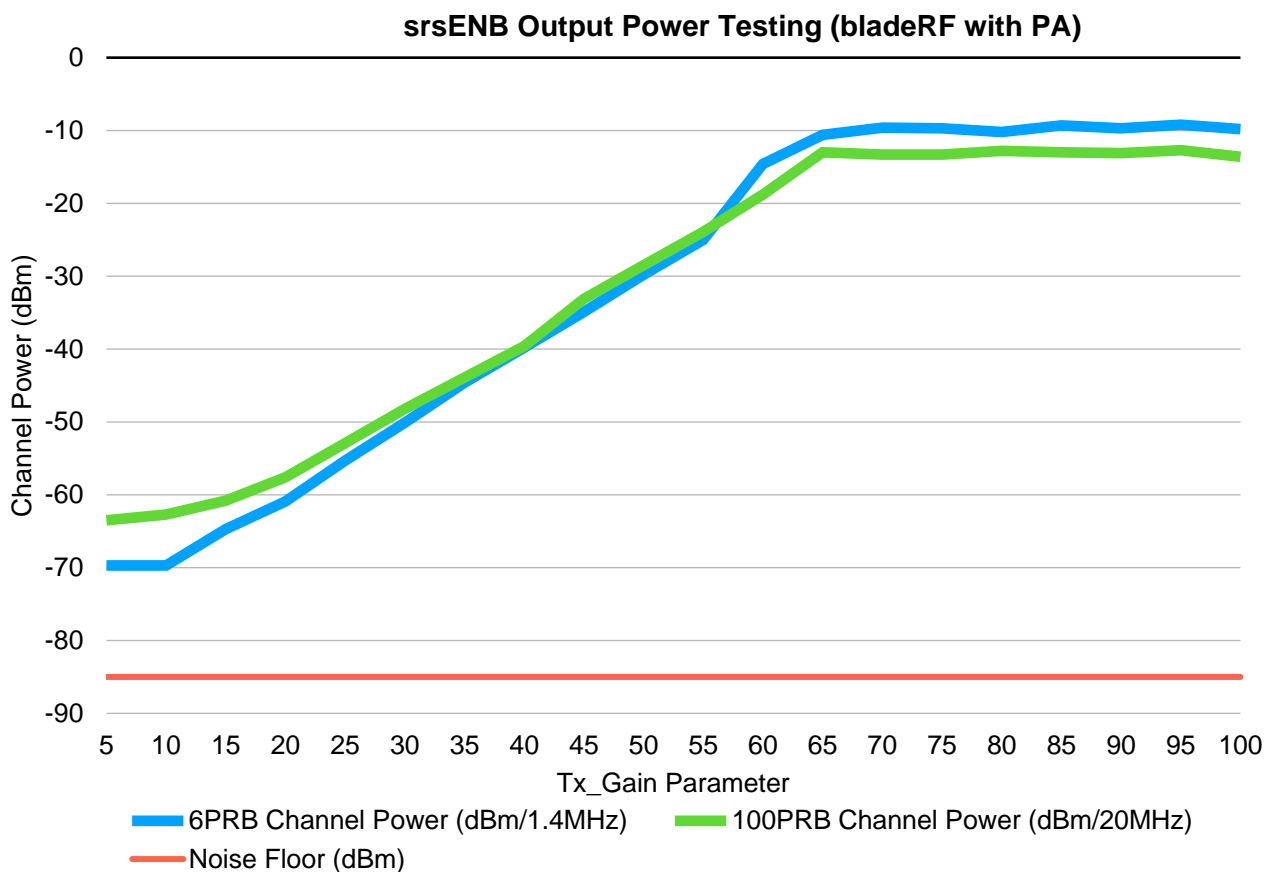


Figure 36: srsENB Output Power Testing Results

The following observations can be ascertained from Figure 36:

1. The channel power for both PRB settings saturates near -10dBm from a *tx_gain* between 70 and 100.
2. A PRB setting of 6 appears to have greater channel power than that of 100 PRB when the *tx_gain* parameter is >70.
3. The -10dBm peak channel power is 28dB lower than the maximum specified CW output power of the BladeRF xA4 as mentioned in subsection 6.3.3.

Due to observation 1 above, the *tx_gain* parameter was chosen to remain static at 75dB (see Table 11). This is because a *tx_gain* of 75 yields the maximum channel power from the SDR frontend. Observation 2 seems intuitive, as a PRB of 100 equates to a bandwidth of 20MHz, whereas a PRB of 6 equates to a bandwidth of 1.4MHz. Observation 3 is perhaps the most surprising. A CW signal occupies a very small bandwidth, less than 10Hz. Therefore, the AD9361 IC on the BladeRF is capable of injecting much more power into a smaller bandwidth CW signal in comparison to a 1.4MHz signal. Furthermore, the BT-100 PA attached to the BladeRF has an amplification factor that varies with frequency and bandwidth, and appears to add 8dB of gain at 1878.7MHz for a 1.4MHz bandwidth.

8.2 Preliminary Testing

8.2.1 Testing Objective

The objective behind preliminary testing was to prove the principle of operation with some fixed and varying parameters. A goal of this testing was to benchmark the performance of the system and understand the most influential factors on the output of the system. Simply put, the principle of operation is to use parameters extracted from the onboard cellular RAN to inform the position of target mobile phones in the testing area. For the preliminary testing, the flight parameters can be seen in Table 15.

Table 15: The fixed and variable parameters defined for preliminary testing

Aspect	Fixed/Variable
Flight height	Fixed below 30m (20m for preliminary test 1 and 2, 30m for preliminary test 3)
Flight speed	Fixed 0.6m/s
Flight heading	Variable: 0-180°
Testing area	Fixed area, with variable target UE positions within test area

8.2.2 Test Methodology

Preliminary testing was performed in a low complexity environment with some tall objects nearby. The intention behind using this environment was to observe the effect (if any) of potential multipath. Also of note, is the fact that these tests were performed on separate occasions, unlike the primary testing which was performed on the same day. Initially, the ground station is placed at a point such that it can continuously track the position of the UAV within the bounds of the testing area. An additional consideration is the flight speed of the UAV. The distance at which the ground station should be placed depends upon the maximum flight speed of the UAV. However, for the flight speed used in preliminary testing (0.6m/s), the ground station can be relatively close. Next, the target mobile phone is placed in a specific location and its latitude and longitude is recorded using the mobile phone's onboard sensors.

The EPC is then started on the GCS workstation, and the tracking station is initialised. Once the GCS is initiated, the UAV is then booted up, and the eNB is started. The target mobile phone must be connected to the eNB prior to take-off. While the UE attach procedure is completing between the UE and the eNB, the flight path of the UAV is programmed on the Pix4DCapture app in accordance with the parameters shown in Table 15. Once the flight plan has been finalised and the mobile phone is connected to the eNB, the UAV is commanded to take-off.

Once the UAV has completed its grid-style flight path, the UAV lands. The required log files are extracted while the EPC and eNB systems are deactivated. The log files are promptly processed on the GCS workstation, alongside the orthomosaic stitching process. These steps can be seen in the process flow diagrams in Appendix C.

8.2.3 Preliminary Test 1

This test was performed at a 20m flight height, with a 290° flight heading.

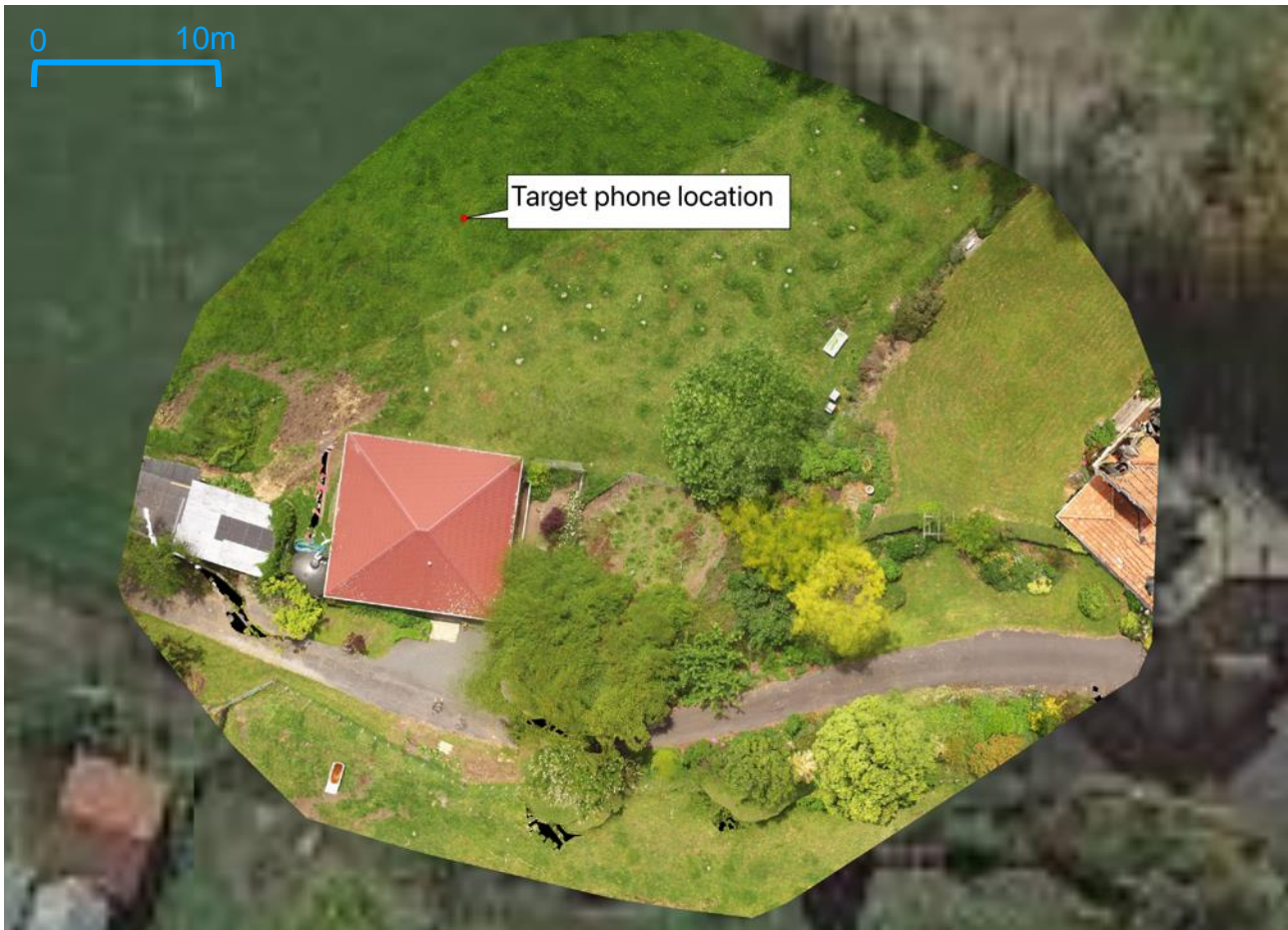


Figure 37: Orthomosaic layer overlaid on satellite base map showing UE location

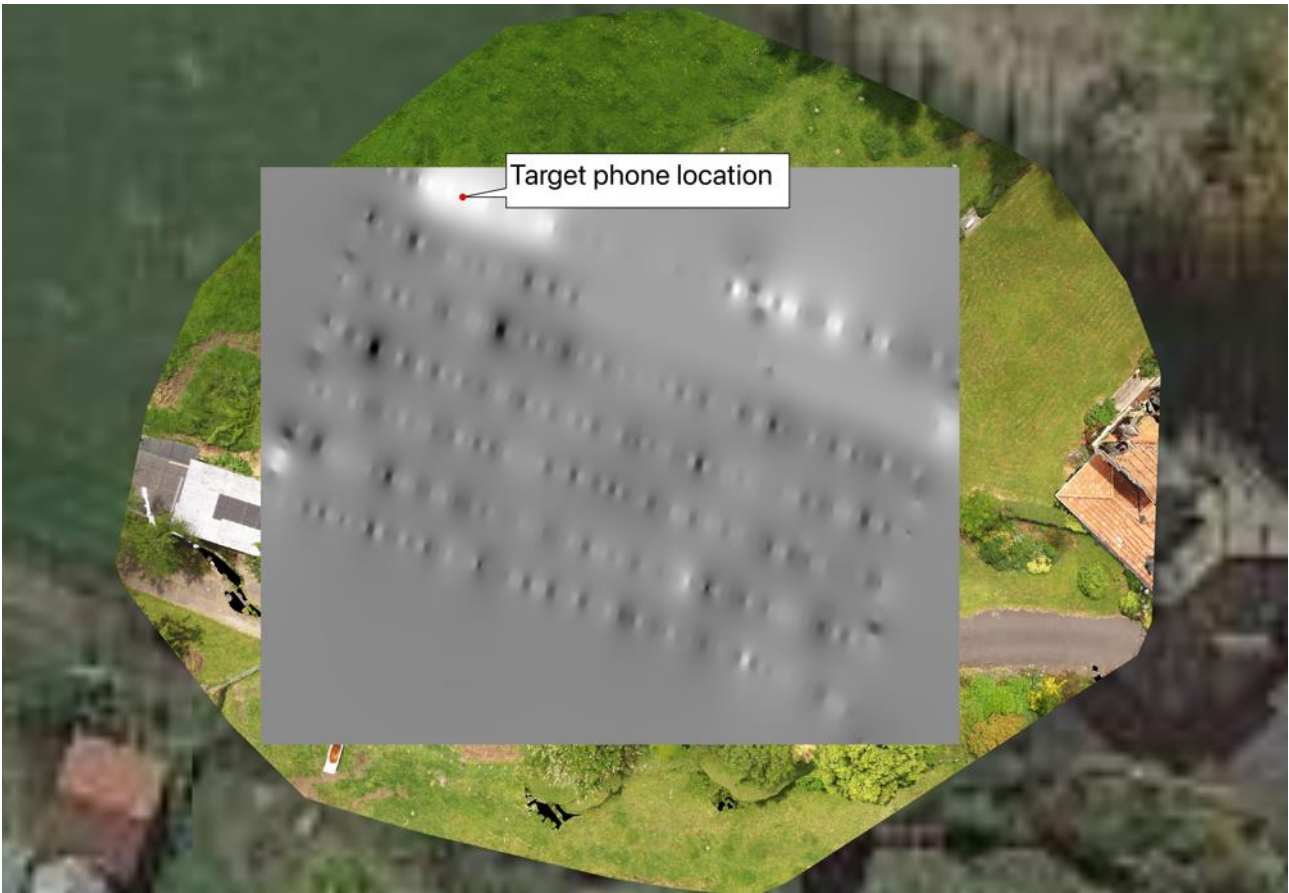


Figure 38: EPRE heat-map overlaid on top of base maps



Figure 39: Heat-map thresholded for EPRE values > 10dBFS

Figure 37 shows the test site with the orthomosaic overlaid on the Google Satellite base map. Note the increased resolution afforded by the orthomosaic as compared to the Google Satellite base map. Figure 38 shows the processed heatmap overlaid on the orthomosaic. Figure 39 shows the heatmap thresholded for EPRE values greater than 10dBFS. This value was manually selected based on how salient the primary hotspot appeared to be. The thresholded hotspot correlates well with the location of the target mobile phone. The main hotspot near the mobile phone is of higher EPRE than the erroneous hotspots in the heat-map. If this threshold is increased, then the main hotspot would be the only hotspot in the heat-map, however this would reduce the size of the main hotspot, as the edges of the hotspot would have lower EPRE than the centre of the hotspot. There are some additional image-processing techniques which can be applied to isolate the largest hotspot without requiring further thresholding. These techniques were not investigated for preliminary testing.

8.2.4 Preliminary Test 2

This test was performed at a 20m flight height, with a 30° flight heading. The intention of this test was to briefly investigate the difference in result that could arise from a different flight heading. The placement of the mobile phone is also slightly different than that of preliminary test 1. The location differs by approximately 30m from the phone location in preliminary test 1.



Figure 40: Orthomosaic layer overlaid on satellite base map showing phone location

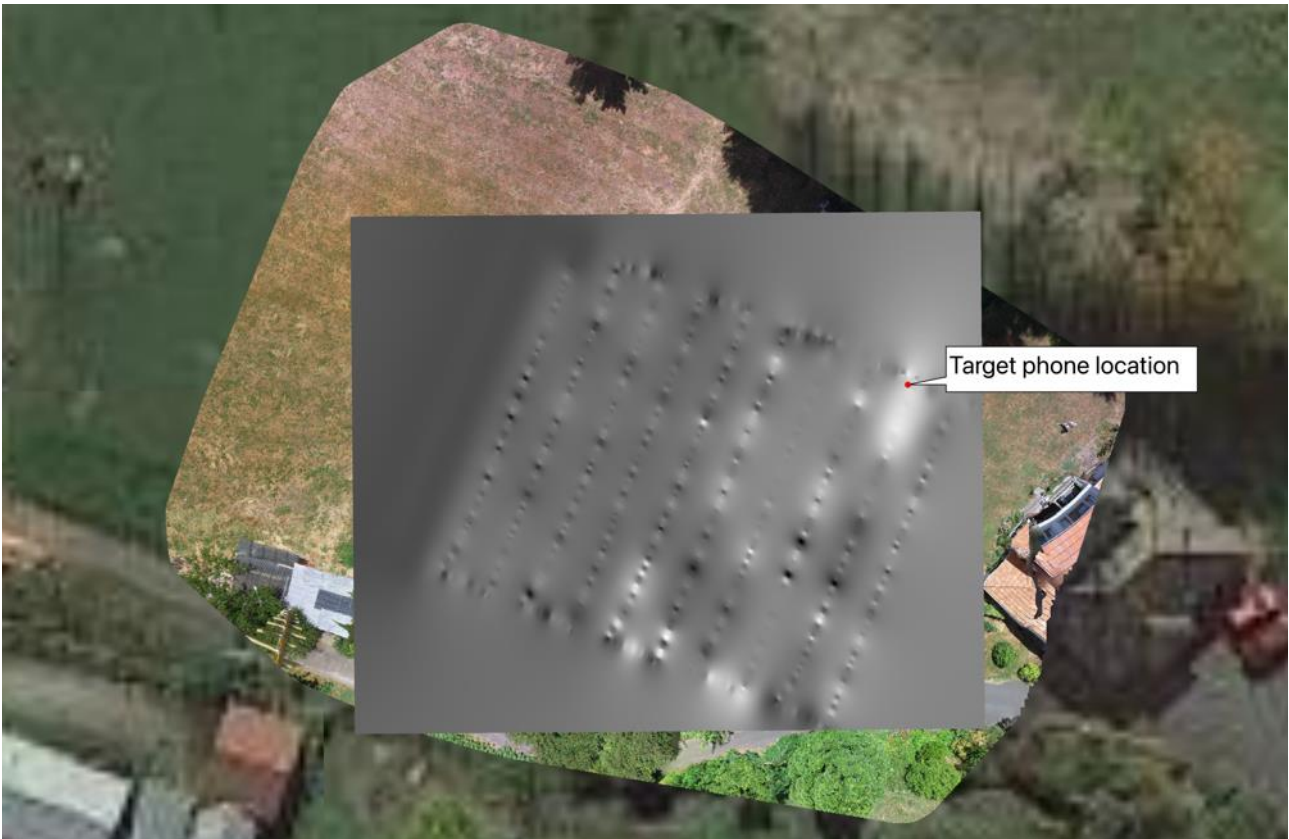


Figure 41: EPRE Heat-map overlaid on top of base maps



Figure 42: Heat-map thresholded for EPRE values > 10dBFS

Figure 40 shows the test site with the orthomosaic overlaid on the Google Satellite base map. Figure 41 shows the processed heatmap overlaid on the orthomosaic. Figure 42 shows the heatmap thresholded for EPRE values greater than 10dBFS (manually selected). The main hotspot near the mobile phone is *not* of higher EPRE than the other erroneous hotspots in the heat-map. However, it is the largest hotspot. It also seems as though the main hotspot is weaker (i.e., lower EPRE) than the main hotspot in preliminary test 1 and preliminary test 3. This could be related to the proximity of the UE to taller objects in the testing environment, whereby multipath components could be affecting the results. This interaction is speculative. The location of the main hotspot correlates well with the location of the target mobile phone. This test had a different flight path to that of preliminary test 1, whereby the flight path was offset in the direction orthogonal to the parallel flight passes in preliminary test 1. This difference in result could also suggest that there is an interaction between the antenna polarisation of the target mobile phone and the cellular receiver antenna on the UAV. However, the underlying cause is unknown.

8.2.5 Preliminary Test 3

This test was performed at a 30m flight height, with a 30° flight heading. The intention of this test was to replicate preliminary test 2 at a slightly higher altitude.



Figure 43: Orthomosaic layer overlaid on satellite base map showing phone location

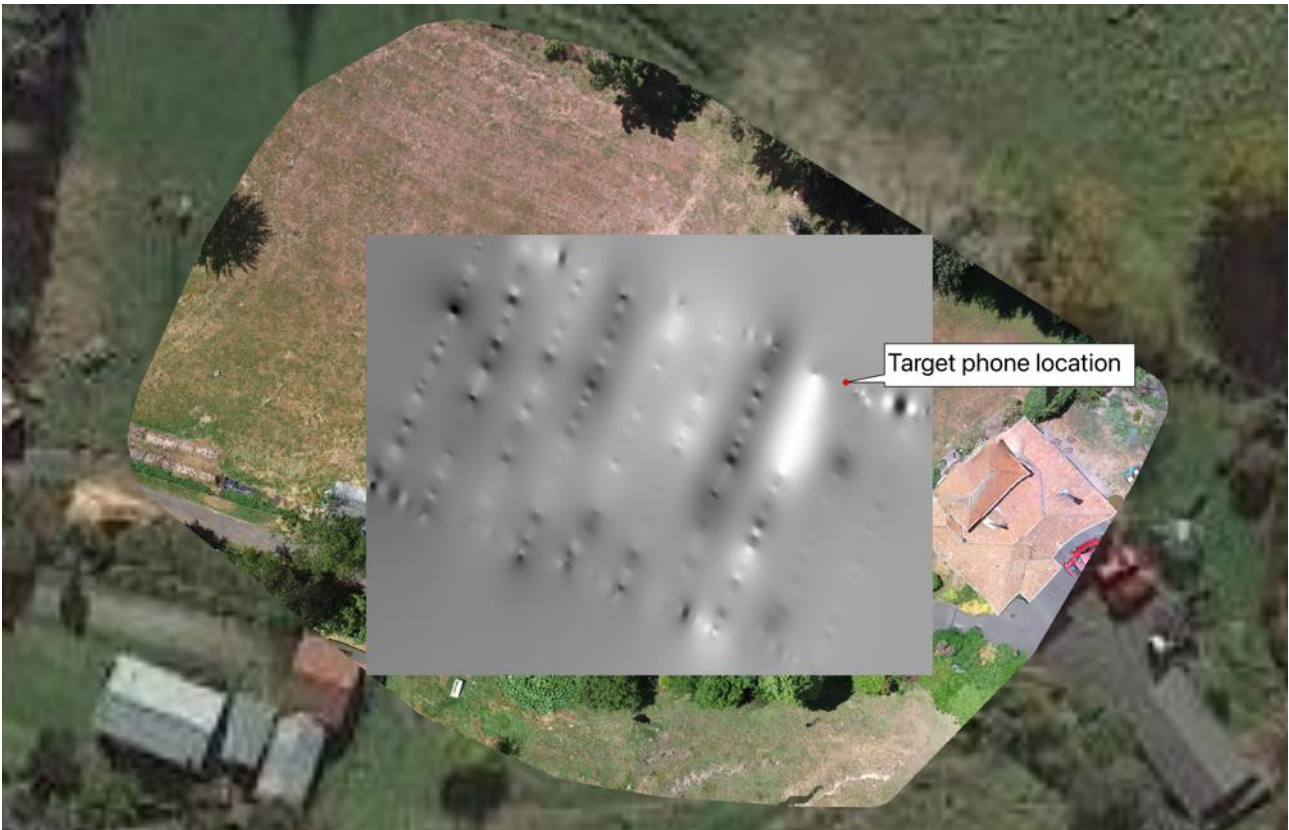


Figure 44: EPRE heat-map overlaid on top of base maps

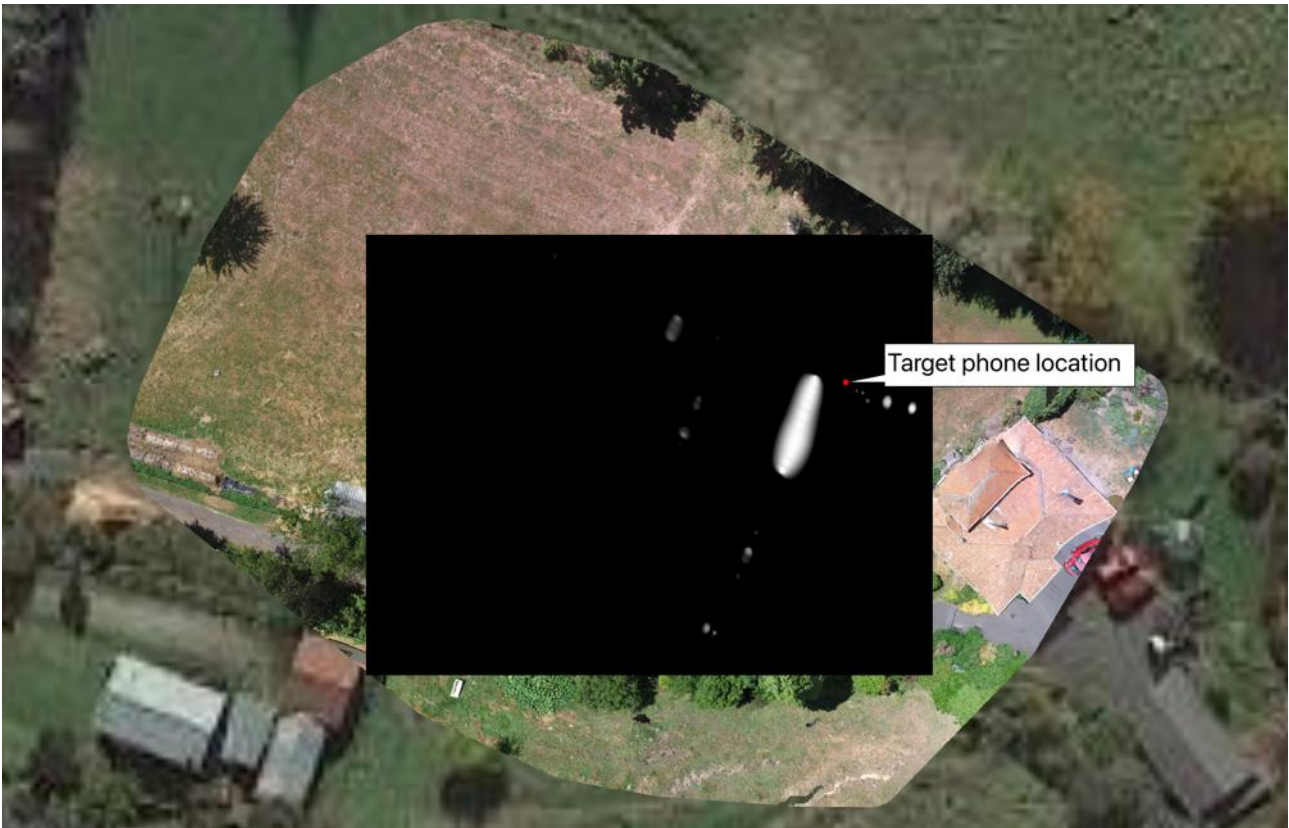


Figure 45: Heat-map thresholded for EPRE values > 15dBFS

Figure 43 shows the test site with the orthomosaic overlaid on the Google Satellite base map. Figure 44 shows the processed heatmap overlaid on the orthomosaic. Figure 45 shows the heatmap thresholded for EPRE values greater than 15dBFS (manually selected). Interestingly, the threshold for primary hotspot saliency was 5dB higher in preliminary test 3 relative to preliminary test 1 and 2. The main hotspot near the mobile phone is of a higher EPRE than the other erroneous hotspots in the heat-map and appears to be more uniform than that of preliminary test 2. This could suggest an interaction of the flight height on the strength of the hotspot. This hotspot is also the largest hotspot. However there appears to be an offset between the hotspot and the target phone location. This can be analysed further by observing the adjacent flightpath passes relative to the location of the target mobile phone, as seen in Figure 46.

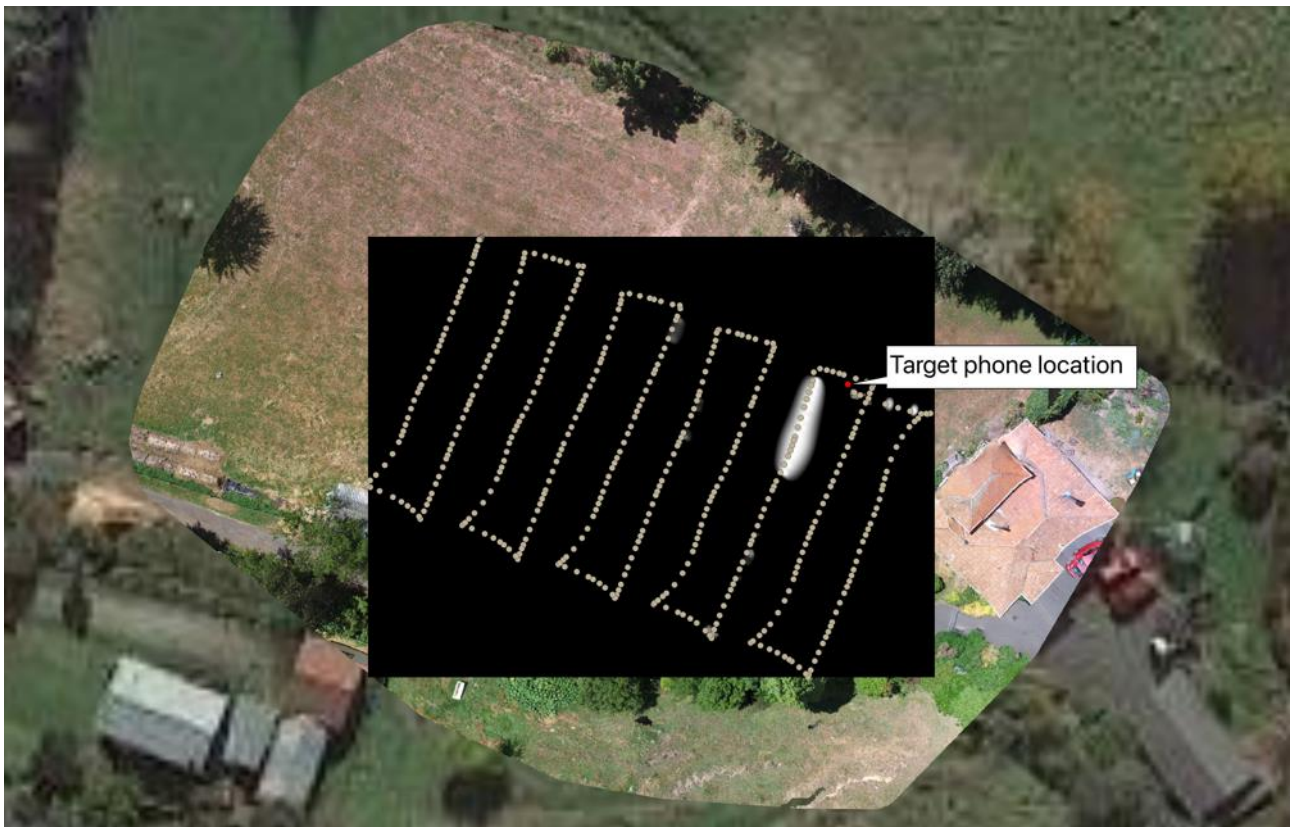


Figure 46: The flight path relative to the heat-map

The longer sides of the flight-path passes are the reliable data points due to the polarisation of the directional antenna aboard the UAV. The shorter orthogonal lengths are where the UAV is changing heading directions, and therefore the directional antenna is changing polarisations. The target mobile phone location is in between two of the longer, adjacent flightpath passes. Therefore, the hotspot is representative of the location of the target mobile phone. Interestingly, the adjacent parallel flight pass does not indicate higher EPRE considering the proximity of the target mobile phone, it is unknown as to why this is the case. The flight height of this test was 30m, as opposed to 20m. This means that the distance between parallel flight passes is also larger and slightly offset, which seems to characterise this observation well. In preliminary test 1 and 2, the flight path appears to pass directly over the mobile phone location. There could be a localisation error that is equivalent to the distance between parallel flight passes.

8.2.6 Observations

The results from these three tests seems to validate the technical feasibility of the system. The results gained go a long way in answering the research questions. In all three results detailed here, the locations of the main hotspots seems to correlate quite well with the locations of the target mobile phone. It can also be observed that there are several erroneous hotspots in the results which are somewhat random. These can be removed using image processing techniques, such as segmentation and contour analysis. For example, contour analysis could be used to discern between the relatively smooth contours of genuine hotspots and erroneous hotspots. This has not been investigated for preliminary testing. The cause of said hotspots could be due to several different factors, which are out of scope of preliminary testing. There are several potential interactions highlighted in these tests, however none of them have been validated during preliminary testing. These are all speculative.

As mentioned previously, the mobile phone's onboard GPS was used to measure its latitude and longitude. Along with the latitude and longitude values, the accuracy of the reading was supplied. For all tests, the reading was taken once the accuracy reached 5m (i.e., waiting for the GPS fix to settle sufficiently). Even though this step was followed in the workflow, it was found that the variation in this reading was significant with respect to the size of the test area, as seen in Figure 47. In this figure, the static location of the test mobile phone was collected for four separate consecutive tests. The target phone's perceived GPS location varied as much as 8m.

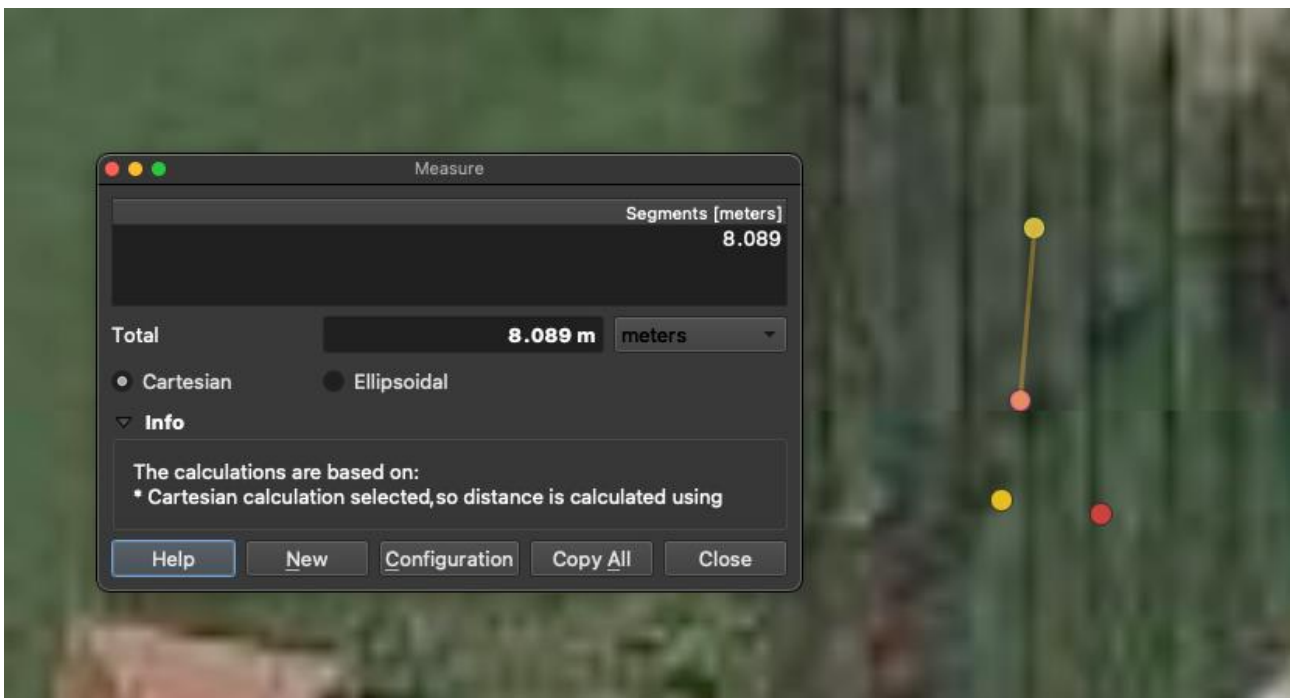


Figure 47: The error between consecutive static positions of UE

Additionally, the UAV's GPS is fundamental to the accuracy of the system. The accuracy of the UAV's GPS sensor is $\pm 2\text{m}$ (Rodrigues, Patrikar et al. 2021), which introduces inherent error. Using a UAV enabled with Real Time Kinematics (RTK) would allow for much higher accuracy, e.g., $\pm 6\text{cm}$ (Elkhrachy 2021).

8.3 Primary Testing

Prior to primary testing, observations from preliminary testing were used to formulate some improvements that were implemented for primary testing.

8.3.1 Post-testing Improvements

There were a few improvements made between the preliminary testing phase and the primary testing phase. These are listed below:

- Improved position fix of target UE: This improvement is necessary due to the positioning error that can be observed in Figure 47. This was implemented by using a dedicated external GPS receiver which was able to obtain a 'healthier' fix.
- Real-time feedback on UE's connection status: This improvement is necessary to ensure that the UE remains connected throughout the duration of the test and does not exceed either the Radio Link Failure (RLF) timer or RRC inactivity timer. This proved to be an issue during development testing (prior to preliminary testing). This was implemented by enhancing the verbosity of the EPC log.
- Enhanced thresholding and distance factor scaling: During preliminary testing, the choice of distance factor within the IDW interpolation algorithm was rather primitive and was an iterative process. Additionally, thresholding was iterative, to achieve a salient output. For primary testing, this distance factor was fixed, and the thresholding methodology was changed to calculate the maximum hotspot power, and then set the threshold to this value minus 2dB.
- Representative flight parameters: The heights of the tests were more representative of a real-world use-case scenario. Whereby the flight height would scale better with ground area coverage and battery life of the UAV. I.e., 60m flight height instead of 20m.
- Evaluating localisation accuracy: During preliminary testing, there was no distinct measure of how accurate the 'calculated' location of the target mobile phone was. This has since been resolved and the centroid method is used. This method simplifies the IDW algorithm parameters as well, since scaling the distance factor beyond a certain value has no effect on the accuracy.

8.3.2 Testing Methodology

The methodology of the primary testing was based heavily on answering the research subquestions. Both research subquestions have been somewhat answered during preliminary testing. Primary testing was based on two factors:

- Height difference: Test 1 and Test 2 are 60m and 80m flight heights respectively
- Repeatability: Test 2 and Test 3 are both 80m flight heights

Test 4 was performed with the directional antenna substituted for a 3dBi omnidirectional antenna, oriented in the same polarisation as the omnidirectional receiver antenna. For all the subsequent tests, the mobile phone was placed at the same location.

8.3.3 Testing Environment

The environment chosen for primary testing was dense forest and bush, as seen in Figure 48. This type of environment was chosen due to its applicability to the realistic use case of such a system. This environment had a relatively low noise floor as compared to the preliminary testing site. This is advantageous due to the lack of discrete filtering hardware on the SDR frontend. Having an inherently lower noise floor is conducive to more accurate benchmarking of the system. The flight plan bounds were chosen such that the Wi-Fi link range maintained a link speed of $\geq 50\text{Mbps}$.



Figure 48: Satellite base map of primary testing site showing 60m flight path

The test results touched on in the remainder of chapter 8 are all performed at the same location with *identical* flight area bounds. Additionally, these were all performed on the same day with indiscernible weather changes. This is to ensure repeatability across the results, and isolate which factors affect the results. As a summary:

- Primary test 1 (60m) and primary test 2 (80m) differ only by the flight height
- Primary test 2 and primary test 3 exhibit the same flight parameters and are intended to show the repeatability of the system
- Primary test 4 (60m) shows the effect of using a 3dBi omnidirectional antenna instead of the nadir directional antenna attached to the PA of the TX1 port of the BladeRF xA4.

8.3.4 Primary Test 1

This test was performed at a 60m flight height and 115° flight heading. This flight heading was chosen such that the initial UAV heading was into the wind. This would allow for the antenna compensation mechanism to account for any unintended pitching of the UAV. The flight height of 60m was chosen to have sufficient clearance over the forest canopy. The maximum height of the canopy was approximately 40m. Furthermore, 60m is a common flight height for photogrammetry flight plans as it strikes a good trade-off between ground sampling distance and flight time (as a function of battery life). The raw heat map is shown in Figure 49. Figure 50 shows the fully processed heat-map.

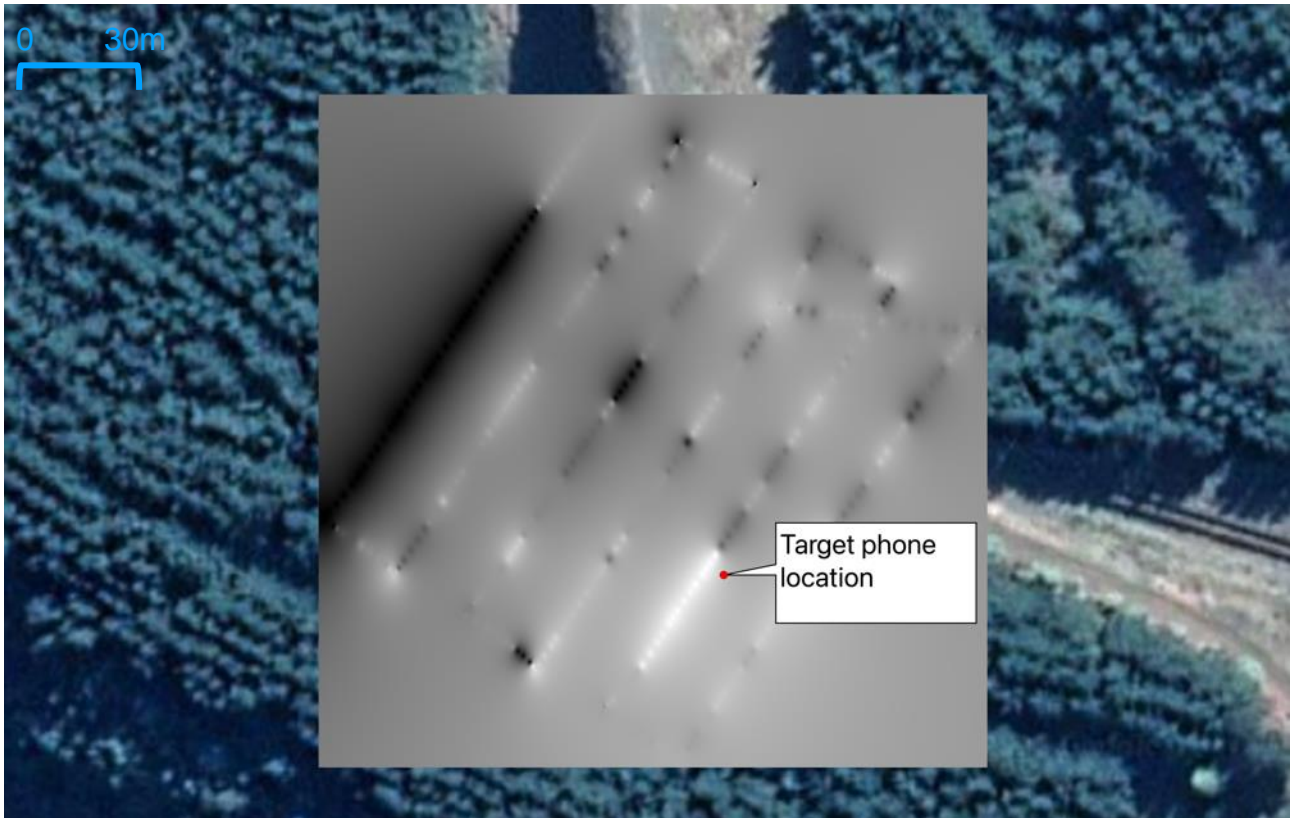


Figure 49: Unprocessed heat-map from primary test 1

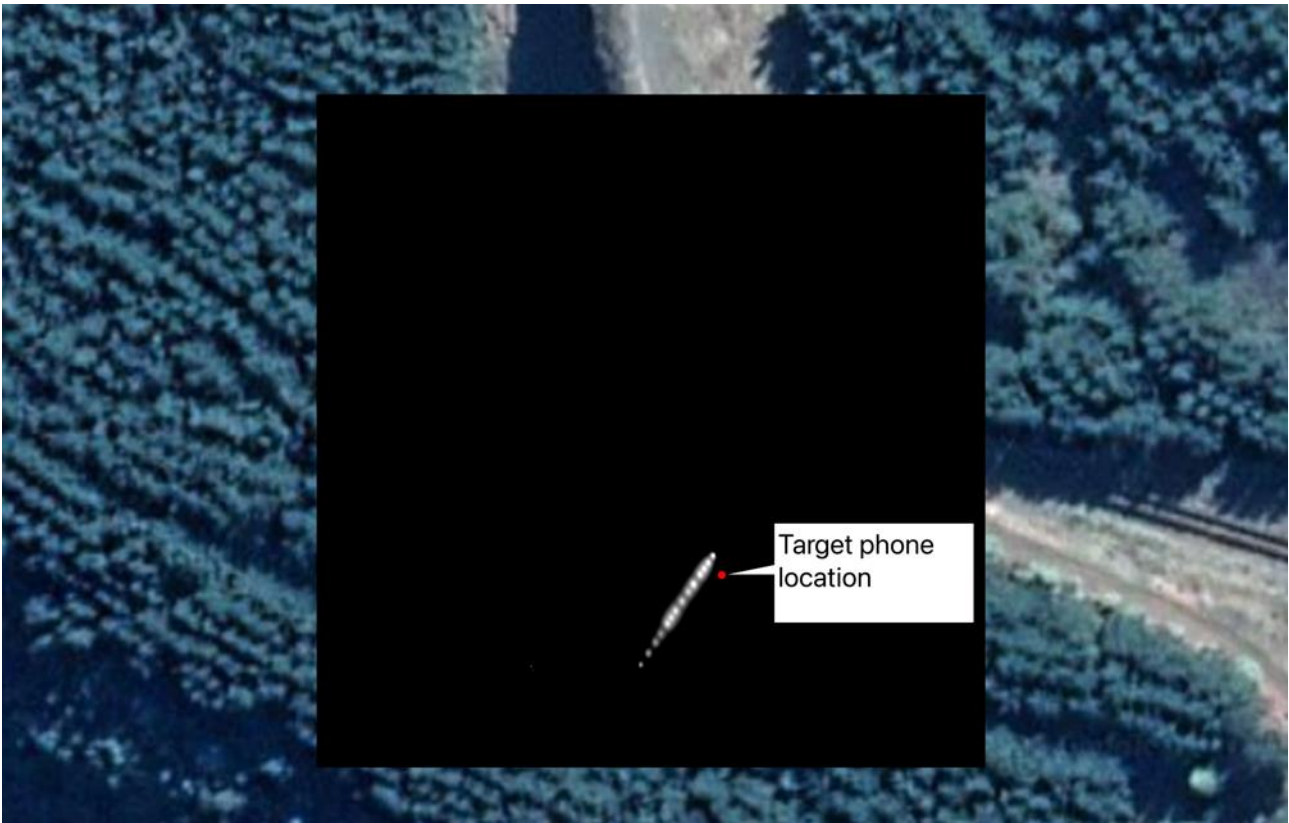


Figure 50: Fully processed heat-map from primary test 1

From observing Figure 50, it can be seen that the hotspot is local to the mobile phone, in fact, if this threshold is increased, the erroneous hotspots are removed.

There is a radial error of approximately 4.3m from the target phone's measured location to the centroid of the primary hotspot. Given that the GPS reading (of the UAV's onboard GPS) has an inherent error of $\pm 5\text{m}$, this result is within the error bounds of the system.

Whilst its more of a qualitative result than a quantitative result, it can be seen in Figure 51 that the orthophoto becomes useful when the transparency of the heat-map is reduced such that the hotspots are visible on the lower base map layers. This could be quite a useful visual tool to help first responders analyse the whereabouts of the target at a higher resolution. This also provides a more relevant base map for locating victims relative to a satellite base map (especially if the satellite base map is out of date).



Figure 51: Enhanced saliency provided by orthophoto base map

8.3.5 Primary Test 2

This test was performed at an 80m flight height, and a 115° flight heading. The increased altitude of this test compared to primary test 1 should, in theory, increase the radial error between the calculated and actual mobile phone locations.

The unprocessed raw heat map is shown in Figure 52, and the processed heat map is shown in Figure 53.

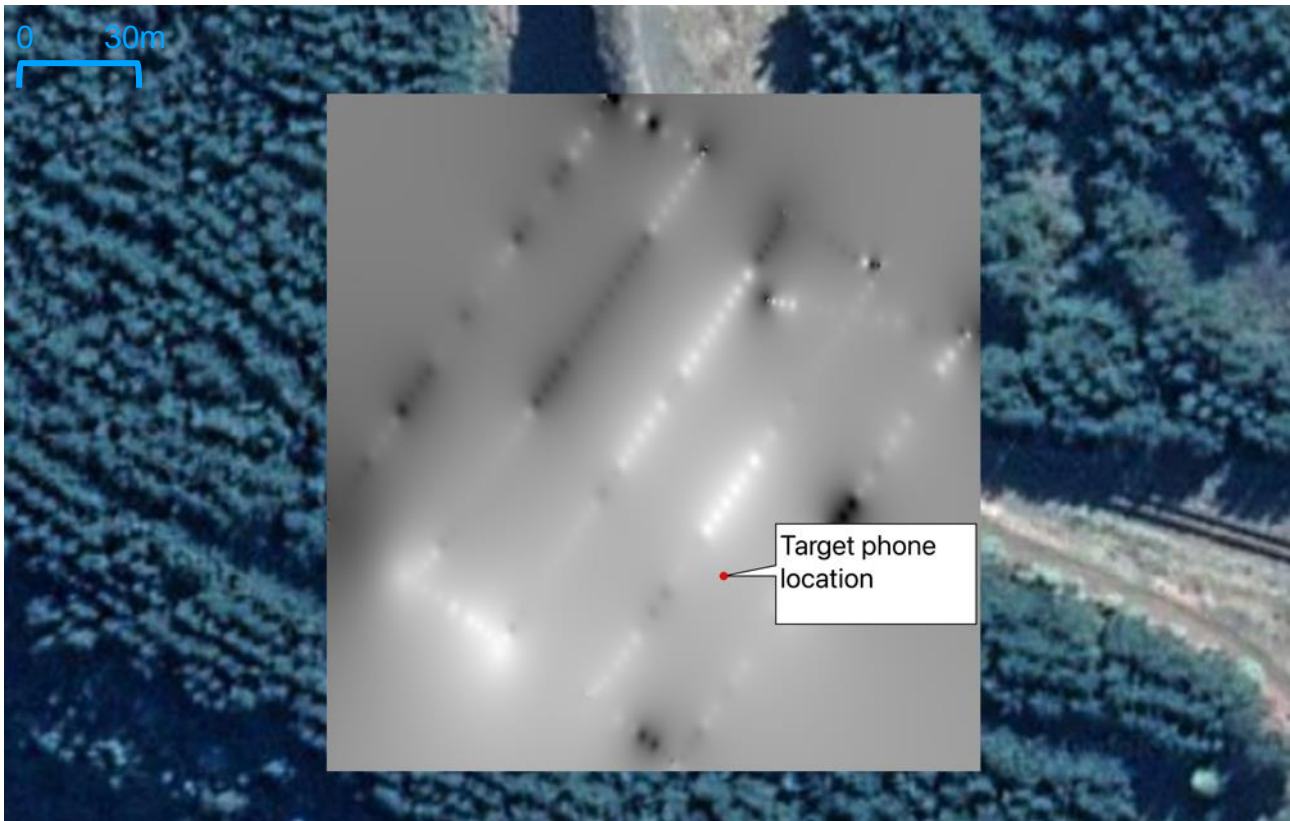


Figure 52: Unprocessed heat-map from primary test 2

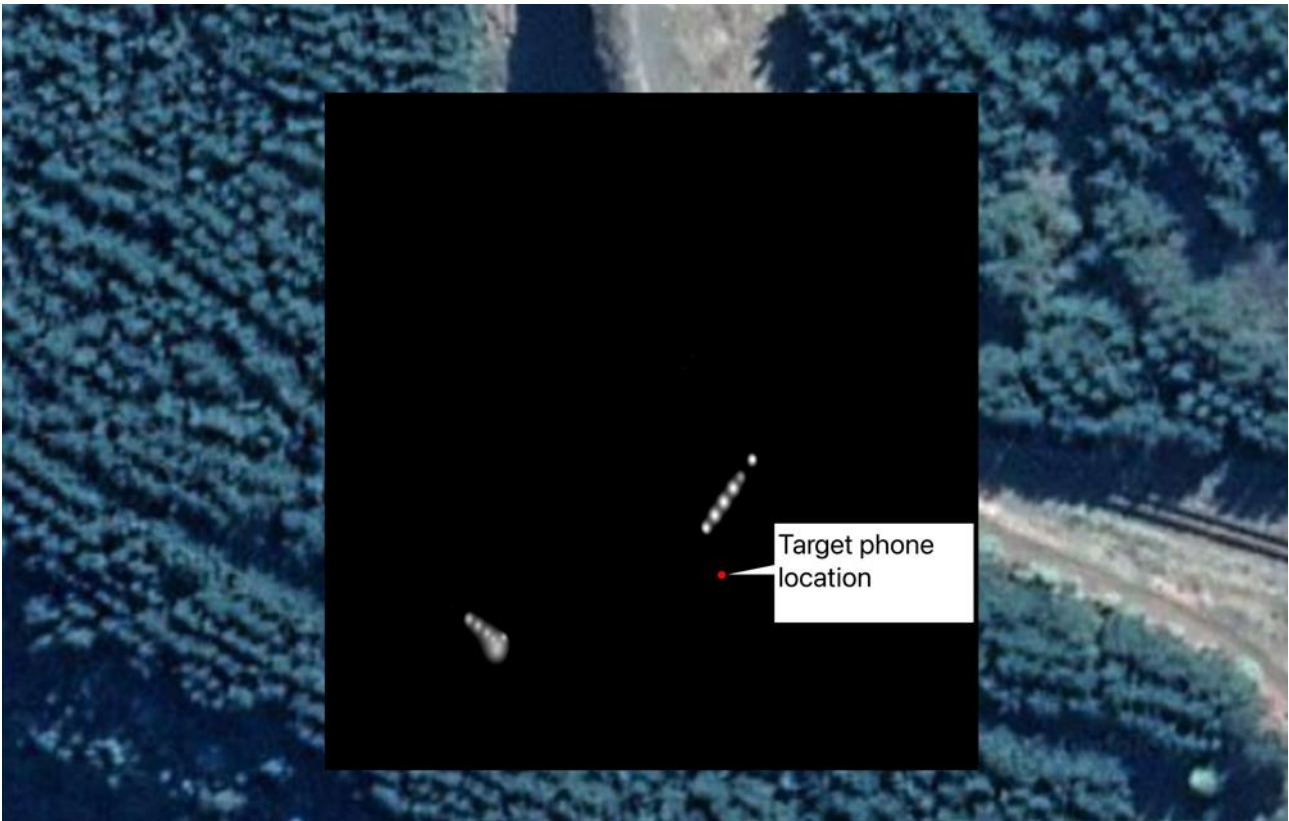


Figure 53: Fully processed heat-map from primary test 2

From observing Figure 53, a radial error of approximately 11.5m exists between the target phone's measured location and the centroid of the primary hotspot. Taking the UAV's inherent GPS error into account, this result is outside the error bounds of the system. However, the additional error can likely be attributed to the increased flight height. One factor that significantly contributes to the radial error is the positioning of the parallel flight paths relative to the actual nadir position of the mobile phone, as seen in preliminary test 3. This is not easily adjustable. Furthermore, adjusting this positioning such that the UAV's flight path aligned with the nadir position of the mobile phone would not be representative of a real use-case.

It would seem intuitive that a greater flight altitude would induce a larger error in the results, this could *also* be attributed to the inherent roll and tilt error that is caused by wind gusts, as seen in Figure 54. While the tilt error is largely compensated for by the movement of the antenna compensation mechanism, the roll angle cannot be compensated for. It is also important to note that there is latency to this compensation control loop. Incidentally, it would be difficult to isolate roll error as the cause of error in results because the adjacent flight path gap provides inherent offsets in the lateral direction. Furthermore, these respective errors are likely to occur in conjunction with each other, and not necessarily in an isolated fashion. One way to determine whether roll error causes this error, would be to record the IMU data from the UAV via ROS and correct the position of the location data post-operatively. However, the maximum accuracy of the onboard IMU is $\pm 2^\circ$ (Rodrigues, Patrikar et al. 2021). At a height of 80m, this could result in a potential error of approximately 2.8m.

It can also be seen from Figure 53 that there is a similar power hotspot further south-west of the target mobile phone. The length of this hotspot is orthogonal to the primary hotspot. This hotspot occurred as the UAV was turning around to start the next parallel flight path. As the UAV turns, it performs a roll and yaw manoeuvre. This means that roll error (as depicted in Figure 54) can be a factor in the error. Furthermore, when the UAV is yawing i.e., turning corners, the polarisation of the directional antenna is changing relative to the mobile phone. This change in polarisation has not been accounted for in the post-processing workflow, and there is likely to be erroneous readings occurring when the cellular receiver antenna changes polarisations. This could be accounted for in real world scenarios by ensuring the flight coverage is large enough to be able to discount the readings measured during turning manoeuvres, or if the data recorded during turning manoeuvres is scrubbed or interpolated.

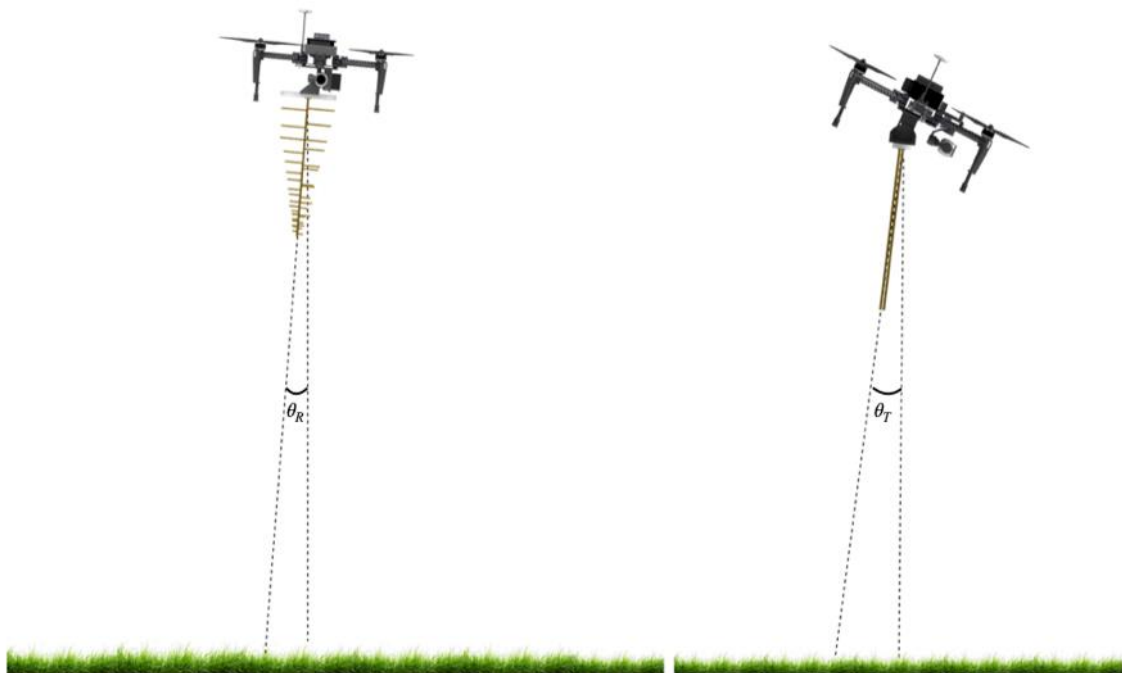


Figure 54: Roll error (θ_R) and tilt error (θ_T) during flight

8.3.6 Primary Test 3

This test was performed at an 80m flight height, with a 115° flight heading, and is intended to validate the repeatability of the system by emulating primary test 2. The unprocessed raw heat map is shown in Figure 55, and the processed heat map is shown in Figure 56.

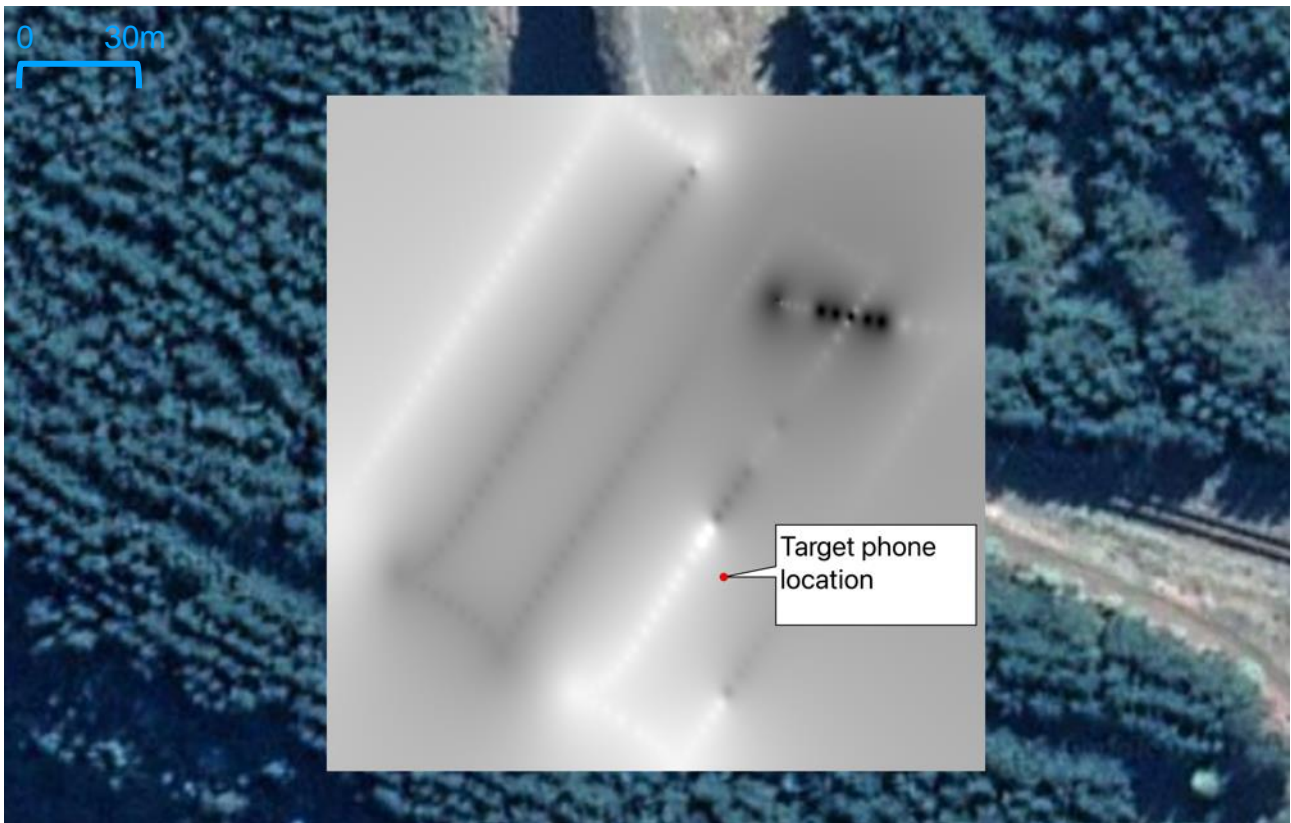


Figure 55: Unprocessed heat-map from primary test 3



Figure 56: Fully processed heat-map from primary test 3

From observing Figure 56, a radial error of approximately 9.6m exists between the target phone's measured location and the centroid of the hotspot. Again, this is outside the error

bounds of the system. In a similar fashion to primary test 2, the error can likely be attributed to the flight height of the UAV, as well as partially attributable to inherent roll error. However, this result yields a slightly lower error than that recorded in primary test 2. There are some common observations that can be noted between primary test 2 and 3:

- The centroid of the hotspot is north-west of the target mobile phone's recorded location. This is in contrast with the hotspot in primary test 1, which is south-west of the target mobile phone. The cause of which is unknown.
- The hotspot is along the same parallel flight pass as primary test 2, and is not present on the adjacent flight passes.

8.3.7 Primary Test 4

This test was performed using a 3dBi omnidirectional antenna attached to the PA instead of the nadir directional antenna. This test was performed with the intention of answering research subquestion 1 (see subsection 1.2). This flight was performed at 60m with otherwise identical parameters to that of Primary Test 1 and Primary Test 2. The unprocessed heat-map is shown in Figure 57.

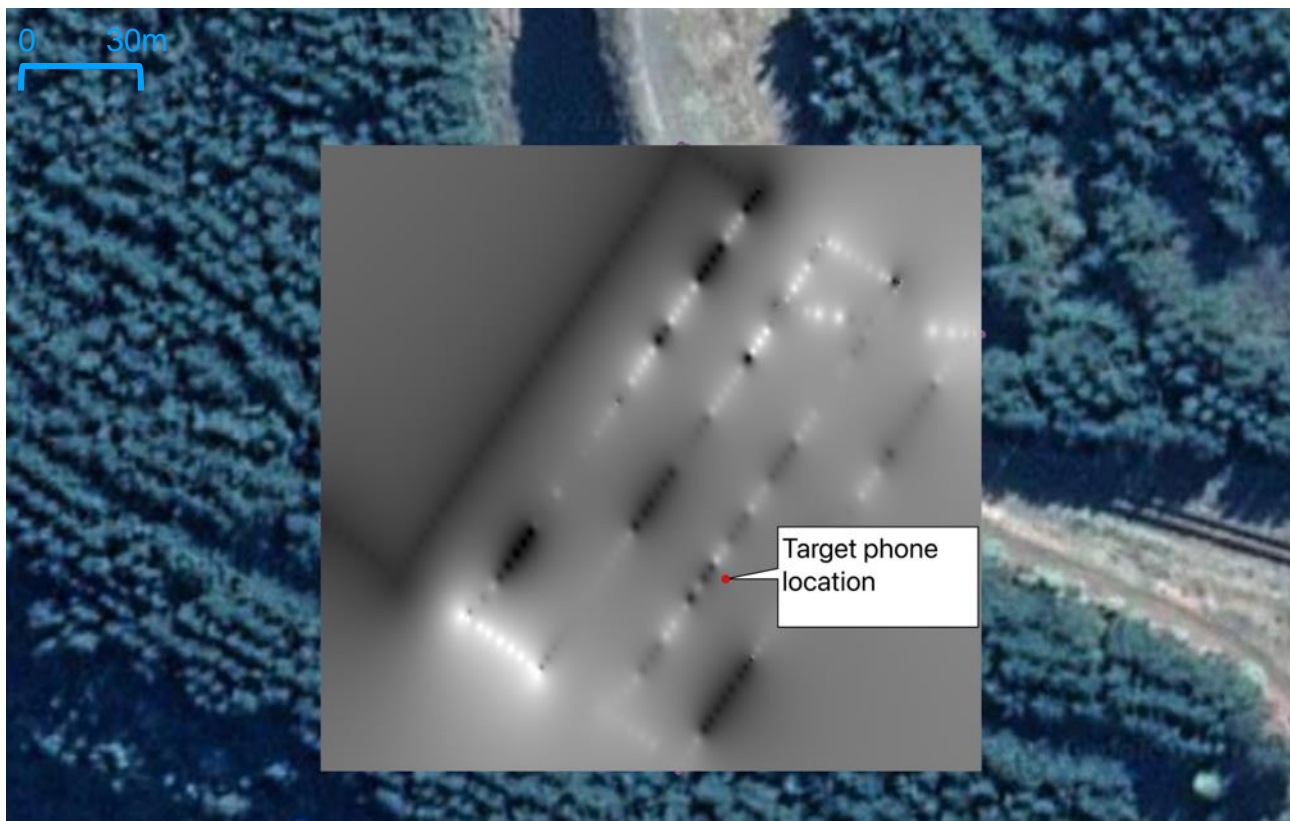


Figure 57: Unprocessed heat-map from primary test 4

The peak value recorded during this test was 5dBFS. This is in stark contrast to the peak values recorded in the directional tests. The thresholded heatmap is shown in Figure 58.

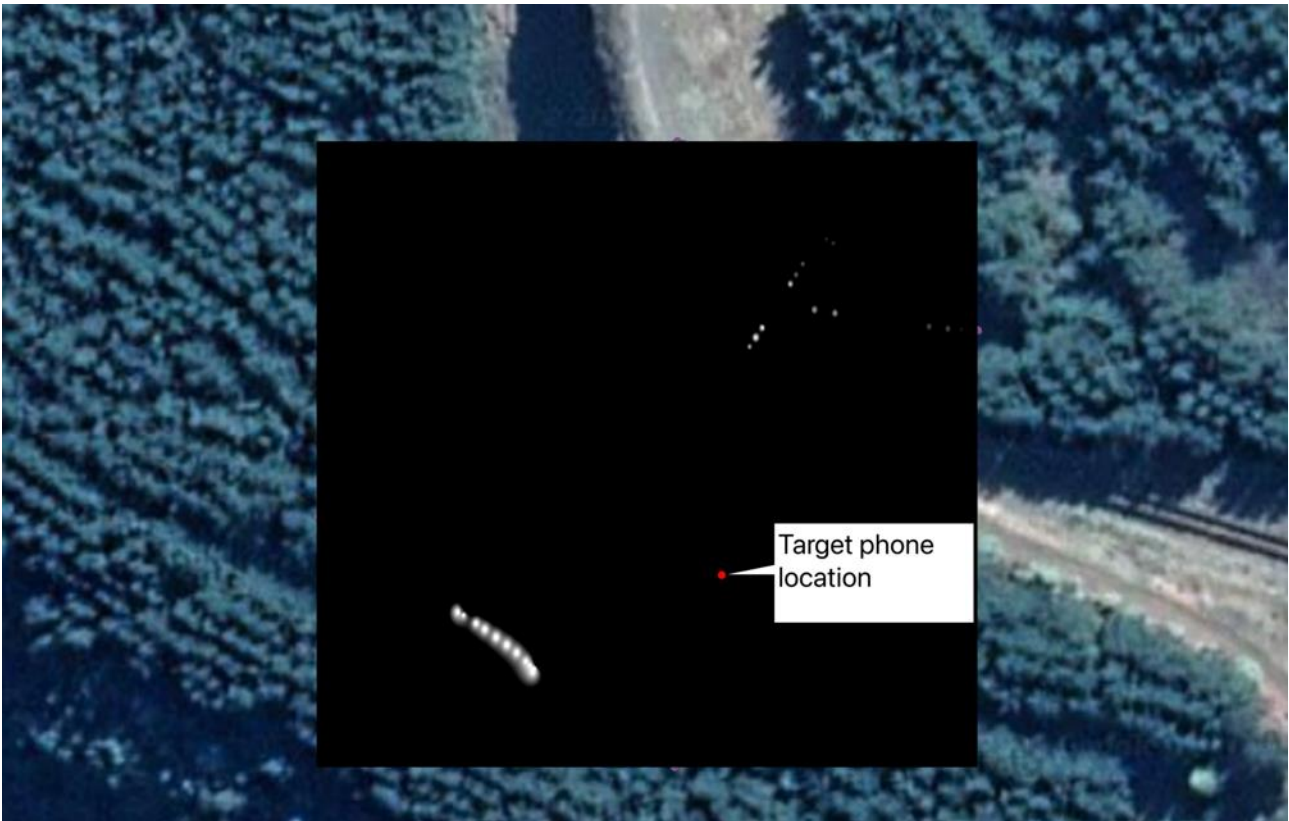


Figure 58: Fully processed heat-map from primary test 4

It can be seen from Figure 58 that there is little correlation between the hotspots in the heat-map and the location of the mobile phone. The hotspots seen in this heatmap can likely be attributed to erroneous readings. The resulting radial error (from measured UE location to the centroid of the largest hotspot) is approximately 47m. This proves that the omnidirectional antenna does not provide useful inferences for mobile phone localisation. It is curious that there is an erroneous reading in roughly the same location as observed in primary test 2 (south-west of the location of the UE). The cause of this is unknown.

8.3.8 Observations

The results obtained during primary testing reinforce the observations from preliminary testing. There are several insights gained from primary testing which gives the opportunity for further research. A nadir cellular antenna is fundamental to the accurate acquisition of cellular measurements. Additionally, the directional link between the UAV and the GCS is paramount to ensure the EPC to eNB link remains intact, and therefore ensure seamless operation of the system. Using an omnidirectional antenna on the ground system would greatly hinder the radial range of the UAV with respect to the GCS (see Appendix D). From the primary testing, it appears as though there are certain flight parameters that are conducive to higher accuracy. Namely flight height. Flight height can be tailored depending on the height of the surrounding environment. However, comparing the results from flight heights of 60m and 80m shows the enhanced accuracy yielded by flying at a lower altitude of 60m. This is due to several factors such as potential roll/tilt error having a less pronounced effect at lower altitude, as well as reduced parallel flight pass spacing at lower altitudes. Increasing the percentage of side overlap in flight planning software intuitively leads to greater resolution of results, however this must be traded against battery life.

9. Conclusions and Recommendations

9.1 Summary

This thesis explores the suitability of a cellular aerial base station for locating mobile phones in search and rescue scenarios and aims to highlight the qualitative aspects that make such a system conducive to search and rescue. Based on gaps in literature, this thesis also explores the use of a nadir directional antenna for the cellular radio, and a segregated LTE architecture, and the effect of these aspects on the performance of the system.

The baseline aircraft was modified such that these hardware components could be added to the vehicle. Additionally, a ground control station was designed and built to enable the segregated LTE architecture. Due to the inherent limitations of the vehicle (e.g., weight, battery capacity), case-by-case decisions were made to offload processing onto the more capable ground control station. This lends credence to running the resource-heavy EPC on the more capable GCS, rather than the UAV's onboard computer. Due to the design of the system, it is not possible to meet strict LTE timing requirements if the eNB *and* the EPC are run on the onboard computer. To maintain seamless operation of this link in an operationally realistic setting, a tracking directional antenna is required. Therefore, the directional link between the GCS and UAV is warranted, thus answering research subquestion 2.

A COTS mobile phone was paired to the LTE base station and used as the target UE. Preliminary testing proved the technical feasibility of the operating principle, yet also provided useful insights and changes required to the system prior to primary testing. After implementing the changes, the system was tested in a more realistic scenario. This reinforced the insights gained from preliminary testing, yet also gave further insights to the improvements that are required in future work. The primary testing answered the research subquestions. Subquestion 1 was answered during primary testing, whereby the omnidirectional receiving antenna attached to the radio frontend yields a significantly larger radial error than the nadir directional antenna.

Whilst the testing performed during this research project proves the technical feasibility and validates structural and functional design of the system, there remains a body of work that is required to advance the system to a state where it can be used in real-world search and rescue scenarios. This body of work was deemed out of scope of this thesis. These recommendations are covered in subsection 9.2. The conclusions made from this body of work are sufficient in fulfilling the purpose of this research as a proof of concept for the sponsor company, Salcom Ltd.

In conclusion, this research established that:

- an aerial base station is suitable for search and rescue purposes
- cellular signal strength metrics are suitable for location inference
- a directional transmitter antenna aboard the aerial base station improves location inference

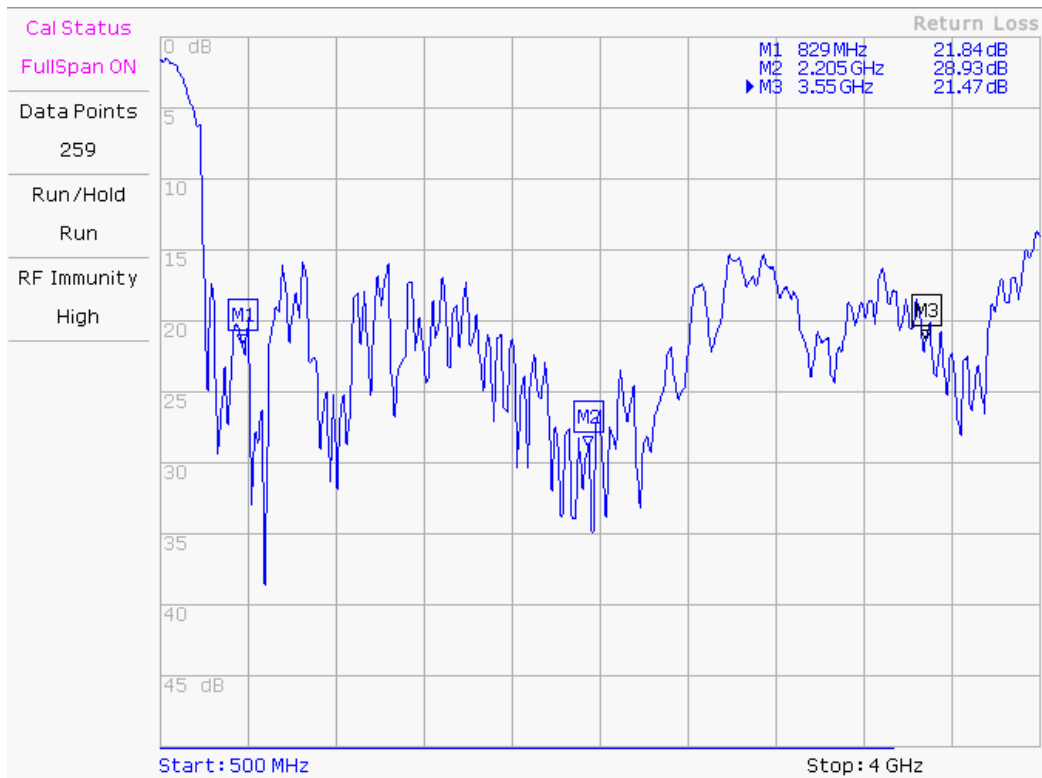
9.2 Recommendations for Future work

The following recommendations have been curated based on the results collected to date, and the subsequent analysis:

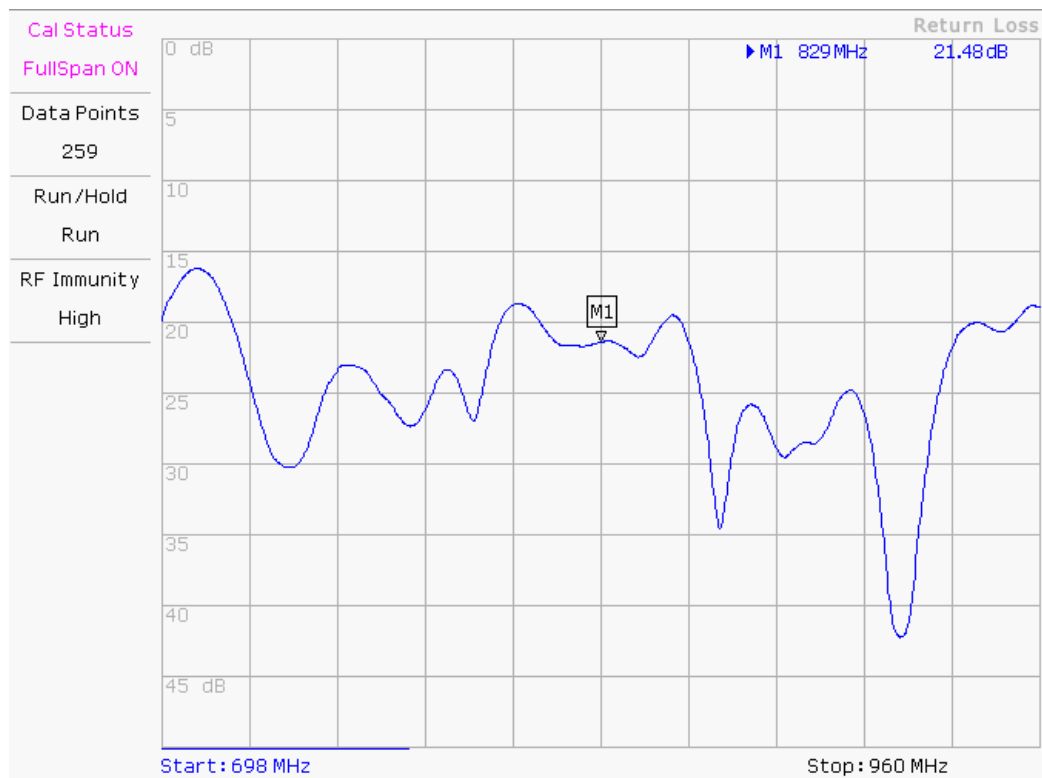
- Thoroughly characterise the RF components of the system, such as more detailed propagation simulations and radiation patterns. This would allow for more informed discernment between positive and false-positive hotspots.
- Use a less-constrained baseline vehicle. Using a baseline vehicle that had greater payload capacity and greater battery capacity would allow for greater onboard computer performance, and a multi-axis antenna compensation mechanism to be implemented. This would reinforce the qualitative characteristics of the nadir antenna implementation. Using a baseline vehicle that was RTK-enabled would also allow for reduced radial error due to significantly greater GPS accuracy.
- Record more ROS data to correct the position data in post-processing. This pertains to the roll error discussed in Figure 54. Collecting more data and using it in a post-process workflow would allow for greater correction of environmental effects, such as crosswinds and gusts.
- Use a weather station during testing and operation in order to characterise any confounding factors due to weather (e.g., wind speed and direction).
- Investigate and test different modalities of the system. For example, record and map attach/detach requests of the UE to the eNB. Mapping attach and detach requests as a function of position from the UE to the eNB would be more applicable for larger search areas where a signal-strength-based solution would fail due to minimum receiver sensitivities.
- Investigate the applicable functions and features of latter LTE releases and 5G releases for improvement opportunities. As of the time of writing, Software Radio Systems has just released a new version of srsRAN which has support for 5G non-standalone.
- Test in environments which are representative of urban search and rescue scenarios. This is important for determining whether this system is capable in a range of search and rescue scenarios.
- Investigate the effect of different terrains on the performance of the system (e.g., undulating, flat, mountainous).
- Test with more than one UE. Due to issues tracking network identifier to UE mapping, this was not implemented in this system. However, it is pertinent to analyse the performance with more than one UE.
- Investigate the advantages and disadvantages of using uplink reference signals (such as DMRS) as localisation metrics.
- Design and perform tests to prove/disprove the speculative interactions highlighted in preliminary and primary testing

Appendix A - Antenna Return Loss

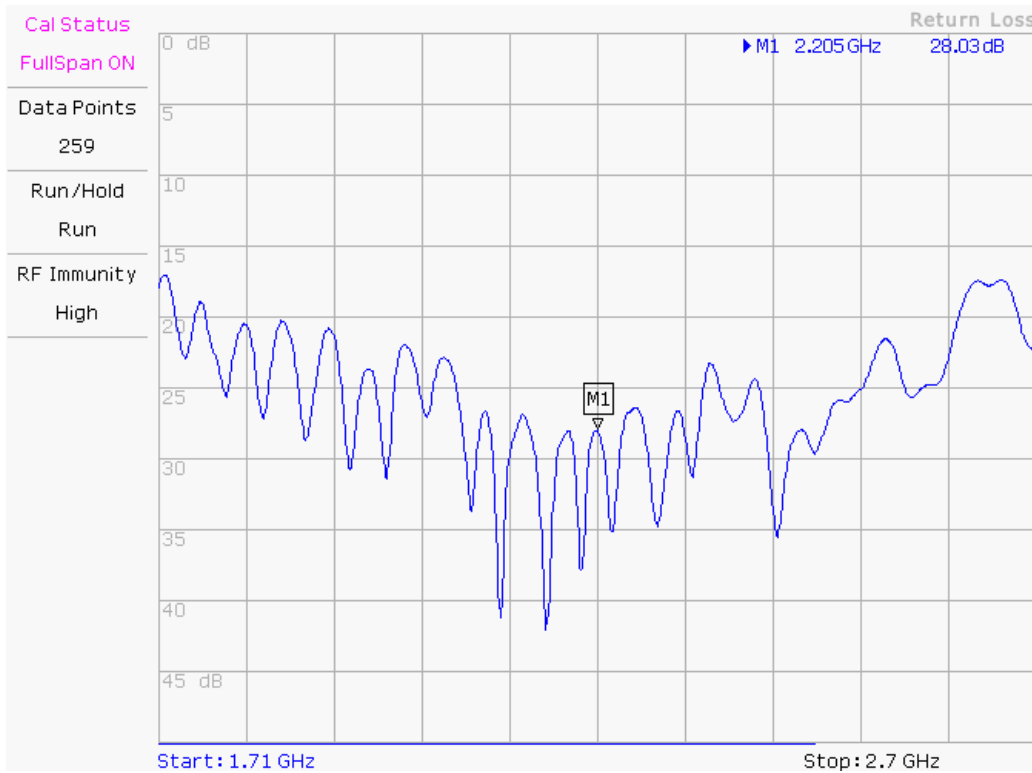
i.) Entire Band: 500MHz - 4000MHz



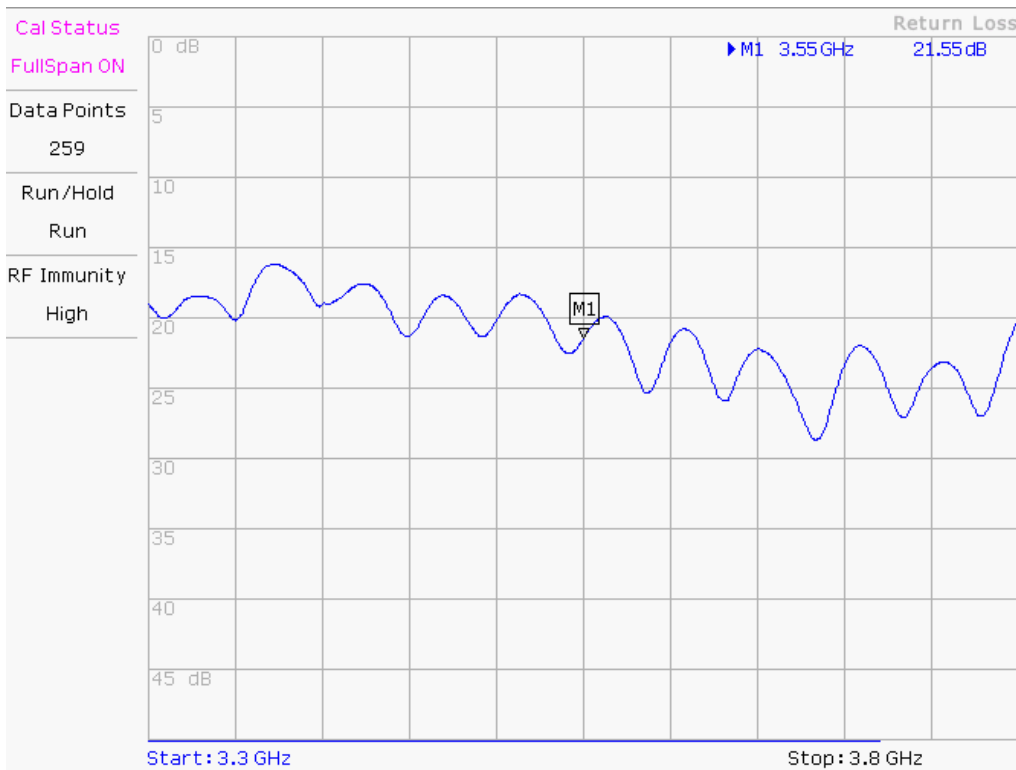
ii.) Lower Band: 696MHz - 960MHz



iii.) Middle Band: 1700MHz - 2700MHz



iv.) Upper Band: 3300MHz - 3800MHz



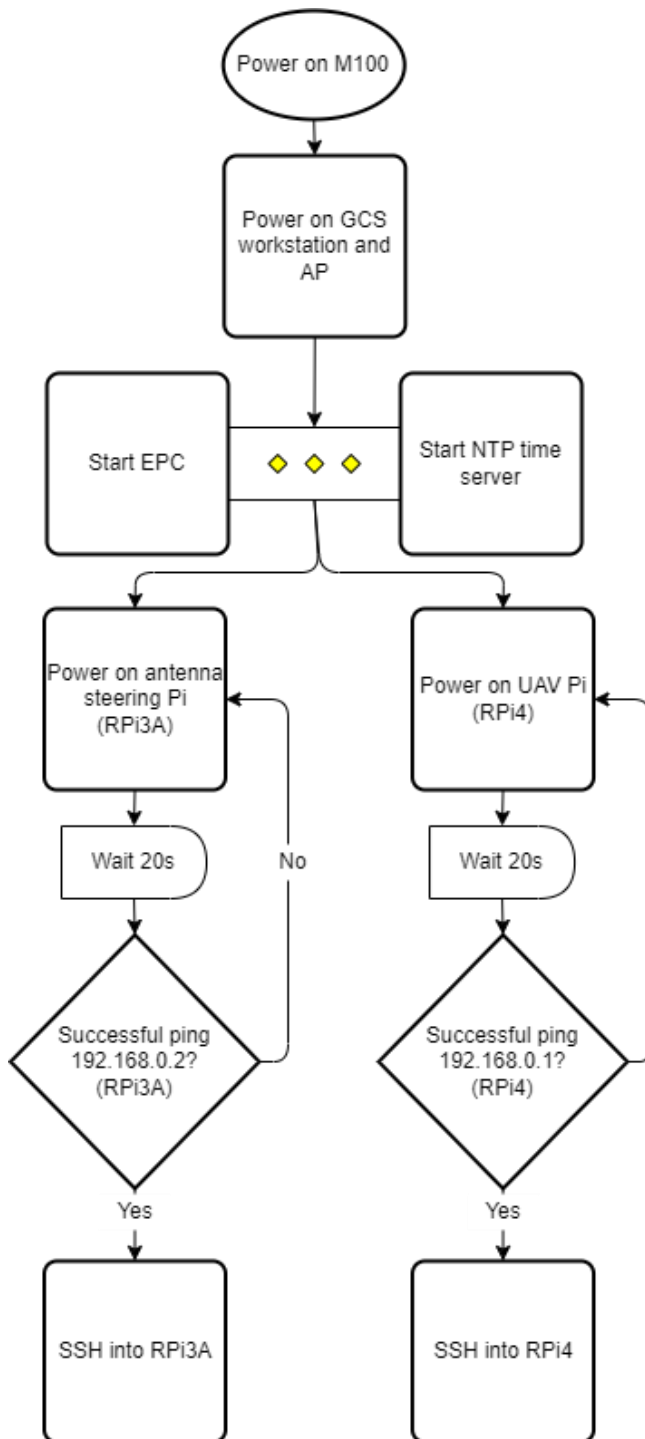
Appendix B - Configured srsRAN Parameters

Parameter	Explanation	Set as	Justification	Configured in
Mobile Country Code	Denotes which country the LTE deployment is in	901	Trans-national country code. 901 is an abandoned country code	epc.conf
Mobile Network Code	Denotes an individual LTE network provider	70	Unused MNC	epc.conf
Timing advance in samples	The propagation delay (in number of samples) that should be compensated between the RF frontend and processing of samples	27	For the BladeRF xA4 frontend, 27 sample timing advance is recommended	enb.conf
RRC inactivity timer	The time (in milliseconds) at which the UE's context is removed from RRC after no activity	5000	Increasing the inactivity timer introduces leniency for eNB 'brown-outs'.	enb.conf
Radio Link Failure release timer	The time (in milliseconds) at which the eNB releases the UE context after an RLF	5000	In a similar fashion to the inactivity timer, increasing RLF timer also introduces more leniency for eNB 'brown-outs'.	enb.conf

Appendix C - Software Script Flow Diagrams

i.) System Setup Workflow

This workflow shows the initiation of hardware components in the system, and the initial software verification that the system is working.



I) The first step is to power on the M100.

II) Next step is to power on the GCS workstation, and the Wi-Fi AP.

III) Next, the EPC is started on the GCS, and the NTP time server is initiated.

IV) Next, both Raspberry Pi's must be powered on. Both the GCS Pi (RPi3A) and UAV Pi (RPi4).

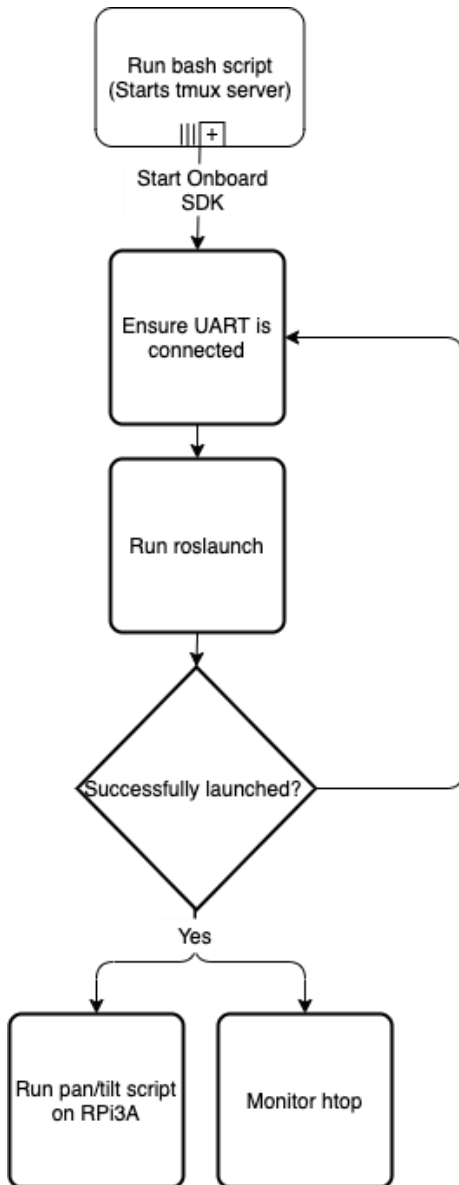
V) Neither of the Pi's can be pinged until they have properly booted and configured their network interfaces.

VI) Next, ping both Pi's to see if their network interfaces are properly configured.

VII) If network interfaces are configured properly, the GCS workstation can SSH into both Pi's separately.

ii.) Launching ROS Workflow

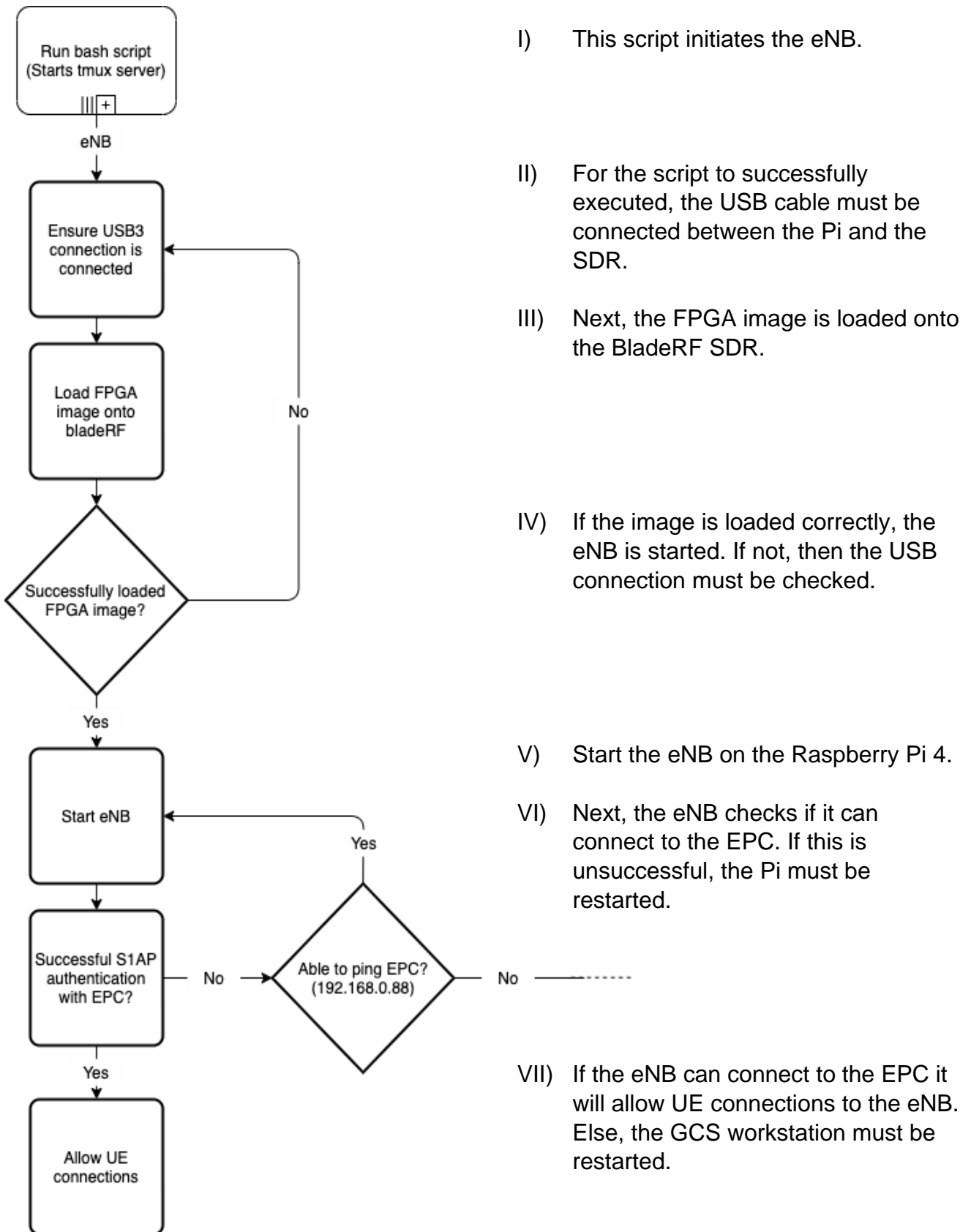
This workflow shows the initiation of ROS within the system. This is the next workflow within the system initiation process.



- I) After all systems are started and can be pinged from each node in the network, the tmux server is started. One of the sub-scripts that is executed is *start_ros.sh*.
- II) For this script to run successfully, the UART cable must be connected between the UAV and the onboard Raspberry Pi 4.
- III) The *roslaunch* command is executed and fails if the UART cable is not connected properly.
- IV) If the script fails to launch, there is usually an error in the UART connection, or the read/write permissions on the Raspberry Pi GPIO.
- V) Once the *roslaunch* command has completed, all the ROS nodes in the system can perform their tasks, this includes the steering mechanism control script run on the Raspberry Pi 3A.

iii.) Launching Cellular Workflow

This workflow shows the initiation of the various srsRAN constituent components. This is the final setup workflow within the system initiation process.



Appendix D Wi-Fi Link Range Using Omnidirectional Antenna

In subsection 5.3.4, the effective range of the wireless 2.4GHz link between the UAV and GCS using the 19dBi 2.4GHz grid-pack antenna is calculated with respect to the 4dBi omnidirectional 2.4GHz whip antenna (attached to Wi-Fi dongle) on the UAV. However, research subquestion 2 concerns the extent to which a directional GCS antenna is warranted between the GCS and UAV. Therefore, it is pertinent to calculate the link range in the case where an *omnidirectional* antenna is used instead of a directional antenna on the GCS. The omnidirectional antenna parameters used in this calculation are based on the antenna that is supplied with the MikroTik Metal. This antenna has 6Bi gain at 2.4GHz.

Therefore, the maximum useable distance of this link can be calculated if modelled as a point-to-point link in free space:

Where:

- P_T is the transmitter power of the GCS AP (dBm): $P_T = 17\text{dBm}$
- G_T is the antenna gain of the GCS AP: $G_T = 6\text{dBi}$
- G_R is the antenna gain of the UAV Wi-Fi dongle: $G_R = 4\text{dBi}$
- L_{margin} is the link margin: $L_{margin} = 15\text{dB}$
- c is the speed of light: $c \approx 3 \times 10^8 \text{ m/s}$
- d is the relative distance between GCS and UAV Wi-Fi antennae
- f is the frequency of the signal: $f = 2.4 \text{ GHz}$

The minimum receiver sensitivity of the UAV Wi-Fi dongle for different link speeds at 2.4GHz (802.11n) is:

- 54Mbps: -68dBm
- 11Mbps: -85dBm

Therefore, to sustain a minimum link speed of 50Mbps, the minimum receiver sensitivity is -68dBm. The maximum distance considering the UAV Wi-Fi dongle as the transmitter and GCS antenna as the receiver can be calculated:

$$P_T + G_T + G_R - L_{margin} - P_{loss} \geq -68$$

$$17 + 6 + 4 - 15 - P_{loss} \geq -68$$

$$\text{Therefore } P_{loss} \leq 80\text{dB}$$

$$FSPL = 20\log_{10}(d) + 20\log_{10}(f) + 20\log_{10}\left(\frac{4\pi}{c}\right)$$

$$20\log_{10}(d) + 20\log_{10}(2.4 \times 10^9) + 20\log_{10}\left(\frac{4\pi}{3 \times 10^8}\right) \leq 80$$

$$d \leq 10^{\frac{80 - 20\log(2.4 \times 10^9) - 20\log\left(\frac{4\pi}{3 \times 10^8}\right)}{20}}, \text{ therefore } d \leq 99.4\text{m}$$

Therefore, the maximum link distance between GCS and UAV, while maintaining a 15dB link margin and maintaining a >50Mbps link, using an omnidirectional antenna on the GCS is approximately 100m (assuming free space LoS conditions). This is prohibitively low compared to the (approximate) 444m range by using the directional antenna as calculated in subsection 5.3.4. It is a safe assumption that the UAV and GCS will be in line of sight of each other within a typical operating scenario.

However, in contrast to the GCS implementation with a directional antenna, the omnidirectional counterpart does not need to be placed a certain distance from the operational area of the UAV to compensate for the UAV's speed (i.e., antenna tracking of the UAV). This is because the directional implementation must steer the antenna and has certain limitations on panning and tilting speeds (see subsection 5.3.3). The omnidirectional implementation does not need the antenna to be steered due to the *more* isotropic radiation pattern of the omnidirectional antenna. However, it is worth noting that the radiation pattern of the omnidirectional antenna is *not* isotropic and has poor performance directly above the omnidirectional antenna (if the antenna is vertically polarised). In a realistic use case, it is very likely that the UAV would be directly above the GCS if the omnidirectional GCS implementation is used. This could cause the Wi-Fi link to fall under the required sensitivity, and therefore risk a link failure. In the case where an omnidirectional GCS implementation is used, it is advisable to place the GCS offset from the area of operation such that the radiation pattern of the antenna is conducive to sustaining the link. In this case, the maximum radial distance of the UAV with respect to the omnidirectional GCS would be approximately 100m to maintain a 15dB link margin and a >50Mbps link. Furthermore, as seen in Figure 31 and Figure 32, the average bitrate achieved using an omnidirectional antenna (as opposed to a directional antenna) yields significantly lower performance.

This is quite a prohibitive distance and warrants the directional GCS implementation for realistic deployments of such a system.

Bibliography

- Acuna, V., A. Kumbhar, E. Vattapparamban, F. Rajabli and I. Guvenc (2017). Localization of WiFi Devices Using Probe Requests Captured at Unmanned Aerial Vehicles. 2017 IEEE Wireless Communications and Networking Conference (WCNC).
- Aditya, S., A. F. Molisch and H. M. Behairy (2018). "A Survey on the Impact of Multipath on Wideband Time-of-Arrival Based Localization." *Proceedings of the IEEE* 106(7): 1183-1203.
- Albanese, A., V. Sciancalepore and X. Costa-Pérez (2020). "SARDO: An automated search-and-rescue drone-based solution for victims localization." *arXiv preprint arXiv:2003.05819*.
- Avanzato, R. and F. Beritelli (2019). "An Innovative Technique for Identification of Missing Persons in Natural Disaster Based on Drone-Femtocell Systems." *Sensors (Basel, Switzerland)* 19(20): 4547.
- Avanzato, R. and F. Beritelli (2020). "A Smart UAV-Femtocell Data Sensing System for Post-Earthquake Localization of People." *IEEE Access* 8: 30262-30270.
- Avanzato, R., F. Beritelli and M. Vaccaro (2019). Identification of Mobile Terminal with Femtocell on Drone for Civil Protection Applications. 2019 10th IEEE International Conference on Intelligent Data Acquisition and Advanced Computing Systems: Technology and Applications (IDAACS).
- Bäckström, C.-J. and N. Christoffersson (2006). "Urban Search and Rescue-An evaluation of technical search equipment and methods." *LUTVDG/TVBB--5197--SE*.
- Charfuelan, M. and G. Kruijff (2013). Classification of speech under stress and cognitive load in USAR operations. 2013 IEEE International Conference on Acoustics, Speech and Signal Processing.
- Chen, L., M. Loschonsky and L. M. Reindl (2012). "Autoregressive modeling of mobile radio propagation channel in building ruins." *IEEE transactions on microwave theory and techniques* 60(5): 1478-1489.
- Coldrey, M., J. Berg, L. Manholm, C. Larsson and J. Hansryd (2013). "Non-line-of-sight small cell backhauling using microwave technology." *IEEE Communications Magazine* 51(9): 78-84.
- Coldrey, M., U. Engström, K. W. Helmersson, M. Hashemi, L. Manholm and P. Wallentin (2014). "Wireless backhaul in future heterogeneous networks." *Ericsson Review* 91: 1-11.
- Dehghan, S. M. M., M. Farmani and H. Moradi (2012). Aerial localization of an RF source in NLOS condition. 2012 IEEE International Conference on Robotics and Biomimetics (ROBIO).
- Deruyck, M., J. Wyckmans, W. Joseph and L. Martens (2018). "Designing UAV-aided emergency networks for large-scale disaster scenarios." *EURASIP Journal on Wireless Communications and Networking* 2018(1): 79.

Deruyck, M., J. Wyckmans, L. Martens and W. Joseph (2016). Emergency ad-hoc networks by using drone mounted base stations for a disaster scenario. 2016 IEEE 12th International Conference on Wireless and Mobile Computing, Networking and Communications (WiMob), IEEE.

DJI. (2019). "Matrice 100 Specs." 2021, from <https://www.dji.com/nz/matrice100>.

Dressel, L. and M. J. Kochenderfer (2018). Pseudo-bearing Measurements for Improved Localization of Radio Sources with Multirotor UAVs. 2018 IEEE International Conference on Robotics and Automation (ICRA).

Dressel, L. K. and M. J. Kochenderfer (2018). Efficient and low-cost localization of radio signals with a multirotor UAV. 2018 AIAA Guidance, Navigation, and Control Conference.

Elkhrachy, I. (2021). "Accuracy Assessment of Low-Cost Unmanned Aerial Vehicle (UAV) Photogrammetry." *Alexandria Engineering Journal* 60(6): 5579-5590.

Enayati, S., H. Saeedi, H. Pishro-Nik and H. Yanikomeroğlu (2019). "Moving aerial base station networks: A stochastic geometry analysis and design perspective." *IEEE Transactions on Wireless Communications* 18(6): 2977-2988.

Erdelj, M., M. Król and E. Natalizio (2017). "Wireless sensor networks and multi-UAV systems for natural disaster management." *Computer Networks* 124: 72-86.

Galindo, G. and R. Batta (2013). "Review of recent developments in OR/MS research in disaster operations management." *European Journal of Operational Research* 230(2): 201-211.

Garavaglia, A., C. Brunner, D. Flore, Y. Ming and F. Pica (2005). Inter-system cell reselection parameter optimization in UMTS. 2005 IEEE 16th International Symposium on Personal, Indoor and Mobile Radio Communications.

Ge, B., K. Wang, J. Han and B. Zhao (2015). "Improved RSSI Positioning Algorithm for Coal Mine Underground Locomotive." *Journal of Electrical and Computer Engineering* 2015: 918962.

George, M. and K. Vadivukkarasi (2015). "Kalman filtering for RSSI based localization system in wireless sensor networks." *10*: 16429-16440.

Gomez-Migueluez, I., A. Garcia-Saavedra, P. D. Sutton, P. Serrano, C. Cano and D. J. Leith (2016). srsLTE: An open-source platform for LTE evolution and experimentation. Proceedings of the Tenth ACM International Workshop on Wireless Network Testbeds, Experimental Evaluation, and Characterization.

Gomez Chavez, K., A. Al-Hourani, L. Goratti, R. Riggio, K. Sithamparanathan and I. Bucaille (2015). Capacity Evaluation of Aerial LTE Base-Stations for Public Safety Communications.

Grogan, S., R. Pellerin and M. Gamache (2018). The use of unmanned aerial vehicles and drones in search and rescue operations – a survey.

- Guevara, K., M. Rodriguez, N. Gallo, G. Velasco, K. Vasudeva and I. Guvenc (2015). UAV-based GSM network for public safety communications. SoutheastCon 2015.
- Haider, A. and S.-H. Hwang (2019). "Maximum transmit power for UE in an LTE small cell uplink." *Electronics* 8(7): 796.
- Hamp, Q., R. Zhang, L. Chen, O. Gorgis, T. Ostertag, M. Loschonsky and L. Reindl (2014). "New technologies for the search of trapped victims." *Ad Hoc Networks* 13(Part A): 69-82.
- Han, D.-S., W. Yang, X. Liu and Y. Zhang (2013). "A weighted centroid localization algorithm based on received signal-strength indicator for underground coal mine." *Journal of China Coal Society* 38(3): 522.
- Hasan, F. (2019). *Transport Layer*, Massey University: 28.
- Hatorangan, E. and T. Juhana (2014). Mobile phone location logging into OpenBTS-based cellular network in disaster situation. 2014 8th International Conference on Telecommunication Systems Services and Applications (TSSA).
- Holloway, C. L. (2005). Propagation and detection of radio signals before, during, and after the implosion of a thirteen-story apartment building / Christopher L. Holloway.
- Holloway, C. L. (2006). Propagation and detection of radio signals before, during, and after the implosion of a large convention center / Christopher L. Holloway, et al. [Boulder, CO], National Institute of Standards and Technology.
- Holloway, C. L., G. Koepke, D. Camell, K. A. Remley and D. Williams (2005). Radio propagation measurements during a building collapse: Applications for first responders. Proc. Intl. Symp. Advanced Radio Tech., Boulder, CO.
- Holloway, C. L., G. Koepke, D. Camell, K. A. Remley, D. F. Williams, S. A. Schima, S. Canales and D. Tamura (2005). "Propagation and detection of radio signals before, during, and after the implosion of a large sports stadium (Veterans' Stadium in Philadelphia)." *Natl. Inst. Stand. Technol. Note* 1541.
- Holloway, C. L., G. Koepke, D. Camell, W. F. Young and K. A. Remley (2014). "Propagation measurements before, during, and after the collapse of three large public buildings." *IEEE Antennas and Propagation Magazine*, *Antennas and Propagation Magazine*, IEEE, IEEE Antennas Propag. Mag. 56(3): 16-36.
- Holloway, C. L., W. F. Young, G. H. Koepke, C. A. Remley, D. G. Camell and Y. Becquet (2008). Attenuation of radio wave signals coupled into twelve large building structures.
- Hood, B. N. and P. Barooah (2011). "Estimating DoA From Radio-Frequency RSSI Measurements Using an Actuated Reflector." *IEEE Sensors Journal* 11(2): 413-417.

Isaacs, J. T., F. Quitin, L. R. G. Carrillo, U. Madhow and J. P. Hespanha (2014). Quadrotor control for RF source localization and tracking. 2014 International Conference on Unmanned Aircraft Systems (ICUAS), IEEE.

Jarvis, L., J. McEachen and H. Loomis (2011). Geolocation of LTE subscriber stations based on the timing advance ranging parameter. 2011-MILCOM 2011 Military Communications Conference, IEEE.

Jianwu, Z. and Z. Lu (2009). Research on distance measurement based on RSSI of ZigBee. 2009 ISECS International Colloquium on Computing, Communication, Control, and Management.

Jiao, H., C. L. Shang, W. X. Chang and E. Li (2014). Radio frequency channel characterization of a novel localization system for rescue in disaster scenarios. 2014 XXXIth URSI General Assembly and Scientific Symposium (URSI GASS).

Kashihara, S., A. Yamamoto, K. Matsuzaki, K. Miyazaki, T. Seki, G. Urakawa, M. Fukumoto and C. Ohta (2019). Wi-SF: Aerial Wi-Fi Sensing Function for Enhancing Search and Rescue Operation. 2019 IEEE Global Humanitarian Technology Conference (GHTC).

Kawser, M. T., N. I. B. Hamid, M. N. Hasan, M. S. Alam and M. M. Rahman (2012). "Downlink snr to cqi mapping for different multipleantenna techniques in lte." International journal of information and electronics engineering 2(5): 757.

Koledoye, M. A., D. D. Martini, S. Rigoni and T. Facchinetti (2018). A Comparison of RSSI Filtering Techniques for Range-based Localization. 2018 IEEE 23rd International Conference on Emerging Technologies and Factory Automation (ETFA).

Konings, D., F. Alam, F. Noble and E. M. Lai (2019). "SpringLoc: A device-free localization technique for indoor positioning and tracking using adaptive RSSI spring relaxation." Ieee Access 7: 56960-56973.

Mehta, M., N. Akhtar and A. Karandikar (2015). Impact of HandOver parameters on mobility performance in LTE HetNets. 2015 Twenty First National Conference on Communications (NCC).

Ming, J., N. Hu, X. Niu and Y. Zhang (2017). Study on the personnel localization algorithm of the underground mine based on RSSI technology. 2017 IEEE 9th International Conference on Communication Software and Networks (ICCSN).

Moradi, M. (2018). Software-Driven and Virtualized Architectures for Scalable 5G Networks.

Moradi, M., K. Sundaresan, E. Chai, S. Rangarajan and Z. M. Mao (2018). SkyCore: Moving core to the edge for untethered and reliable UAV-based LTE networks. Proceedings of the 24th Annual International Conference on Mobile Computing and Networking.

Murphy, S. Ó., K. N. Brown and C. J. Sreenan (2017). Cellphone Localisation using an Autonomous Unmanned Aerial Vehicle and Software Defined Radio. EWSN.

- Murphy, S. O., C. Sreenan and K. N. Brown (2019). Autonomous unmanned aerial vehicle for search and rescue using software defined radio. 2019 IEEE 89th vehicular technology conference (VTC2019-Spring), IEEE.
- Murray, T. and S. F. Hasan (2020). Present State of the Art in Post Disaster Victim Localization. 2020 IEEE 5th International Symposium on Telecommunication Technologies (ISTT).
- Murray, T. and S. F. Hasan (2022). Received Signal Strength Indicator for Device Localization in Post Disaster Scenarios. 2022 International Conference on Information Networking (ICOIN).
- Nuand. (2022). "bladeRF 2.0 micro xA4." 2021, from <https://www.nuand.com/product/bladerf-xa4/>.
- NZPA. (2011). "Japanese search and rescue team races home." Retrieved 15 May, 2020, from https://www.nzherald.co.nz/nz/news/article.cfm?c_id=1&objectid=10711920.
- Okita, Y., Y. Minato and R. Shaw (2019). "Possibility of utilising international USAR teams for early recovery and non-earthquake disasters."
- Pascual Campo, P. (2018). Antenna Steering System For Directional Microwave Link With UAV Communications.
- Paúr, M., B. Stoklasa, J. Grover, A. Krzic, L. L. Sánchez-Soto, Z. Hradil and J. Řeháček (2018). "Tempering Rayleigh's curse with PSF shaping." *Optica* 5(10): 1177-1180.
- Peral-Rosado, J. A. d., R. Raulefs, J. A. López-Salcedo and G. Seco-Granados (2018). "Survey of Cellular Mobile Radio Localization Methods: From 1G to 5G." *IEEE Communications Surveys & Tutorials* 20(2): 1124-1148.
- Perez, A. (2015). "Uplink Physical Channels." *LTE and LTE Advanced: 4G Network Radio Interface*: 257-307.
- Petitjean, M., S. Mezhoud and F. Quitin (2018). Fast localization of ground-based mobile terminals with a transceiver-equipped UAV. 2018 IEEE 29th Annual International Symposium on Personal, Indoor and Mobile Radio Communications (PIMRC).
- Pokorny, J., A. Ometov, P. Pascual, C. Baquero, P. Masek, A. Pyattaev, A. Garcia, C. Castillo, S. Andreev and J. Hosek (2018). "Concept design and performance evaluation of UAV-based backhaul link with antenna steering." *Journal of Communications and Networks* 20(5): 473-483.
- Półka, M., Ł. Kuziora, S. Ptak and A. Kuczyńska (2018). "Chapter The Use of Unmanned Aerial Vehicles by Urban Search and Rescue Groups."
- Półka, M., S. Ptak and Ł. Kuziora (2017). "The Use of UAV's for Search and Rescue Operations." *Procedia Engineering* 192: 748-752.

- Qj, Y., H. Kobayashi and H. Suda (2006). "Analysis of wireless geolocation in a non-line-of-sight environment." *IEEE Transactions on wireless communications* 5(3): 672-681.
- Radišić, T., M. Muštra and P. Andraši (2019). Design of an UAV Equipped With SDR Acting as a GSM Base Station. 2019 International Conference on Systems, Signals and Image Processing (IWSSIP).
- Robusto, C. C. (1957). "The cosine-haversine formula." *The American Mathematical Monthly* 64(1): 38-40.
- Rodrigues, T. A., J. Patrikar, A. Choudhry, J. Feldgoise, V. Arcot, A. Gahlaut, S. Lau, B. Moon, B. Wagner and H. S. Matthews (2021). "In-flight positional and energy use data set of a DJI Matrice 100 quadcopter for small package delivery." *Scientific Data* 8(1): 1-8.
- Selim, M. Y. and A. E. Kamal (2018). Post-disaster 4G/5G network rehabilitation using drones: Solving battery and backhaul issues. 2018 IEEE Globecom Workshops (GC Wkshps), IEEE.
- Sevindik, V., J. Wang, O. Bayat and J. Weitzen (2012). Performance evaluation of a real long term evolution (LTE) network. 37th Annual IEEE Conference on Local Computer Networks-Workshops, Ieee.
- ShareTechnote. (2014). "4G/LTE - PHY Measurement." Retrieved 9/9/2022, 2022, from https://www.sharetechnote.com/html/Handbook_LTE_RSRP_EPPE_TotalPower.html.
- Sorbelli, F. B., S. K. Das, C. M. Pinotti and S. Silvestri (2018). Precise localization in sparse sensor networks using a drone with directional antennas. Proceedings of the 19th International Conference on Distributed Computing and Networking.
- Spence, R. J. S., E. So and C. Scawthorn (2011). Human casualties in earthquakes : progress in modelling and mitigation, Springer.
- Statheropoulos, M., A. Agapiou, G. C. Pallis, K. Mikedi, S. Karma, J. Vamvakari, M. Dandoulaki, F. Andritsos and C. L. P. Thomas (2015). "Factors that affect rescue time in urban search and rescue (USAR) operations." *Natural Hazards: Journal of the International Society for the Prevention and Mitigation of Natural Hazards* 75(1): 57.
- Strecha, C., O. Küng and P. Fua (2012). Automatic mapping from ultra-light UAV imagery.
- Sun, Y., X. Wen, Z. Lu, T. Lei and S. Jiang (2018). Localization of WiFi Devices Using Unmanned Aerial Vehicles in Search and Rescue. 2018 IEEE/CIC International Conference on Communications in China (ICCC Workshops).
- Sundaresan, K., E. Chai, A. Chakraborty and S. Rangarajan (2018). "SkyLiTE: End-to-end design of low-altitude UAV networks for providing LTE connectivity." arXiv preprint arXiv:1802.06042.

Tang, S., X. Shu, S. Shen, Z. Li and S. Cao (2017). "Study of portable infrastructure-free cell phone detector for disaster relief." *Natural Hazards* 86(1): 453-464.

Tiemann, J., O. Feldmeier and C. Wietfeld (2018). Supporting Maritime Search and Rescue Missions Through UAS-Based Wireless Localization. 2018 IEEE Globecom Workshops (GC Wkshps).

Tomic, T., K. Schmid, P. Lutz, A. Domel, M. Kassecker, E. Mair, I. L. Grixia, F. Ruess, M. Suppa and D. Burschka (2012). "Toward a fully autonomous UAV: Research platform for indoor and outdoor urban search and rescue." *IEEE robotics & automation magazine* 19(3): 46-56.

Tomiyama, M., Y. Takeda and T. Koita (2020). Location estimation algorithm using UAV for real environments. 2020 Eighth International Symposium on Computing and Networking Workshops (CANDARW).

Vijay, C., G. Sasibhushana Rao and M. V. Kumar (2019). Carrier Frequency Offset Impact on LTE-OFDM Systems. *Microelectronics, Electromagnetics and Telecommunications*, Singapore, Springer Singapore.

Wang, A., X. Ji, D. Wu, X. Bai, N. Ding, J. Pang, S. Chen, X. Chen and D. Fang (2017). "GuideLoc: UAV-Assisted Multitarget Localization System for Disaster Rescue." *Mobile Information Systems 2017*: 1267608.

Wang, W., R. Joshi, A. Kulkarni, W. K. Leong and B. Leong (2013). Feasibility study of mobile phone WiFi detection in aerial search and rescue operations. *Proceedings of the 4th Asia-Pacific workshop on systems*.

Webber, D., N. Hui, R. Kastner and C. Schurgers (2017). Radio receiver design for unmanned aerial wildlife tracking. 2017 International Conference on Computing, Networking and Communications (ICNC), IEEE.

Weldon, W. T. and J. Hupy (2020). "Investigating methods for integrating unmanned aerial systems in search and rescue operations." *Drones* 4(3): 38.

Wolfe, V., W. Frobe, V. Shrinivasan and T. Hsieh (2015). Detecting and locating cell phone signals from avalanche victims using unmanned aerial vehicles. 2015 International Conference on Unmanned Aircraft Systems (ICUAS).

Wong, J. and C. Robinson (2004). "Urban search and rescue technology needs: identification of needs." Federal Emergency Management Agency (FEMA) and the National Institute of Justice (NIJ). Document 207771.

Xu, N., S. Li, C. S. Charollais, A. Burg and A. Schumacher (2020). Machine Learning Based Outdoor Localization using the RSSI of Multibeam Antennas. 2020 IEEE Workshop on Signal Processing Systems (SiPS).

Yu, J. and F. Ye (2019). User Equipment Localization and Victim Estimation with Next-Generation PSC in Emergency Response. 2019 IEEE Global Communications Conference (GLOBECOM).

Zhu, C. (2018). Implementation and evaluation of Open Source LTE-EPC Software, Universitat Politècnica de Catalunya.

Zorn, S., M. Gardill, R. Rose, A. Goetz, R. Weigel and A. Koelpin (2012). A smart jamming system for UMTS/WCDMA cellular phone networks for search and rescue applications, IEEE: 1-3.

Zorn, S., R. Rose, A. Goetz and R. Weigel (2010). A novel technique for mobile phone localization for search and rescue applications. 2010 International Conference on Indoor Positioning and Indoor Navigation.